Effects of Connected Automated Vehicles on Traffic Flow

by

Sergei S. Avedisov

A dissertation submitted in partial fulfillment
of the requirements for the degree of
Doctor of Philosophy
(Mechanical Engineering)
in the University of Michigan
2019

Doctoral Committee:

Professor Gábor Orosz, Chair
Dr. Gaurav Bansal, A^3 by Airbus
Professor A. Harvey Bell IV
Professor Jerome P. Lynch
Professor Ramanarayan Vasudevan

Sergei S. Avedisov

avediska@umich.edu

ORCID iD: 0000-0002-1829-6677

ACKNOWLEDGEMENTS

It is imperative that I thank the co-authors of my papers Gábor Orosz, Jin I. Ge, Chaozhe R. He, Wubing B. Qin, Mehdi Sadeghpour, Adam Kiss, and Gaurav Bansal.

TABLE OF CONTENTS

LIST OF FIGURES

LIST OF TABLES

LIST OF APPENDICES

ABSTRACT

In this dissertation we provide a comprehensive framework for evaluating the merits of wireless vehicle-to-vehicle (V2V) communication on traffic. In particular we focus on mixed traffic scenarios that will dominate highways in the next several decades. Such mixed traffic primarily contains conventional human driven vehicles, however also includes connected human-driven vehicles, automated vehicles, and connected automated vehicles. Connected human-driven vehicles are human-operated vehicles that are able to send and receive messages using V2V. Automated vehicles rely on an internal computer (rather than a human) to process information from sensors such as cameras or radars to control their motion. Finally connected automated vehicles are automated vehicles that use information received from V2V communication in addition to sensory information for controlling their motion.

Our framework is based on developing a prototype connected automated vehicle and investigating its effects on traffic patterns amongst human driven vehicles. We first establish an experimental procedure and criteria for tuning the connected automated vehicle's controller to follow a connected human-driven vehicle at a desired distance. We then showcase an experimental configuration that allows us to observe traffic patterns in a three-car connected vehicle network, where our connected automated vehicle interacts with two connected human-driven vehicles. These experiments demonstrate the effectiveness of connected automated vehicles using beyond-line-of-sight information in promoting smooth traffic flow in a mixed traffic environment.

To investigate the effects of connected automated vehicles for large networks, we first focus on simple car-following models without communication, actuation or human reaction delay. For these models we are able to analytically characterize the traffic patterns occurring in human driven traffic at various densities, as well as show that connected automated vehicles can indeed mitigate congestion and promote stable uniform flow of traffic. By exploiting the cyclic symmetry of the governing equations, we rigorously show that the results hold for arbitrarily large connected vehicle networks, and also that the feedback to long-range information in connected automated vehicles should be carefully chosen to ensure the benefit to traffic flow.

Lastly we use simulations to investigate large connected vehicle networks, where delays, nonlinearities, wireless communication delay, and eclectic driving dynamics are considered. We use these simulations to demonstrate that indeed the information from beyond-line-of-sight is the key feature that allows the connected automated vehicles to bring significant benefits to traffic. Finally, we conduct penetration studies to quantify the extent to which connected automated vehicles may benefit traffic at partial penetrations, and discuss the implications of this study on the current competing wireless V2X communication technologies.

CHAPTER 1

Introduction

Ideas regarding using intelligent vehicles to improve the safety and efficiency of roadways originated in the 1930s but early efforts were not successful due to the lack of inexpensive sensors. In the last two decades we have witnessed an increase in vehicle automation and advanced driver assistance features to improve safety and driver comfort [85, 86, 81] but mobility has not seen a similar transformation. The limiting effect of vehicle automation on the mobility of roadways may be attributed to the limitations of the automated vehicles' sensory range [3]. While lidars, radars, and cameras may be sufficient to perceive the automated vehicle's immediate surroundings to ensure safety, these sensors are not able to see beyond an obstruction such as another vehicle or a blind corner.

The opportunity for automated vehicles to look beyond-line-of-sight is becoming available with vehicle-to-everything (V2X) communication technologies. These technologies allow vehicles to communicate with their environment, such as other vehicles or infrastructure, using standardized communication protocols such as dedicated short range communication (DSRC), and Cellular V2X (C-V2X) [39, 80, 21, 7, 51]. Initial developments in DSRC applications both in the United States and abroad were motivated by improving the safety of human-driven vehicles by providing the driver of an equipped vehicle with a set of warnings for safety critical applications such as forward collision warning, blind spot warning, and intersection movement assist [19]. It was later shown that the wireless information communicated through DSRC can be used in an automated vehicle to perform control and benefit safety as well as traffic flow [29, 88, 68]. At present time DSRC was successfully tested and deployed in several cities [82, 90, 98] and by several manufacturers [40]. The recent development of C-V2X as an alternative to DSRC was promoted by the 5G Automotive Association and Qualcomm [51, 2]. Initial field experiments [1] show that C-V2X provides a longer communication range than DSRC and allows for retransmission of lost packets unlike DSRC. Furthermore, because pedestrians and cyclists generally have cellular phones, C-V2X can potentially enable equipped vehicles to communicate with them in addition to

other vehicles and the infrastructure. However since C-V2X technology is more recent, it has not been tested and deployed to the extent of DSRC. The framework developed in this dissertation can be used to assess both the capabilities of C-V2X and DSRC and compare their potential in improving traffic flow.

Of particular interest are vehicle-to-vehicle (V2V) communication technology. Vehicles equipped with V2V, called connected vehicles (CVs), can communicate with each other in traffic over several hundred meters, beyond the line of sight of lidars, cameras, or radars. They can use the received V2V information to augment their perception of the environment and enhance their ability to respond. For example, a connected vehicle would be able to detect a harsh braking event several hundred meters ahead through V2V even when its lidar or camera are obstructed by surrounding vehicles [14, 34, 68]. Provided that this connected vehicle is also automated, we can then design a controller so that the vehicle responds to V2V information in a timely manner, in a way that not only ensures driver safety and comfort, but also prevents the formation of congestion [66].

To study the effects of connected vehicles and connected automated vehicles in a general traffic environment, we distinguish four types of vehicles: based on whether the vehicle is controlled by a human operator or a computer and whether it is equipped with V2X communication; see Figure 1.1. Regular vehicles are human driven (HVs) and do not have V2X capabilities. By adding V2V devices they become connected human-driven vehicles (CHVs). A vehicle whose dynamics are controlled by a computer is referred to as an automated vehicle (AV) if it only relies on sensory information or a connected automated vehicle (CAV) when it also utilises V2X connectivity. In this dissertation we focus on the impact of connectivity on traffic flow, so we assume that all automated vehicles are equipped with V2V devices, i.e., they are all connected automated. However we construct our CAVs so that they still function when no other vehicle in the neighborhood has V2V capability, in which case a CAV degrades to an AV. That is we consider a connected vehicle network, composed of connected vehicles, connected vehicles, and connected automated vehicles as shown in Figure 2.1 A,B.

The control strategy used in connected automated vehicles to achieve the desired system level behavior largely depends on the penetration of connected automated vehicles. When there are no connected vehicles present in the connected vehicle network (Figure 1.2 A), the automated vehicle can only utilize information from its immediate predecessor obtained from its seosors to control its longitudinal motion. We refer to this type of control strategy as

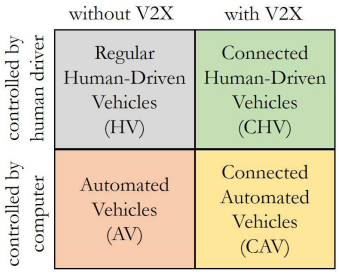

Figure 1.1: Vehicle types discussed in this dissertation.

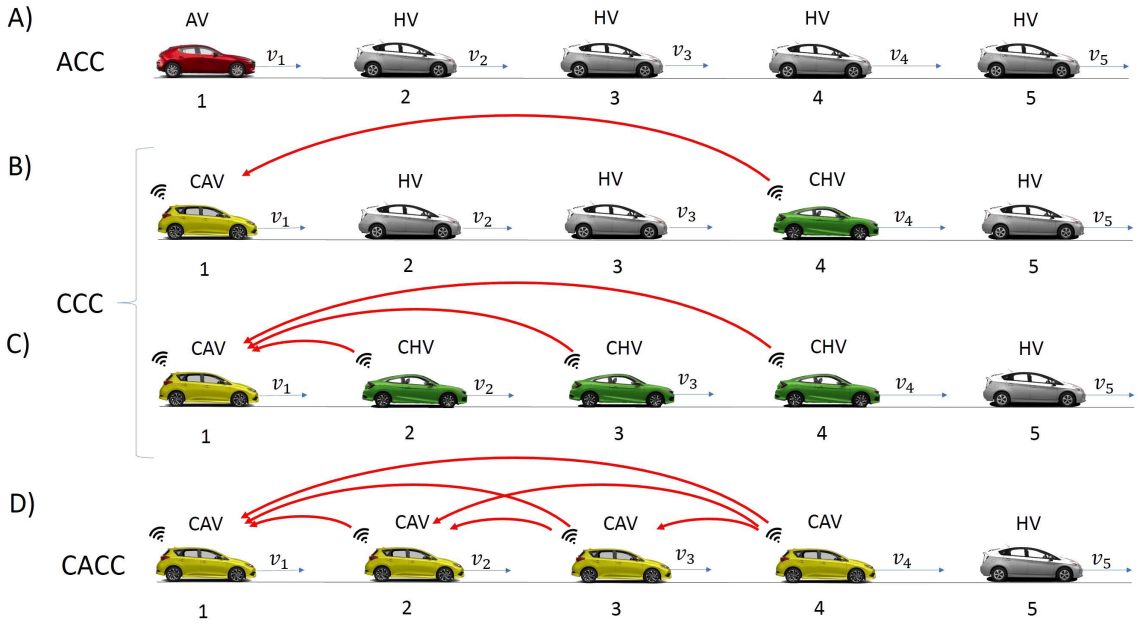

Figure 1.2: Vehicles traveling on a single lane straight road with A): a single AV in a stream of regular human-driven vehicles using ACC B): a singe CAV using information from a single CHV downstream for CCC C): a single CAV using information from multiple CHVs downstream for CCC D): a formation of CAVs traveling after each other using CACC

adaptive cruise control (ACC). The simplest realization of a connected cruise control (CCC) is shown in Figure 1.2 B, where a single CAV is able to use information from a downstream CHV beyond the CAV's line of sight to perform longitudinal control. In general, a connected automated vehicle can use CCC to utilize information from multiple connected vehicles ahead, both within and beyond line of sight [8, 25, 27, 62, 109]; see Figure 1.2 C. Also CCC does not require a pre-defined connectivity structure which makes CCC an effective control for small penetrations of CVs and CAVs.

At sufficiently high levels of CAV penetration a scenario in which several CAVs follow each other is more likely to occur, see Figure 1.2. Such scenarios allow the CAVs

to implement cooperative adaptive cruise control (CACC), where all the CAVs use V2V communication to control their motion in a coordinated fashion to achieve certain control objectives [4, 29, 54, 55, 72]. The main challenge of CACC is that multiple CAVs need to maintain a formation to reap its benefits, which would be especially challenging in a low CAV penetration environment.

For a general control strategy a specific controller for CAVs needs to be first designed and tuned, and then it's impact on traffic patterns can be evaluated. Designing and tuning of CAV controllers is usually done in an open chain configuration, where a few vehicles are traveling one after another in a single lane road, as in Figure 2.1 A. Such a connected vehicle network configuration can be studied both analytically [27, 54, 109, 72] and implemented experimentally [28, 56, 60]. Once a controller with suitable properties has been developed, a ring configuration can be used to evaluate the impact of the CAVs on traffic patterns, see Figure 2.1 B. The advantage of this configuration is that it allows one to observe traffic patterns for a relatively small number of vehicles. This configuration is mostly used in analytical and simulation studies [22, 65, 66, 8, 9], however some experiments using this configuration were also performed [93, 91, 11]. Because we focus on traffic patterns in this dissertation, we will mostly be dealing with the ring configuration. Initially we use the open chain configuration to tune the gains for the controller on our experimental CAV. Note that for large numbers of vehicles, the open chain and ring configurations become equivalent and yield the same analytical results [24].

In this dissertation we first develop an experimental connected automated vehicle that performs car following in a fashion similar to a human driver, however is also able to exploit information from beyond the line of sight by means of V2V communication. We tune the feedback gains of the controller by performing car following experiments and using experiment-based criteria in addition to theoretical criteria. We then design an experimental framework to investigate traffic patterns for a three-car connected vehicle network consisting of one connected automated vehicle and two connected human-driven vehicles. This setup features a special boundary condition enforced by the connected automated vehicle allowing us to observe traffic patterns at a wide range of traffic densities and speeds. The results of these experiment show that by utilizing beyond-line-of-sight information, connected automated vehicles allow for more traffic throughput compared to when the connected automated vehicle only uses feedback from the nearest neighbor.

Inspired by our experiments with the connected automated vehicle, we perform an

analytical investigation of traffic patterns in connected vehicle networks using rigorous network-based methods. These methods enable us to determine whether the vehicle network would tend to uniform flow or whether congestion waves would develop. Furthermore, we can account for the nonlinear behavior of traffic such as bistablity, where either uniform flow or congestion may develop depending on the disturbance. These network-based methods also allow us to evaluate the effects of introducing connected automated vehicles which use beyond the line of sight information into the traffic flow. Based on the insights gained from analytically investigating traffic patterns and matching car-following models to experimental data we perform a large-scale simulation study of connected vehicle networks at partial penetrations of connected and connected automated vehicles. These simulations enable us to include complex phenomena such as driver variability, delays due to actuation, reaction, and communication, and demonstrate the scalability of connected cruise control.

Using the above simulations we are able to quantify the benefits of connected automated vehicles on traffic flow at partial penetrations. In particular, we can highlight the day one benefits, when the penetrations of connected automated vehicles on the road are small. Furthermore, we discuss the merits of our framework in comparing different types of wireless communication technologies, in particular whether using C-V2X would yield significant benefits in improving flux compared to DSRC. We also note that the framework carried out in this dissertation can be used to examine the merits of connected automated vehicles in other key metrics, such as fuel economy and driver comfort.

This dissertation is organized as follows. In the remainder of Chapter 2 we present the dynamical model for the vehicles in the connected vehicle network, as well as discuss the open chain and ring configurations in detail. We then tune the longitudinal controller for the connected automated vehicle, and investigate how it influences traffic patterns in Chapter 3. In Chapter 4 we look at the nonlinear dynamics of a conventional vehicle network where all vehicles rely on information coming from the vehicle immediately ahead. In Chapter 5 we investigate the effects of connected automated vehicles, that can utilize beyond the line of sight information, on traffic dynamics using-network based perturbation methods. In Chapter 6 we perform simulations of CVNs with at various penetration rates of connected and connected and automated vehicles and discuss the implication of these simulations on the current standing of V2X technologies. Finally we conclude this dissertation in Chapter 7.

CHAPTER 2

Modeling a connected vehicle network

In this section we discuss the dynamics of the different vehicles in the connected vehicle network as well as the configurations of the connected vehicle network.

2.1 Vehicles in a connected vehicle network

We consider a connected vehicle network composed of conventional vehicles, connected vehicles, and connected automated vehicles as shown in Figure 2.1 A,B. As in this dissertation we are interested in car-following along a single lane, so we only consider longitudinal dynamics of the vehicles in the connected vehicle network to be significant. We first introduce the general longitudinal dynamics of a vehicle in the network, and then discuss the differences in dynamics between human-driven and connected automated vehicles.

2.1.1 Longitudinal vehicle dynamics

We consider a connected vehicle network with N vehicles. Let us denote the position of the rear bumper of vehicle i by s_i and its velocity by v_i; see Figure 2.1 A. We neglect tire slip, suspension dynamics, aerodynamic drag, rolling resistance, grade, and engine dynamics. Then the longitudinal motion is described by

$$\begin{aligned} \dot{s}_i(t) &= v_i(t), \\ \dot{v}_i(t) &= f_{\text{sat}}(u_i(t)), \end{aligned} \tag{2.1}$$

where the dot represents differentiation with respect to time t, u_i gives the scaled driving force commanded by the vehicle operator, and the saturation function f_{sat} represents the

limits of the engine and brakes of the vehicle. In particular, we use

$$f_{\text{sat}} = \begin{cases} u_{\min}, & \text{if} \quad u \leq u_{\min}, \\ u, & \text{if} \quad u_{\min} < u < u_{\max}, \\ u_{\max}, & \text{if} \quad u \geq u_{\max}, \end{cases} \tag{2.2}$$

shown in Figure 2.2A with limits $u_{\max} = 3\,[\text{m/s}^2]$ and $u_{\min} = -10\,[\text{m/s}^2]$, as these correspond to the acceleration limits observed in experiments.

2.1.2 Modeling regular human drivers

For regular human-driven vehicles (HVs) the human driver exhibits two kinds of longitudinal vehicle control: car following and conflict prevention. During car following the vehicle is tracking the motion of the vehicle directly ahead and chooses the acceleration based on the headway (distance to the rear bumper of the preceding vehicle) and the relative velocity to the vehicle ahead. We adopt a model from [12, 8] and assume that the driver of vehicle i responds to the motion of the preceding vehicle using the nonlinear controller

$$u_i^{\text{hf}}(t) = \alpha_i\big(V_i(h_i(t-\tau_i)) - v_i(t-\tau_i)\big) + \beta_i\big(W_i(v_{i+1}(t-\tau_i)) - v_i(t-\tau_i)\big) \tag{2.3}$$

where τ_i represents the sum of the driver reaction time and the actuation delay while α_i and β_i are control gains for the headway and relative velocity feedback, respectively. The superscript hf denotes human car following. In the relative velocity feedback W_i is a saturation function for the velocity feedback, that prevents car i from following the predecessor if $v_{i+1} > v_{\max,i}$.

$$W_i(v) = \begin{cases} v, & \text{if} \quad v < v_{\max,i}, \\ v_{\max,i}, & \text{if} \quad v \geq v_{\max,i}, \end{cases} \tag{2.4}$$

see Figure 2.2 B where $v_{\max} = 24$ [m/s].

The headway feedback term in (2.3) involves the nonlinear function $V_i(h)$ called the range policy or optimal velocity function [66, 8] which satisfies the following properties:

1. $V_i(h)$ is continuous and monotonically increasing (the more sparse the traffic is, the faster the vehicles want to travel).

2. $V_i(h) \equiv 0$ for $h \leq h_{\text{st},i}$ (in dense traffic vehicles intend to stop).

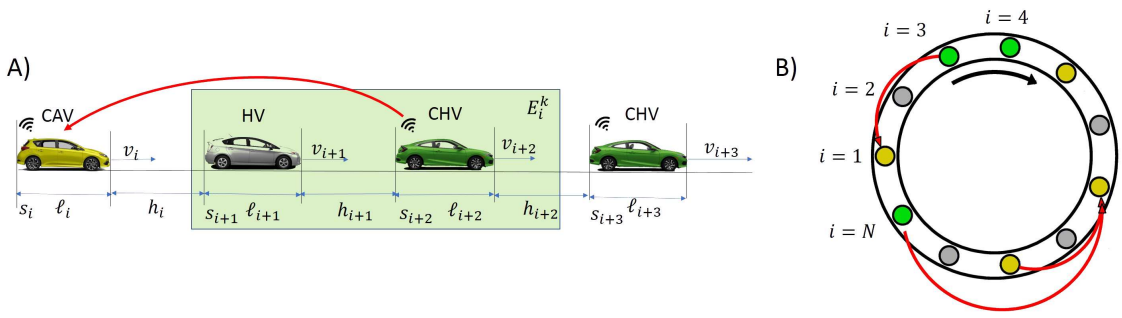

Figure 2.1: A): Connected vehicle network arranged in open chain configuration, featuring regular human driven vehicles (HVs, grey), connected human-driven vehicles (CHVs, green), and connected automated vehicles (CAVs, yellow) B): A connected vehicle network with $N = 11$ vehicles arranged in ring configuration, viewed from the top. Grey dots represent regular human-driven vehicles (HVs), green dots represent connected human-driven vehicles (CHVs), and yellow dots represent connected automated vehicles (CAVs). The vehicles move around the ring in the clockwise direction. Note that cars 1 to 4 are replicated from the open chain configuration.

3. $V_i(h) \equiv v_{\max,i}$ for $h \geq h_{\text{go},i}$ (in sparse traffic vehicles intend to travel with the maximum speed).

These properties can be summarized as

$$V_i(h) = \begin{cases} 0, & \text{if} \quad h \leq h_{\text{st},i}\,, \\ F(h), & \text{if} \quad h_{\text{st,i}} < h < h_{\text{go,i}}\,, \\ v_{\max,i}, & \text{if} \quad h \geq h_{\text{go},i}\,, \end{cases} \tag{2.5}$$

A simple choice of $F(h)$ is a piecewise-linear function

$$F(h) = \kappa(h - h_{\text{st},i}) \tag{2.6}$$

where $\kappa = v_{\max,i}/(h_{\text{go},i} - h_{\text{st},i})$. We use this range policy later on in the design of the connected automated vehicle as the slope κ can be tuned to change the aggressiveness of the CAV. Figure 2.2 C shows this function for $\kappa = 0.6$ and $\kappa = 1.0$ [s].

For human driven vehicles we use the function

$$F(h) = v_{\max,i}\left(1 - \left(\frac{h_{\text{go},i} - h}{h_{\text{go},i} - h_{\text{st},i}}\right)^2\right) \tag{2.7}$$

as we see from Figure 2.2 D that this function fits experimental data collected from human drivers well. Model matched parameters of these range policies to two different human

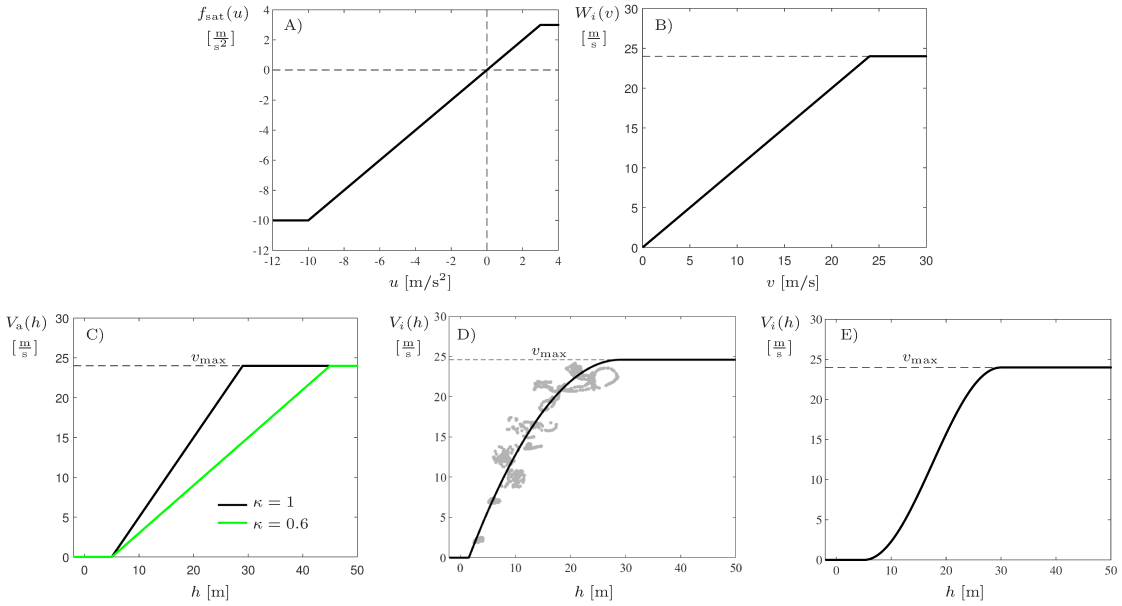

Figure 2.2: A): Saturation function for the acceleration of vehicles. B): Speed saturation function for vehicle i C): Piecewise linear range policy designed for automated vehicle with different aggressiveness D): Quadratic range policy for human driven vehicles fitted to data E): Trigonometric range policy used for nonlinear analysis.

drivers are given in the first two rows of Table 2.1, and these were determined from experiments by model matching as detailed in Section 3.2.2 and Appendix B. In order to analytically examine traffic patterns in large connected vehicles in Chapters 4, 5 we use a smooth range policy

$$F(h) = \frac{v_{\max}}{2}\left(1 - \cos\left(\pi \frac{h - h_{\mathrm{st},i}}{h_{\mathrm{go},i} - h_{\mathrm{st},i}}\right)\right) \tag{2.8}$$

which is plotted in Figure 2.2 E. Qualitatively these range policies are similar.

Table 2.1: Range policy parameters for vehicles in connected vehicle network

Vehicle	**Parameters**		
1	$h_{\mathrm{st},1} = 1.56 \pm 0.12$ [m]	$h_{\mathrm{go},1} = 29.1 \pm 0.92$ [m]	$v_{\max,1} = 24.6 \pm 1.2$ [m/s]
2	$h_{\mathrm{st},2} = -0.20 \pm 0.11$ [m]	$h_{\mathrm{go},2} = 33.9 \pm 0.64$ [m]	$v_{\max,2} = 24.0 \pm 0.6$ [m/s]
3[a]	$h_{\mathrm{st,a}} = 5$ [m]	$h_{\mathrm{go,a}} = 45$ [m] for $\kappa = 0.6$ [1/s], $h_{\mathrm{go,a}} = 29$ [m] for $\kappa = 1$ [1/s]	$v_{\max,\mathrm{a}} = 24$ [m/s]

[a] Since CAV parameters are designed, no error is given.

In order to define the conflict prevention dynamics of human-driven vehicles we define

the time to conflict of car i as

$$T_i(t) = \frac{h(t) - h_{\text{st},i}}{v_i(t) - v_{i+1}(t)}. \tag{2.9}$$

We consider that vehicle is i at risk of conflict when $T_i(t) < T_\text{c}$, i.e.,

$$v_i(t) > v_{i+1}(t) + \frac{1}{T_\text{c}}(h(t) - h_{\text{st},i}), \tag{2.10}$$

where T_c is the critical time-to-conflict. When this happens, we assume that the driver of the vehicle i tries to maintain the critical time-to-conflict using the controller

$$u_i^{\text{hc}}(t) = \dot{v}_{i+1}(t - \tau_\text{c}) + \frac{1}{T_\text{c}}\Big(v_{i+1}(t - \tau_\text{c}) - v_i(t - \tau_\text{c})\Big), \tag{2.11}$$

where τ_c is the delay associated with the human reaction time in safety-critical situations and the superscript hc refers to this being the human-driven vehicles motion under conflict prevention. The commanded longitudinal acceleration of human-driven vehicle i is then

$$u_i(t) = \begin{cases} u_i^{\text{hf}}(t), & \text{if} \quad T(t - \tau_\text{c}) \geq T_\text{c}, \\ u_i^{\text{hc}}(t), & \text{otherwise.} \end{cases} \tag{2.12}$$

2.1.3 Connected vehicles

Recall from Figure 1.1 that connected human-driven vehicles (CHVs) are human-driven vehicles equipped with V2X communication devices, enabling them to transmit and receive wireless messages. We also note that connected automated vehicles also have the same capability in terms of communication. We refer to any vehicle that uses V2X communication as a connected vehicle (CV). Messages are broadcasted intermittently with a sampling time of Δt. Here we use $\Delta t = 0.1$ [s] corresponding to the dedicated short range communication (DSRC) standard [80]. We assume that each connected vehicle samples its motion data at time instances $t_k = k\,\Delta t$, $k = 0, 1, 2, \ldots$ that can be achieved at a few millisecond accuracy in V2X devices available in the market. When a connected vehicle transmits a packet, another connected vehicle may receive the packet. According to our experiments with the vehicles and devices shown in Figure 3.5 E-F, there is no significant packet loss if the vehicles are within 300 [m] of each other in a highway environment. Thus we consider that vehicles can communicate up to 300 [m] distance.

2.1.4 Connected automated vehicles

In addition to sending and receiving V2X messages, a connected automated vehicle (CAV) utilizes the obtained information to control its motion. We assume that the CAV uses a combination of sensory information about the vehicle immediately ahead and data received from multiple vehicles ahead via V2V communication to command its longitudinal acceleration. Similar to human-driven vehicles, CAVs may also run in car following or conflict prevention modes.

In car-following mode given a processing and actuation delay τ_{a}, the acceleration of the CAV i in car-following mode is commanded by

$$u_i^{\mathrm{af}}(t) = a\Big(V_{\mathrm{a}}\big(h_i(t_k-\tau_{\mathrm{a}})\big) - v_i(t_k-\tau_{\mathrm{a}})\Big) + b\Big(W_{\mathrm{a}}(\bar{v}_i^{(\mathrm{d})}(t_k-\tau_{\mathrm{a}})) - v_i(t_k-\tau_{\mathrm{a}})\Big), \quad (2.13)$$

which is held constant during the time interval $t \in [t_k, t_{k+1})$ using a zero order hold. The superscript af denotes automated car following, while a and b are control gains for the headway feedback term and relative velocity feedback terms according to configuration in Figure 3.5 D. Also, we design the piecewise linear range policy

$$V_{\mathrm{a}}(h) = \begin{cases} 0, & \text{if} \quad h \le h_{\mathrm{st,a}}, \\ \kappa(h - h_{\mathrm{st,a}}), & \text{if} \quad h_{\mathrm{st,a}} < h < h_{\mathrm{go,a}}, \\ v_{\mathrm{max,a}}, & \text{if} \quad h \ge h_{\mathrm{go,a}}, \end{cases} \quad (2.14)$$

with the parameters provided in the third row of Table 2.1. The corresponding function is plotted in Figure 2.2 E for different values of κ. Such a design gives an intuitive interpretation to the middle section of the range policy where the slope is given by $\kappa = \frac{v_{\mathrm{max,a}}}{h_{\mathrm{go,a}} - h_{\mathrm{st,a}}}$, has a unit of $[1/\mathrm{s}]$, and can be adjusted to tune the "aggressiveness" of the CAV's controller. In our case, the slope is set to $\kappa = 1\ [1/\mathrm{s}]$ and $\kappa = 0.6\ [1/\mathrm{s}]$ depending on the scenario. The velocity feedback features the weighted average velocity $\bar{v}_i^{(\mathrm{d})}$ of the vehicles located downstream of CAV i. That is,

$$\bar{v}_i^{(\mathrm{d})}(t_k) = \sum_{j \in E_i^k} w_{i,j}(t_k) v_j(t_k), \quad \text{s.t.} \quad \sum_{j \in E_i^k} w_{i,j}(t_k) = 1, \quad (2.15)$$

where the set E_i^k denotes the downstream vehicles including

- the immediate predecessor of vehicle i ($j = i+1$). The information can either be obtained via V2V (if $i+1$ is connected) or range sensors (if $i+1$ is a regular human-

driven vehicle).

- connected vehicles within look-ahead distance D that are traveling slower than vehicle $i+1$.

as applied in [10]. In the specific case shown in Figure 2.1 A we have $E_i^k = \{i+1, i+2\}$. The CHV $i+3$ is traveling faster than the vehicle $i+1$. The headway feedback gain and relative velocity gain are tuned to $a = 0.4\ [1/\mathrm{s}]$ and $b = 0.5\ [1/\mathrm{s}]$ based on safety considerations, and $\tau_\mathrm{a} = 0.5\ [\mathrm{s}]$ was established in prior experiments with this CAV. Finally, W_a is given by (2.4), as in human-driver car following using $v_{\max,\mathrm{a}}$.

In conflict prevention mode we command the acceleration of the automated vehicle as

$$u_i^{\mathrm{ac}}(t) = \dot{v}_{i+1}(t_k - \tau_\mathrm{a}) + \frac{1}{T_\mathrm{c}}\left(v_{i+1}(t_k - \tau_\mathrm{a}) - v_i(t_k - \tau_\mathrm{c})\right), \tag{2.16}$$

which is held constant during the time interval $t \in [t_k, t_{k+1})$ using a zero order hold. That is, the overall longitudinal acceleration is given by

$$u_i(t) = \begin{cases} u_i^{\mathrm{af}}(t), & \text{if} \quad T(t - \tau_\mathrm{a}) \geq T_\mathrm{c}, \\ u_i^{\mathrm{ac}}(t), & \text{otherwise}, \end{cases} \tag{2.17}$$

in the time interval $t \in [t_k, t_{k+1})$.

2.2 Connected vehicle network configuration

In this dissertation we use two configurations of connected vehicle networks: the open chain and the ring configuration. Here we describe both of these configurations and their applications. We also discuss the **uniform flow** state as the state which we examine in each configuration.

2.2.1 Open chain configuration

An example of the open chain configuration is shown in Figure 2.1 A. In this configuration N vehicle are aligned such that the i-th vehicle follows the $i+1$-st vehicle in a single lane, with the N-th vehicle being the first vehicle in the open chain. We will investigate the open chain configuration around a pseudo-equilibrium state called **uniform flow**, where all the

vehicles travel at a constant speed v^* pre-defined by the first vehicle, and their positions along the road are given by

$$s_i^* = v^* t + s_i^0, \qquad i = 1, ..., N, \tag{2.18}$$

such that

$$\begin{aligned} s_{i+1}^0 - s_i^0 - \ell_i = h_i^*, \qquad & i = 1, ..., N-1, \\ v^* = V_i(h_i^*), \qquad & i = 1, ..., N-1\,. \end{aligned} \tag{2.19}$$

In this dissertation we primarily look at a two-vehicle open chain where a connected automated vehicle follows a connected human-driven vehicle. In Chapter 3 we investigate whether the connected automated vehicle is able to go to uniform flow while following a connected human-driven vehicle, as well as whether it will be able to sustain uniform flow upon perturbations.

2.2.2 Ring configuration

The ring configuration can be visualized by placing the open chain of N vehicles on a ring road, such that first vehicle follows the N-th vehicle, i.e., we have the periodic boundary conditions $s_{N+1} = s_1$, $v_{N+1} = v_1$, see Figure 2.1 B [22, 66, 8, 9]. The total length of the road is $L + \sum_{i=1}^{N} \ell_i$, where L is called the effective road length and ℓ_i is the length of vehicle i. In fact, vehicles 1 through 4 in Figure 2.1 B replicate the open chain configuration in 2.1 A. One can show that the ring admits a uniform flow where (2.18,2.19) are satisfied in addition to

$$\begin{aligned} s_1^0 - s_N^0 - \ell_N = h_N^*, \\ v^* = V_N(h_N^*), \qquad & i = 1, ..., N\,. \end{aligned} \tag{2.20}$$

due to the boundary condition. For a general connected vehicle network on the ring, the uniform flow velocity can be calculated by solving

$$L - \sum_{i=1}^{N} \ell_i + V_i^{-1}(v^*) = 0 \tag{2.21}$$

numerically. Note, that in order to get a unique uniform flow for a given ring length L this ring length must satisfy

$$\sum_{i=1}^{N} h_{\mathrm{st},i} \leq L \leq \sum_{i=1}^{N} h_{\mathrm{go},i}. \tag{2.22}$$

due to the V_i being invertible in that region. In subsequent chapters we analyze the connected vehicle networks in ring configuration about uniform flow to determine whether vehicles in the network would approach this state or congestion would develop.

2.3 Summary

In this section we described the dynamics of the vehicles in the connected vehicle network, namely the human-driven vehicles and the connected automated vehicles. For all vehicles, the car-following dynamics were governed by two delay-differential equations. While the delay in the human-driven vehicle case stemmed from human reaction and actuation, the delay in the connected automated vehicle is primarily due to actuation. The dynamics of the connected automated vehicles were also discretized in time to represent digital communication and control.

After introducing the dynamics of the vehicles, we considered two ways in which these vehicles can be placed on the road to form a connected vehicle network, namely the open chain configuration and ring road configuration. In the subsequent sections we first use the open-chain configuration to tune the connected automated vehicles's controller. After that we study traffic patterns using the ring road configuration.

CHAPTER 3

Experimental implementation of connected automated vehicles

In this chapter we implement a car following controller for the connected automated vehicle. First, in section 3.1 we tune the gains on the car following controller when the connected automated vehicle follows a single vehicle immediately ahead. Then in section 3.2 we examine the effects of the connected automated vehicle on the traffic patterns in a network of 3 vehicles - two connected human-driven vehicles in addition to the connected automated vehicle. We then demonstrate that when the connected automated vehicles use long-range feedback for control can significantly benefit traffic flow. In our experiments wireless vehicle-to-vehicle (V2V) communication is realized using the devices shown in Figure 3.1. They consist of an electronic control unit and an antennae which transmits basic safety messages (BSM) using standardized Dedicated Short Range Communication (DSRC) protocol [68, 80]. The information broadcasted includes position and velocity. The devices are powered through a 12 Volt power outlet and can be retrofitted to any regular vehicle. The vehicles shown in Figure 3.1 are equipped with such V2V devices. Moreover, the vehicle on the right is also capable of automated driving. In particular, the throttle and the brakes can be commanded based on the data received from the other vehicles via V2V communication.

3.1 Car following with one predecessor

In this section we design experiments to tune the car following controller of the connected automated vehicle derived in the previous section. We focus on the scenario where the connected automated vehicle follows a single connected human driven vehicle, as seen in Figure 3.1 A. In this scenario, the equations of motion of the connected automated vehicle

(2.1,2.13) can be reduced to

$$\begin{aligned} \dot{h}(t) &= v_{\mathrm{L}}(t) - v(t), \\ \dot{v}(t) &= f_{\mathrm{sat}}(u(t)), \end{aligned} \tag{3.1}$$

where

$$u(t) = a\Big(V_{\mathrm{a}}\big(h(t_k - \tau_{\mathrm{a}})\big) - v(t_k - \tau_{\mathrm{a}})\Big) + b\Big(W_{\mathrm{a}}(v_{\mathrm{L}}(t_k - \tau_{\mathrm{a}})) - v(t_k - \tau_{\mathrm{a}})\Big), \tag{3.2}$$

Note that in this case we define the dynamics using the headway h rather than the CAV's position s. This variable definition is more suited when analyzing the open-chain configuration. We use analytical criteria of plant and string stability [94] [26] as derived in Appendix A in combination with data-based criteria to select gains a and b for the above car following controller.

3.1.1 Experiments for gain tuning

In order to tune the feedback gains of the car following controller for the scenario shown in Figure 3.1 A, we perform a set of car following experiments. In these car following experiments we have a human-driven leading vehicle CHV shown in Figure 3.1 B driving on the route shown in Figure 3.1 D according to a specific speed profile. The connected automated vehicle then uses 2.13 to govern its longitudinal motion whilst being steered by a human operator. An example of the headway time profile and the velocity profile during such a test is shown in Figure 3.2 A,B.

For a given set of gains a, b the human driver of the leading vehicle performs a driving cycle where he is asked to maintain a steady state speed over four time intervals, which are marked by the grey shading. First the leading vehicle accelerates from a stop to 15 $[\mathrm{mi/hr}]$ in the first steady speed section. In the second steady state section the driver accelerates to 30 $\mathrm{mi/hr}$. In the third steady state section the driver of the leading vehicle slows down to 10 $\mathrm{mi/hr}$. Finally in the last steady state section the leading vehicle accelerates to 20 $\mathrm{mi/hr}$. Finally the leading vehicle stops, completing one lap of the course, see Figure 3.1 C. For each run we vary gains a and b, and obtain the GPS positions and velocities of the two vehicles throughout the test, see Figure 3.2A,B.

To select the proper gains we use several criteria. The first criterion is called the **time-to-conflict criterion**. We define the instantaneous time-to-conflict as

$$T(t) = \frac{h - h_{\mathrm{st}}}{v(t) - v_{\mathrm{l}}(t)}. \tag{3.3}$$

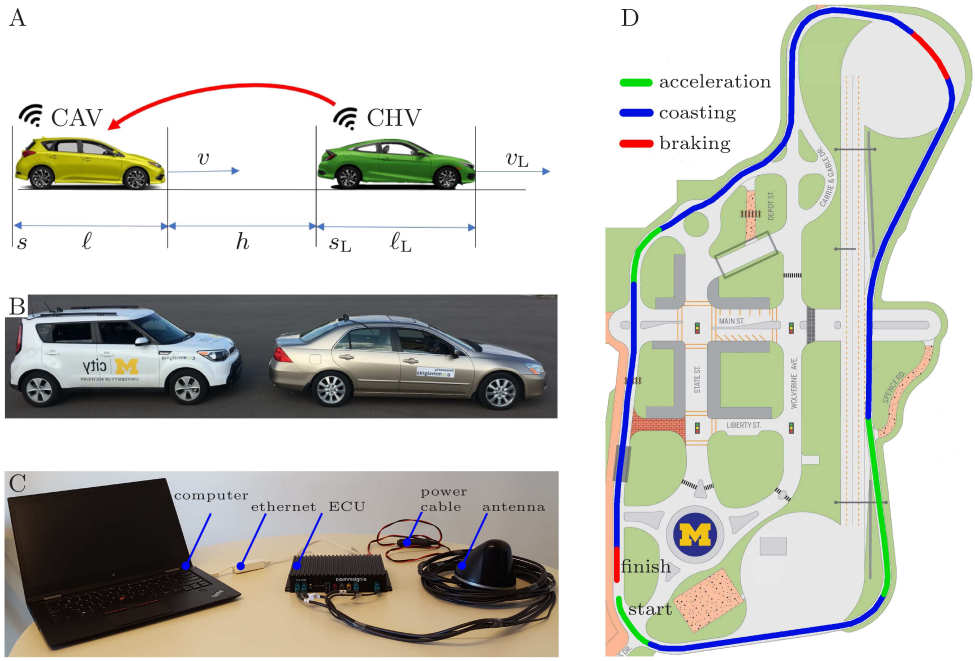

Figure 3.1: A: Connected vehicle network used in gain tuning experiment consisting of a connected human-driven vehicle (CHV) and a connected automated vehicle (CAV) in an open chain configuration. Note that the CHV has the index "L" associated with it, and the CAV has no index. B: Actual vehicles used in experiments with a human-driven connected vehicle on the left and a connected automated vehicle on the right [28, 68] C: V2V devices for connected vehicles [28, 68] D: Route for longitudinal experiment on MCity test track, with start, finish, and direction labeled. The blue line segments of the trajectory denote where leading vehicle maintains a steady state velocity, the green and red segments denote where the leading vehicle accelerates and decelerates respectively.

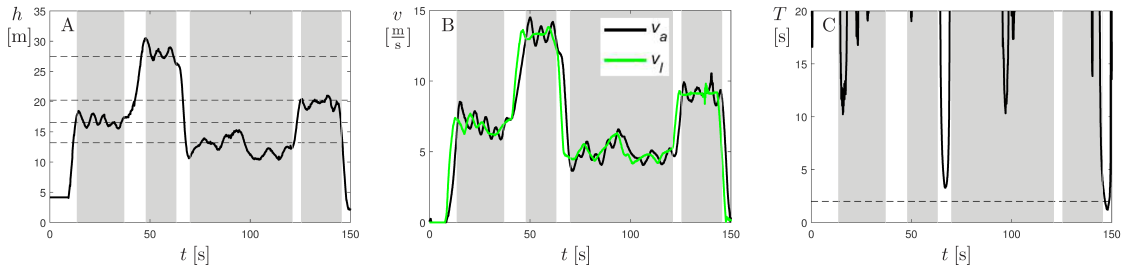

Figure 3.2: Collected data for a longitudinal car-following run with $a = 0.8$ [1/s] and $b = 0.2$ [1/s] including A: Headway of the automated vehicle relative to the leading vehicle, B: Velocities of the leading vehicle and automated vehicle, and C: Time-to-conflict vs time for one of the test runs. The time segments where the leading vehicle is trying to maintain a constant velocity and the automated vehicle settles close to steady car following are shaded in grey. In figure A, the dashed lines denote the headways corresponding to the velocities in steady state sections according to $h^* = V^{-1}(v^*)$.

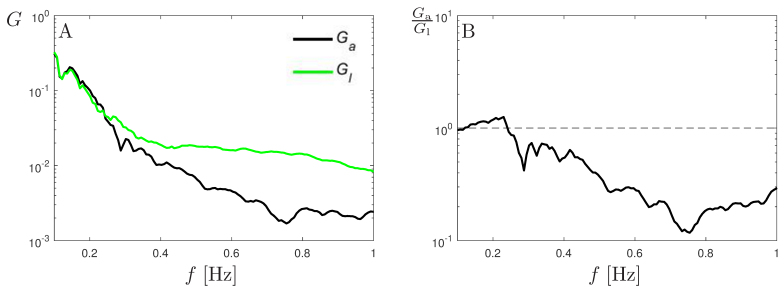

Figure 3.3: Frequency analysis of the velocities of the experimental run with $a = 0.8$ [1/s] and $b = 0.2$ [1/s] including A: the Fourier transforms of the velocities of the leading (green) and automated (black) and B: Fourier transform ratio vs frequency for the same experimental run as in Figure 3.2.

The time-to-conflict index is then given by

$$C_{\mathrm{T}}(a,b) = \int_{t_{\mathrm{st}}}^{t_{\mathrm{end}}} \mathrm{Relu}(T_{\mathrm{c}} - T(t))\mathrm{d}t \tag{3.4}$$

where the function

$$\mathrm{Relu}(u) = \begin{cases} 0 & \text{if} \quad u < 0 \\ u & \text{otherwise} \end{cases} \tag{3.5}$$

and t_{st} and t_{end} represent the start and end of each run. The value T_{c} denotes a threshold for time to conflict below which we would consider the car following to be unsafe. For our purposes we set $T_{\mathrm{c}} = 6$ [s]. Large values of C_{T} indicate that the connected automated vehicle gets close to colliding with the leading vehicle, and thus correspond to an undesirable design.

The second criterion used for parameter selection is the **string instability criterion**. We define the string instability index as

$$C_{\mathrm{s}}(a,b) = \int_{f_{\mathrm{st}}}^{f_{\mathrm{end}}} \mathrm{Relu}\left(\frac{G(f)}{G_{\mathrm{l}}(f)} - 1\right)\mathrm{d}f \tag{3.6}$$

where $G(f)$ represents the Fast Fourier Transform of the speed of the automated vehicle during each run, and likewise $G_{\mathrm{l}}(f)$ is the Fast Fourier Transform of the speed of the leading vehicle. Figure 3.3 A shows the Fast Fourier Transforms of the velocities of the leading vehicle and the following vehicle. Note that the Fast Fouier Transforms have been filtered using the Savitzky-Golay filter with a order 3 polynomial and frame length of 31 points. The ratio of the two is depicted in Figure 3.3 B. Larger values of C_{s} indicate that velocity fluctuations coming from the leading vehicle tend to get amplified by the connected

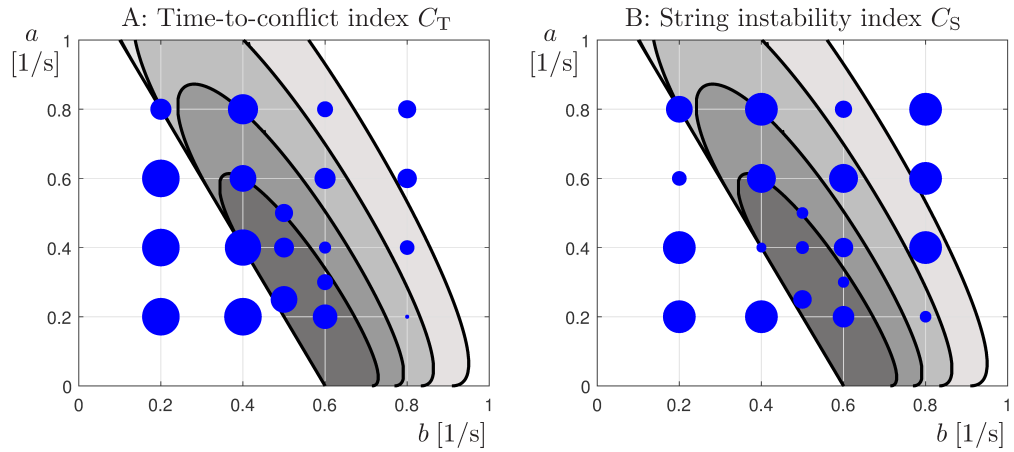

Figure 3.4: Charts in (b,a) depicting A: Time-to-conflict index and B: String instability index values for given (b,a) pairs. The values of indices are coded according to a point size scheme with an affine correlation: larger points represent larger index values. Black curves represent the analytic string stability boundaries for $\bar{\tau} = 0.55$, 0.6, 0.65, 0.7 [s] (see Appendix A). The corresponding regions of string stability are shaded grey, with darker shade corresponding to larger delay.

automated vehicle, which is not desirable and leads to congestion and loss of fuel economy [28]. In Figure 3.4 we plot the time-to-conflict and the string instability indices in the (b,a) plane using a point size scheme. The values of the indices are given by the size of the points: larger index values correspond to larger points.

To supplement the experimental criteria in the parameter selection we also use the analytic string stability boundaries for car following provided in Appendix A and [26]. The three black string stability boundaries correspond to the delays $\tau_a = 0.6$, 0.65, 0.7 s, as these are the delays observed for the connected automated vehicle with packet loss. Based on observing Figure 3.4, we chose $a = 0.4\ [1/\mathrm{s}]$ and $b = 0.5\ [1/\mathrm{s}]$ as the gains. This pair of gains yielded low values for the both the time-to-conflict index and the string instability index. This pair of gains is also located inside the analytic stability boundaries for the examined delays.

3.2 Experimental "ring road" for traffic pattern investigation

In this section we introduce an experimental framework that allows us to evaluate traffic patterns in a connected vehicle network with two connected human driven vehicles and one connected automated vehicle, as seen in Figure 3.5 A. By using the V2V communication of

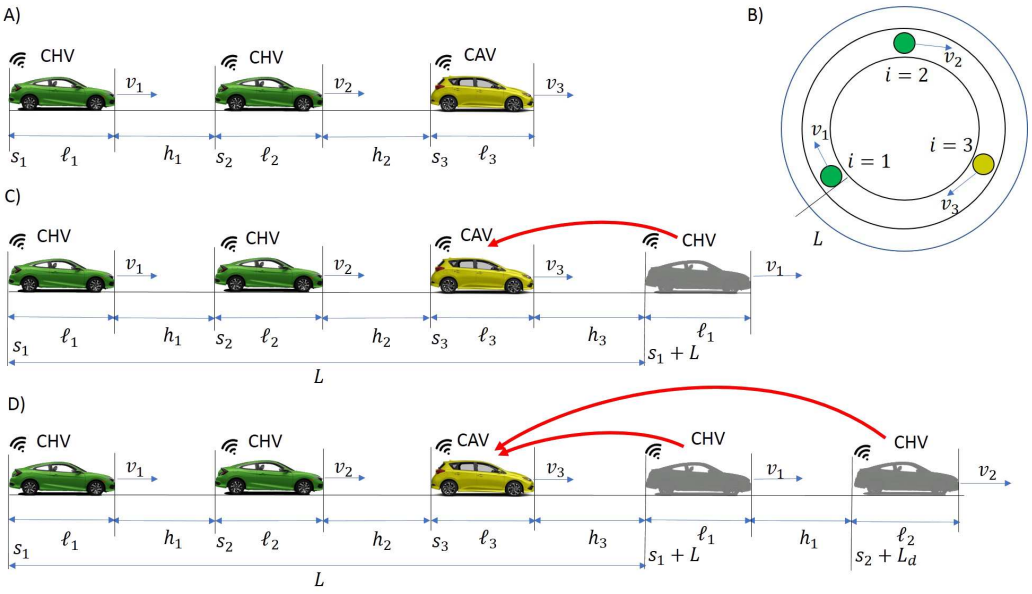

Figure 3.5: A: Connected vehicle network consisting of human-driven connected vehicles (green) and a connected automated vehicle (yellow) B: Representation of the connected vehicle network on a ring road C: The tail vehicle is projected in front of the head vehicle to provide a periodic boundary condition [11]. D: Vehicles $i = 1$ and $i = 2$ are both projected in front of the head vehicle for long-range feedback implementation

the connected automated vehicle, we are able to utilise the ring road boundary condition developed in Chapter 2 Section 2.2. This experimental framework allows us to investigate emerging traffic patterns for a wide range of traffic speeds. We then demonstrate that the traffic patterns observed in the performed experiments can be replicated by simulating the models proposed in Chapter 2 Section 2.1.

3.2.1 Experimental design

Since our goal is to evaluate traffic patterns in connected vehicle networks such as uniform flow or congestion waves, we are interested in how velocity fluctuations propagate along vehicle chains. A common way in the literature to study such problems is to place N vehicles on a circular road of length L as discussed in Section 2.2 of Chapter 2. Moreover, the average spacing of the vehicles on the ring

$$h^*_{\text{avg}} = \frac{1}{N}\left(L - \sum_{i=1}^{N} \ell_i\right) \tag{3.7}$$

can be controlled by adjusting the ring length L and/or the number of vehicles N.

This setup may allow one to study traffic patterns such as uniform flow or traveling

waves depending on parameters in the longitudinal dynamics and the average spacing (3.7). This setup was used in [93] to demonstrate the formation on traffic jams with human-driven vehicles, while in [91] and automated vehicle was placed among human-driven cars and it was shown that it can mitigate congestion by keeping a large distance to its predecessor. However, the speeds and vehicle spacings achieved in these experiments had to be kept low (below 10 $[\mathrm{m/s}]$) in order to keep the lateral acceleration within a comfortable limit and allow drivers to focus on longitudinal control rather than steering. That is, this setup makes it very challenging to evaluate the traffic patterns for realistic speeds.

To solve this problem we propose to use V2V connectivity in order to establish periodic boundary conditions without having vehicles to drive on a ring. The key idea is to allow that head vehicle of an open chain to observe the motion of the tail vehicle of the chain. Then, by adding the ring length L to the longitudinal coordinate of the last vehicle it can be virtually placed ahead of the connected automated vehicle (CAV) as illustrated in Figure 3.5 A,C for a three-vehicle chain [11]. In this case, the head vehicle (yellow) is a CAV which is followed by two CHVs. Then using $s_1 + L$ in the controllers of the connected automated vehicle the CHV $i = 1$ can be "placed" in front of it. This setup allows the human drivers to drive at realistic speed ranges while "closing the ring" via V2V communication.

Moreover, the established periodic boundary condition allows one to evaluate the impact of a connected automated vehicle on traffic flow for different ring lengths (and average vehicle spacings) and different communication strategies. Indeed, the idea can be extended to scenarios when a connected automated vehicle responds to the motion of multiple vehicles ahead and allows us to evaluate the impact of connected automated vehicles on traffic flow. Specifically Figure 3.6 C shows the **nearest-neighbor feedback** configuration, where the CAV responds only to CHV $i = 1$, while Figure 3.6 D shows the **long-range feedback** configuration, where the CAV responds to CHV $i = 1$ and CHV $i = 2$. In this chapter we experimentally compare the traffic patterns emerging in the nearest-network feedback configuration and the long-range feedback configuration.

3.2.2 Experimental results

We performed experiments on a straight public road with the connected automated vehicle set up so that the connected vehicles were in the communication range at all times. Here the CAV uses the car following controller given by (2.13,2.14,2.6,2.15) to prescribe the acceleration. The headway and relative velocity gains are tuned to $a = 0.4$ and $b = 0.5$ [1/s], see Section 3.1. For the nearest-neighbor feedback we set $E_3^k = \{1\}$ and weight $w_{3,1} = 1\,[1/\mathrm{s}]$ while for the long-range feedback we set $E_3^k = \{1,2\}$ and weights $w_{3,1} = 0.4\,[1/\mathrm{s}]$, $w_{3,2} = 0.6\,[1/\mathrm{s}]$,

c.f. (2.15). Also we considered scenarios with $\kappa = 0.6\ [1/\mathrm{s}]$ and $\kappa = 1.0\ [1/\mathrm{s}]$ to observe the effects of the "aggresiveness" of the automated vehicle. In particular, we studied three scenarios as outlined in Table 3.1. For each κ the ring length L (and consequently the average vehicle spacing h^*_{avg}) was varied, as seen in Table 3.1 to account for different uniform flow speeds up to about 24 [m/s]. For each experiment the vehicles started from a stationary configuration and then were given some time to approach either a steady state where they traveled close to uniform flow or reached steady oscillatory behavior during which they periodically slowed down and speeded up.

Table 3.1: Experimental scenarios for three car connected vehicle network

Feedback	**Ring Lengths Examined**	**Average Spacings Examined**
$\kappa = 0.6$ [1/s] nearest-neighbor	$L \in \{30, 45, \ldots, 135\}$ [m]	$h^*_{\mathrm{avg}} \in \{5, 10, \ldots, 40\}$ [m]
$\kappa = 1.0$ [1/s] nearest-neighbor	$L \in \{30, 45, \ldots, 90\}$ [m]	$h^*_{\mathrm{avg}} \in \{5, 10, \ldots, 25\}$ [m]
$\kappa = 1.0$ [1/s] long-range	$L \in \{30, 45, \ldots, 90\}$ [m]	$h^*_{\mathrm{avg}} \in \{5, 10, \ldots, 25\}$ [m]

The first column of Figure 3.6 show time profiles of the headways and velocities of the three vehicles for $h^*_{\mathrm{avg}} = 15\ [\mathrm{m}]$, with the first two rows corresponding to nearest-neighbor feedback with $\kappa = 0.6\ [1/\mathrm{s}]$, the second two rows corresponding to the nearest-neighbor feedback with $\kappa = 1.0\ [1/\mathrm{s}]$, and the last two rows corresponding to the long-range feedback with $\kappa = 1.0\ [1/\mathrm{s}]$.

For $\kappa = 0.6\ [1/\mathrm{s}]$ (see Figure 3.6 A, C) the vehicles accelerate from a standstill and approach uniform flow, where they travel at a constant velocity around 12 [m/s]. This corresponds to the equilibrium speed predicted by the car following models (see black dashed line). When we set $\kappa = 1.0\ [1/\mathrm{s}]$ (see Figure 3.6 E, G), the vehicles approach a state where their speed and headway oscillate. In this case the uniform flow is unstable and the uniform flow velocity would be around 15 [m/s] that is close to the average velocities of the vehicles during the steady oscillations. Lastly, when we introduce long-range feedback with $\kappa = 1.0\ [1/\mathrm{s}]$ vehicles approach uniform flow (see Figure 3.6 J, L). Here, the uniform flow velocity is also about 15 [m/s] and the vehicles are able to sustain this state and no oscillations develop.

To show that the above traffic behavior is captured by the vehicle models developed in Section 2.1 of this chapter, we also plot the corresponding model-matched simulation results in the right column of Figure 3.6. In particular, model matching was used to select the parameters α_i, β_i and τ_i for the human-driven vehicles $i = 1, 2$, see Appendix B for details. We found that, while these parameters may vary in time and from driver to driver,

using approximations $\alpha_1 = \alpha_2$, $\beta_1 = \beta_2$ and $\tau_1 = \tau_2$ we are able to reproduce the behavior of the individual vehicles and that of the connected vehicle network sufficiently well.

From the experiments and the model matched simulations we see that for the one-car-look-ahead configuration, choosing between $\kappa = 0.6$ [1/s] and $\kappa = 1.0$ [1/s] is a tradeoff between speed and stability of uniform flow. For a given spacing h^*_{avg} decreasing κ decreases the overall velocity of the vehicles, while increasing κ would make the network more susceptible to developing undesirable oscillations. The above tradeoff can be resolved by using a long-range feedback, where even with the more aggressively tuned $\kappa = 1.0$ [1/s] the connected vehicle network is able to sustain uniform flow at a higher speed. It is demonstrated that by getting information from multiple vehicles ahead, we are able to improve the throughput of the network without making it susceptible to oscillating behavior. This has been verified by multiple experiments using different initial conditions.

3.3 Summary

In this section we developed a controller for a connected automated vehicle and investigated the traffic patterns formed when this vehicle interacted with human-driven vehicles. To tune the gains of the car-following controller we used an open chain configuration, where the connected automated vehicle followed a connected human-driven vehicle while the human was driving according to a pre-defined speed profile. Experimental criteria were developed and applied to the collected data to tune the controller in addition to standard analytical criteria.

After tuning the controller for the connected automated vehicle, we placed it together with two connected human-driven vehicles into a three-car connected vehicle network. We used the ring configuration to ensure that traffic patterns form and persist for just three vehicles. Our experimental design used the connected automated vehicle to ensure the ring boundary condition so that we could observe speeds of up to 24 [m/s] without taking lateral dynamics into account. In these experiments we observed that when the connected automated vehicle relied only on the information of the preceding vehicle, pushing the vehicles closer together yielded traffic waves rather than uniform flow. Using long range feedback however allows us to push the vehicles closer together and ensure stable uniform flow. Lastly we showed that modeling car following via delayed differential equations allows us to replicate the behavior of the connected vehicle network as well as individual vehicles observed in experiments.

These experimental results motivated us to study traffic patterns in large connected

vehicle networks as it is important to see whether traffic patterns change for a large number of vehicles. Because modeling car following via differential equations allowed us to replicate experimental results, we will perform this investigation by analyzing and simulating these equations.

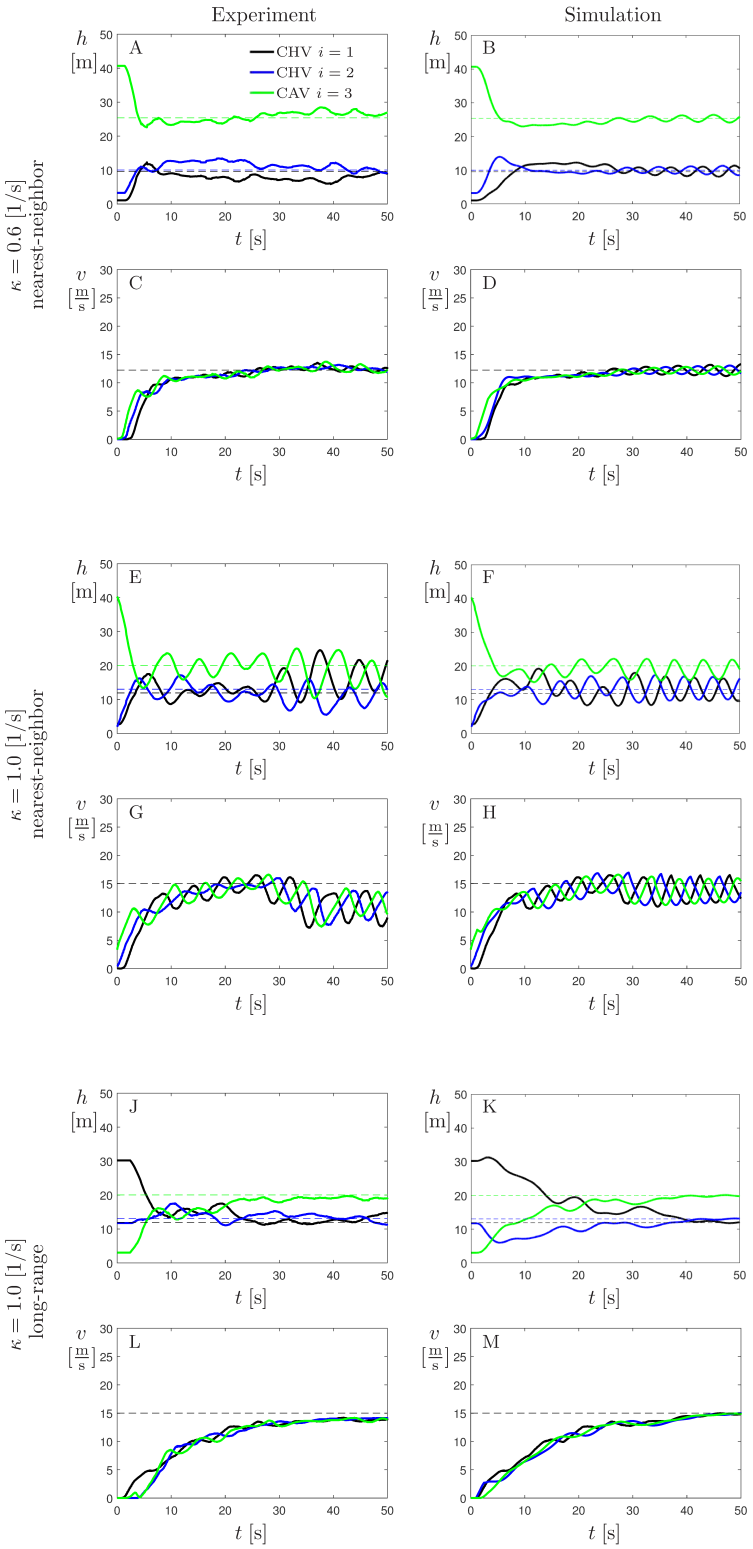

Figure 3.6: Time profiles of headways and velocities for vehicles in connected vehicle network with average spacing $h^* = 15$ [m] from the experiment (left column) and model matched simulations (right column) for the three scenarios presented in Table II.

CHAPTER 4

Network-based nonlinear analysis of human driven traffic

As seen from (2.1,2.3), equations governing car following for human drivers feature several nonlinearities including the saturation in the range policy and the saturation in acceleration. Consequently, we need to analyze the nonlinear dynamics of the arising connected vehicle systems. Of specific interest is to identify the domains of bistability in the parameter space where smooth traffic flow can be achieved, but sufficiently large perturbations may lead to stop-and-go traffic jams [22, 37, 65, 67]. In [37] the critical densities at which bistability appears were derived analytically for a simplified model, while nonlinear oscillatory solutions were characterized in [22] using Hopf calculations and numerical continuation. By extending these techniques to infinite dimensional state spaces, the effects of driver reaction time were investigated in [65, 67]. While these techniques were successful when considering simplified human-driver models, they become cumbersome and inefficient when considering more complicated connected cruise control strategies. This demands new tools for the analysis of nonlinear networked systems to allow fast controller prototyping where the control algorithms can be designed at the vehicle level but their impact on the large-scale dynamics can also be evaluated.

One way to characterize nonlinear dynamics of high-dimensional systems is to identify the so-called nonlinear normal modes (NNMs). Here we briefly discuss the history of NNMs and refer the reader to the comprehensive summary presented in [41]. The concept of NNMs can be traced back to Rosenberg [79], where he defined them as “vibrations-in-unison of the system". Shaw and Pierre expanded this definition in [84] to “a motion that takes place on a two-dimensional invariant manifold embedded in state space". (The manifold was two-dimensional since they were concerned about mechanical systems constructed of one-degree-of-freedom elements, but the concept can be generalized to higher dimensional manifolds.) By exploiting the invariance of these nonlinear manifolds, they presented an analytical method for the approximation of NNMs that led to algebraic equations. Other

analytical techniques used to compute NNMs include various energy-based methods [49, 79]; the method of multiple scales [30, 58, 102]; the method of normal forms [38, 57]; and the harmonic balance method [35, 96]. These analytical methods were applied to systems consisting of small numbers of oscillators due to the complexity of the calculations.

In [41] it was suggested that numerical continuation [16, 89] may be used to extend NNM analysis to systems containing larger numbers of oscillators. The practicality of continuation in NNM analysis was demonstrated in [69] along with several applications to mechanical systems, while in [31, 32] continuation was used to obtain NNMs for structures with cyclic symmetry containing up to 60 oscillators. However, beyond this limit numerical continuation becomes unfeasible due to high computational demand. Furthermore, when using numerical methods one loses the intuition that can be gained when applying analytical approaches.

The analysis of networked systems with large numbers of nodes is not feasible with the current analytical and numerical methods since they lead to large numbers of coupled linear algebraic equations that need to be solved simultaneously to obtain the modal equations. Our goal is to extend these limitations by exploiting the network structure. Using network-based linear and nonlinear transformations we decompose the system into uncoupled nonlinear modal equations. Each modal equation can be obtained by solving a small number of algebraic equations without considering the other modes. When bifurcations occur in the corresponding modal subspace normal forms can be used to characterize the nonlinear behavior of the entire system.

In this chapter we present the mathematical methods for systems with cyclic structure and apply the developed tools to investigate the dynamics of a connected vehicle system where each vehicle utilizes information about the motion of the vehicle immediately ahead; see Fig. 2.1(b). In Section 4.2 we develop a network-based algorithm for decomposing general systems with cyclic symmetry into nonlinear modes. In Section 4.3 we apply this algorithm to analyze nonlinear oscillations arising through a Hopf bifurcation in a connected vehicle system consisting of conventional vehicles. Analytical results are compared to those of numerical continuation in Section 4.4, where we evaluate the effects of the driver model parameters on the dynamics of the network. Finally, we discuss the implications of the developed network-based algorithms in 4.5.

4.1 Simplified model for human-driven car following

In this section we analyze the connected vehicle network in a ring configuration (see Subsection 2.2.2) composed of human drivers. To develop analytical tools for observing

behaviors of large vehicle networks in this chapter we simplify the human (2.1,2.3) by excluding the acceleration saturation $f_{\text{sat}}(\cdot)$ as well as the delay, however note that a similar analysis can be performed with both for a sufficiently small network, see [45]. For simplicity we also consider that all the human drivers have the same parameters, i.e. $\alpha_i = \alpha$, $\beta_i = \beta$, $V_i(h) = V(h)$ for $i = 1 \dots N$. Thus in this scenario, the dynamics of each vehicle can be represented by two ordinary differential equations

$$\begin{aligned} \dot{s}_i &= v_i \\ \dot{v}_i &= \alpha\Big(V(h_i) - v_i\Big) + \beta\Big(v_{i+1} - v_i\Big) \end{aligned} \tag{4.1}$$

Where the range policy is the one defined by (2.5,2.8) due to the fact that it has continuous first derivatives, although similar analysis can be performed for the range policies shown in Figure 2.2 E. We consider the system around uniform flow defined in (2.18-2.22) define the perturbations

$$\widetilde{s}_i = s_i - s_i^*, \qquad \widetilde{v}_i = v_i - v^*, \tag{4.2}$$

and approximate the system about the pseudo-equilibrium (2.18,2.19) up to the cubic order using Taylor expansion that yields

$$\begin{aligned} \dot{\widetilde{s}}_i &= \widetilde{v}_i, \\ \dot{\widetilde{v}}_i &= p\,(\widetilde{s}_{i+1} - \widetilde{s}_i) + \frac{q}{2}(\widetilde{s}_{i+1} - \widetilde{s}_i)^2 + \frac{r}{6}(\widetilde{s}_{i+1} - \widetilde{s}_i)^3 + \beta_1\,(\widetilde{v}_{i+1} - \widetilde{v}_i) - \alpha\,\widetilde{v}_i, \end{aligned} \tag{4.3}$$

where

$$\begin{aligned} p &= \alpha V'(h^*), \\ q &= \alpha V''(h^*), \\ r &= \alpha V'''(h^*), \end{aligned} \tag{4.4}$$

and the prime denotes the derivative with respect to the headway h. In this chapter we use the approximation (4.3) to develop network-based methods to analyze patterns in networks of human-driven vehicles.

4.2 Nonlinear network-based analysis

In this section we develop methods for the nonlinear analysis of a general system with cyclic structure. For simplicity, we present the result for two equations per node and unidirectional nearest-neighbor coupling, but the approach can be generalized for arbitrary number of

equations per node and more general coupling structures that admit $\mathbb{Z}_N$ symmetry. We investigate the system in the vicinity of a uniform equilibrium, where we approximate the dynamics using Taylor expansion up to third order. We then write the quadratic and cubic terms of the approximated system into a compact form, which allows us to perform a series of linear and nonlinear network-based transformations. These transformations result in nonlinear modal equations that are decoupled and can be analyzed separately in order to characterize the dynamics of the entire system.

Consider a system composed of N nodes arranged in a cyclic structure where the $i+1$-st node is connected to the i-th node and the first node is connected to the N-th node; see Fig. 2.1 B. Assuming that the state of the i-th node is described by the vector $\mathbf{x}_i = [x_i^{(1)}\, x_i^{(2)}]^{\mathrm{T}}$, where T denotes the transpose, the dynamics of the i-th node can be written into the form

$$\dot{\mathbf{x}}_i = \mathbf{g}(\mathbf{x}_i, \mathbf{x}_{i+1}), \tag{4.5}$$

for $i = 1, \ldots, N$, where $\mathbf{g} = [g^{(1)}\, g^{(2)}]^{\mathrm{T}}$ and $\mathbf{x}_{N+1} \equiv \mathbf{x}_1$. We assume that the system possesses a uniform equilibrium

$$\mathbf{x}_i^* = \mathbf{x}^*, \tag{4.6}$$

for $i = 1, \ldots, N$ which satisfies $\mathbf{g}(\mathbf{x}^*, \mathbf{x}^*) = 0$.

By defining the perturbation

$$\mathbf{y}_i = \mathbf{x}_i - \mathbf{x}^*, \tag{4.7}$$

where $\mathbf{y}_i = [y_i^{(1)}\, y_i^{(2)}]^{\mathrm{T}}$, the third-order Taylor approximation of (4.5) around the equilibrium (4.6) can be written as

$$\begin{aligned}\dot{\mathbf{y}}_i = {} & [\mathfrak{J}_0]^* \mathbf{y}_i + [\mathfrak{J}_1]^* \mathbf{y}_{i+1} + \frac{1}{2} \sum_{b=0,1} \sum_{\beta=1,2} \mathbf{H}_b^{(\beta)}(\mathbf{y}_{i+b}) \left([\partial_b^{(\beta)} \mathfrak{J}_0]^* \mathbf{y}_i + [\partial_b^{(\beta)} \mathfrak{J}_1]^* \mathbf{y}_{i+1} \right) \\ & + \frac{1}{6} \sum_{b=0,1} \sum_{\beta=1,2} \sum_{d=0,1} \sum_{\delta=1,2} \mathbf{H}_b^{(\beta)}(\mathbf{y}_{i+b})\, \mathbf{H}_d^{(\delta)}(\mathbf{y}_{i+d}) \left([\partial_b^{(\beta)} \partial_d^{(\delta)} \mathfrak{J}_0]^* \mathbf{y}_i + [\partial_b^{(\beta)} \partial_d^{(\delta)} \mathfrak{J}_1]^* \mathbf{y}_{i+1} \right),\end{aligned} \tag{4.8}$$

where $\partial_b^{(\beta)} = \frac{\partial}{\partial x_{i+b}^{(\beta)}}$, and the operators

$$\mathfrak{J}_b = \begin{bmatrix} \partial_b^{(1)} g^{(1)} & \partial_b^{(2)} g^{(1)} \\ \partial_b^{(1)} g^{(2)} & \partial_b^{(2)} g^{(2)} \end{bmatrix}, \tag{4.9}$$

where $b = 0, 1$ represent the derivatives of the function $\mathbf{g}$. In (4.8) the asterisk denotes that

the derivatives are evaluated at the equilibrium. The quadratic and cubic terms contain the diagonal matrices

$$\mathbf{H}_b^{(\beta)}(\mathbf{y}_i) = \begin{bmatrix} y_{i+b}^{(\beta)} & 0 \\ 0 & y_{i+b}^{(\beta)} \end{bmatrix}, \tag{4.10}$$

for $\beta = 1,2$, $b = 0,1$, and $i = 1,\ldots,N$. The matrix $\mathbf{H}_0^{(\beta)}(\mathbf{y}_i)$ is related to the self-feedback (the dependence of a node's dynamics on its own states), while $\mathbf{H}_1^{(\beta)}(\mathbf{y}_{i+1})$ is related to the coupling (the dependence of a node's dynamics on the state of the neighboring node). We remark that the double sum in (4.8) results in 4 different quadratic terms while the quadruple sum results in 10 different cubic terms.

4.2.1 Network Structure

Before we proceed with the general analysis we rewrite (4.8) into a form that allows us to take advantage of the cyclic structure during the linear and nonlinear analysis. In order to do this we first define the direct product (or Kronecker product) of matrices $\mathbf{B} = [b_{ij}] \in \mathbb{C}^{N\times M}$ and $\mathbf{C} \in \mathbb{C}^{P\times Q}$ as

$$\mathbf{B}\otimes\mathbf{C} = \begin{bmatrix} b_{11}\mathbf{C} & b_{12}\mathbf{C} & \cdots & b_{1M}\mathbf{C} \\ b_{21}\mathbf{C} & b_{22}\mathbf{C} & \cdots & b_{2M}\mathbf{C} \\ \vdots & \vdots & \ddots & \vdots \\ b_{N1}\mathbf{C} & b_{N2}\mathbf{C} & \cdots & b_{NM}\mathbf{C} \end{bmatrix}, \tag{4.11}$$

where $\mathbf{B}\otimes\mathbf{C} \in \mathbb{C}^{NP\times MQ}$. We also define the vector $\hat{\mathbf{y}} = \mathrm{col}[\mathbf{y}_1 \cdots \mathbf{y}_i \cdots \mathbf{y}_N]$, where the operator $\mathrm{col}[\cdot]$ stacks vectors into one large column vector. Thus, using (4.8) and (4.11) the dynamics of the entire system can be written into the form

$$\begin{aligned}\dot{\hat{\mathbf{y}}} = &\left(\mathbf{I}_N\otimes[\mathfrak{J}_0]^* + \mathbf{A}_N\otimes[\mathfrak{J}_1]^*\right)\hat{\mathbf{y}} + \frac{1}{2}\sum_{b=0,1}\sum_{\beta=1,2}\hat{\mathfrak{L}}^{(\beta)}\left(\hat{\mathbf{H}}_b(\hat{\mathbf{y}})\right)\left(\mathbf{I}_N\otimes[\partial_b^{(\beta)}\mathfrak{J}_0]^* + \mathbf{A}_N\otimes[\partial_b^{(\beta)}\mathfrak{J}_1]^*\right)\hat{\mathbf{y}} \\ &+ \frac{1}{6}\sum_{b=0,1}\sum_{\beta=1,2}\sum_{d=0,1}\sum_{\delta=1,2}\hat{\mathfrak{L}}^{(\beta)}\left(\hat{\mathbf{H}}_b(\hat{\mathbf{y}})\right)\hat{\mathfrak{L}}^{(\delta)}\left(\hat{\mathbf{H}}_d(\hat{\mathbf{y}})\right)\left(\mathbf{I}_N\otimes[\partial_b^{(\beta)}\partial_d^{(\delta)}\mathfrak{J}_0]^* + \mathbf{A}_N\otimes[\partial_b^{(\beta)}\partial_d^{(\delta)}\mathfrak{J}_1]^*\right)\hat{\mathbf{y}},\end{aligned} \tag{4.12}$$

where $\mathbf{I}_N$ is the N-dimensional identity matrix and $\mathbf{A}_N = [a_{ij}]$ is the N-dimensional adjacency matrix with circulant structure, whose elements are defined as

$$a_{ij} = \begin{cases} 1 & \text{if} \quad j = i+1\,, \\ 0 & \text{otherwise}\,. \end{cases} \tag{4.13}$$

As mentioned above, for $i = N$ we have $j = 1$. The Jacobian matrix in (4.12) contains the blocks $[\mathfrak{J}_0]^*$ along the diagonal and the blocks $[\mathfrak{J}_1]^*$ above the diagonal representing the self-coupling and the effects of the neighbors, respectively.

The nonlinear self-feedback terms feature the $2N$-dimensional diagonal matrix

$$\hat{\mathbf{H}}_0(\hat{\mathbf{y}}) = \mathrm{diag}\left(\begin{bmatrix} y_i^{(1)} & 0 \\ 0 & y_i^{(2)} \end{bmatrix} \right), \tag{4.14}$$

where the operator $\mathrm{diag}(\cdot)$ is defined by

$$\mathrm{diag}(\mathbf{B}_i) = \mathrm{diag}(\mathbf{B}_1, \mathbf{B}_2, \ldots, \mathbf{B}_N) = \begin{bmatrix} \mathbf{B}_1 & \mathbf{0} & \ldots & \mathbf{0} \\ \mathbf{0} & \mathbf{B}_2 & \ldots & \mathbf{0} \\ \vdots & \vdots & \ddots & \vdots \\ \mathbf{0} & \mathbf{0} & \ldots & \mathbf{B}_N \end{bmatrix}, \tag{4.15}$$

as adopted from [59]. To be able to represent the nonlinear coupling terms, we shift the blocks along the diagonal in a circulant manner using

$$\hat{\mathbf{H}}_1(\hat{\mathbf{y}}) = (\mathbf{A}_N \otimes \mathbf{I})\, \hat{\mathbf{H}}_0(\hat{\mathbf{y}})\, (\mathbf{A}_N^{-1} \otimes \mathbf{I}) = \mathrm{diag}\left(\begin{bmatrix} y_{i+1}^{(1)} & 0 \\ 0 & y_{i+1}^{(2)} \end{bmatrix} \right), \tag{4.16}$$

where $\mathbf{I}$ is the 2-dimensional identity matrix. Matrices (4.14) and (4.16) are the basic building blocks for the quadratic and cubic terms for the system dynamics. To be able to express all possible terms we shuffle the variables within the blocks of $\hat{\mathbf{H}}_0(\hat{\mathbf{y}})$ and $\hat{\mathbf{H}}_1(\hat{\mathbf{y}})$. First, we define two linear shuffling operators $\mathfrak{L}^{(1)}$ and $\mathfrak{L}^{(2)}$ whose action on the diagonal matrix

$$\mathbf{M} = \begin{bmatrix} \mu & 0 \\ 0 & \upsilon \end{bmatrix}, \tag{4.17}$$

is given by

$$\begin{aligned} \mathfrak{L}^{(1)}(\mathbf{M}) &= \begin{bmatrix} 1 & 0 \\ 0 & 0 \end{bmatrix} \mathbf{M} \begin{bmatrix} 1 & 0 \\ 0 & 0 \end{bmatrix} + \begin{bmatrix} 0 & 0 \\ 1 & 0 \end{bmatrix} \mathbf{M} \begin{bmatrix} 0 & 1 \\ 0 & 0 \end{bmatrix} = \begin{bmatrix} \mu & 0 \\ 0 & \mu \end{bmatrix}, \\ \mathfrak{L}^{(2)}(\mathbf{M}) &= \begin{bmatrix} 0 & 0 \\ 0 & 1 \end{bmatrix} \mathbf{M} \begin{bmatrix} 0 & 0 \\ 0 & 1 \end{bmatrix} + \begin{bmatrix} 0 & 1 \\ 0 & 0 \end{bmatrix} \mathbf{M} \begin{bmatrix} 0 & 0 \\ 1 & 0 \end{bmatrix} = \begin{bmatrix} \upsilon & 0 \\ 0 & \upsilon \end{bmatrix}. \end{aligned} \tag{4.18}$$

Consequently, considering a block matrix $\hat{\mathbf{M}} \in \mathbb{C}^{2N\times 2N}$ with 2×2 diagonal blocks

$$\hat{\mathbf{M}}_{ij} = \begin{bmatrix} \mu_{ij} & 0 \\ 0 & \upsilon_{ij} \end{bmatrix}, \tag{4.19}$$

we can define the shuffling operators

$$\begin{aligned}
\hat{\mathfrak{L}}^{(1)}(\hat{\mathbf{M}}) &= \left(\mathbf{I}_N \otimes \begin{bmatrix} 1 & 0 \\ 0 & 0 \end{bmatrix}\right)\hat{\mathbf{M}}\left(\mathbf{I}_N \otimes \begin{bmatrix} 1 & 0 \\ 0 & 0 \end{bmatrix}\right) + \left(\mathbf{I}_N \otimes \begin{bmatrix} 0 & 0 \\ 1 & 0 \end{bmatrix}\right)\hat{\mathbf{M}}\left(\mathbf{I}_N \otimes \begin{bmatrix} 0 & 1 \\ 0 & 0 \end{bmatrix}\right), \\
\hat{\mathfrak{L}}^{(2)}(\hat{\mathbf{M}}) &= \left(\mathbf{I}_N \otimes \begin{bmatrix} 0 & 0 \\ 0 & 1 \end{bmatrix}\right)\hat{\mathbf{M}}\left(\mathbf{I}_N \otimes \begin{bmatrix} 0 & 0 \\ 0 & 1 \end{bmatrix}\right) + \left(\mathbf{I}_N \otimes \begin{bmatrix} 0 & 1 \\ 0 & 0 \end{bmatrix}\right)\hat{\mathbf{M}}\left(\mathbf{I}_N \otimes \begin{bmatrix} 0 & 0 \\ 1 & 0 \end{bmatrix}\right),
\end{aligned} \tag{4.20}$$

where the blocks are given by

$$[\hat{\mathfrak{L}}^{(1)}(\hat{\mathbf{M}})]_{ij} = \begin{bmatrix} \mu_{ij} & 0 \\ 0 & \mu_{ij} \end{bmatrix}, \qquad [\hat{\mathfrak{L}}^{(2)}(\hat{\mathbf{M}})]_{ij} = \begin{bmatrix} \upsilon_{ij} & 0 \\ 0 & \upsilon_{ij} \end{bmatrix}. \tag{4.21}$$

We remark that for the more general case, when the dynamics of each node are given by n differential equations, we need to define n shuffling operators with similar structure to (4.20). Notice the similarity of structure of the linear, quadratic, and cubic terms in (4.12). In the next section we exploit this structure while performing network-based coordinate transformations.

4.2.2 Linear Modal Transformation

Prior to applying network-based nonlinear transformations, we transform the system to modal coordinates using the linear coordinate transformation

$$\hat{\mathbf{y}} = (\mathbf{T}_N \otimes \mathbf{I})\,\hat{\mathbf{z}}, \tag{4.22}$$

where the modal coordinates are defined as $\mathbf{z}_k = [z_k^{(1)}\, z_k^{(2)}]^{\mathrm{T}}$, $\hat{\mathbf{z}} = \mathrm{col}\,[\mathbf{z}_0\ \ldots\ \mathbf{z}_k\ \ldots\ \mathbf{z}_{N-1}]$. Moreover, $\mathbf{T}_N = \begin{bmatrix} \mathbf{e}_0 & \cdots & \mathbf{e}_k & \cdots & \mathbf{e}_{N-1} \end{bmatrix}$, where $\mathbf{e}_k$ is the k-th eigenvector of the adjacency matrix $\mathbf{A}_N$ corresponding to the k-th modal eigenvalue $\mathrm{e}^{\mathrm{i}\frac{2\pi k}{N}}$, so that $\mathrm{i}^2 = -1$ and $k = 0,\ldots,N-1$. Notice that the mode number $k = 0$ corresponds to a translational symmetry of the system, the mode numbers $k = 1,\ldots,\lfloor\frac{N}{2}\rfloor$ correspond to having k waves along the ring, while the mode numbers $k = \lceil\frac{N}{2}\rceil,\ldots,N-1$ correspond to having $N-k$ waves along

the ring [59, 66]. Using the modal coordinates (4.12) can be written as

$$\dot{\hat{\mathbf{z}}} = \hat{\mathbf{D}}\,\hat{\mathbf{z}} + \frac{1}{2}\sum_{b=0,1}\sum_{\beta=1,2}\hat{\mathfrak{L}}^{(\beta)}\big(\hat{\mathbf{S}}_b(\hat{\mathbf{z}})\big)\,\hat{\mathbf{K}}_b^{(\beta)}\,\hat{\mathbf{z}} + \frac{1}{6}\sum_{b=0,1}\sum_{\beta=1,2}\sum_{d=0,1}\sum_{\delta=1,2}\hat{\mathfrak{L}}^{(\beta)}\big(\hat{\mathbf{S}}_b(\hat{\mathbf{z}})\big)\,\hat{\mathfrak{L}}^{(\delta)}\big(\hat{\mathbf{S}}_d(\hat{\mathbf{z}})\big)\hat{\mathbf{L}}_{bd}^{(\beta\,\delta)}\hat{\mathbf{z}}. \tag{4.23}$$

Here the matrix

$$\hat{\mathbf{D}} = \mathrm{diag}(\mathbf{D}_k), \tag{4.24}$$

is block diagonal and the 2×2 block for mode k is given by

$$\mathbf{D}_k = [\mathfrak{J}_0]^* + [\mathfrak{J}_1]^*\,\mathrm{e}^{\mathrm{i}\frac{2\pi k}{N}}, \tag{4.25}$$

for $k = 0,\ldots,N-1$. Note that the block $\mathbf{D}_k$ is in fact the $k+1$-st block along the diagonal due to the presence of modal index 0. The matrices $\hat{\mathbf{S}}_b(\hat{\mathbf{z}}) \in \mathbb{C}^{2N\times 2N}$, $b = 0, 1$ in (4.23) have block structures such that the blocks are given by

$$\mathbf{S}_{0k\ell}(\mathbf{z}_{f_{k\ell}}) = \begin{bmatrix} z^{(1)}_{f_{k\ell}} & 0 \\ 0 & z^{(2)}_{f_{k\ell}} \end{bmatrix}, \qquad \mathbf{S}_{1k\ell}(\mathbf{z}_{f_{k\ell}}) = \begin{bmatrix} \mathrm{e}^{\mathrm{i}\frac{2\pi(k-\ell)}{N}} z^{(1)}_{f_{k\ell}} & 0 \\ 0 & \mathrm{e}^{\mathrm{i}\frac{2\pi(k-\ell)}{N}} z^{(2)}_{f_{k\ell}} \end{bmatrix}, \tag{4.26}$$

where the function

$$f_{k\ell} = \begin{cases} k-\ell & \text{if} \quad k \geq \ell, \\ N+k-\ell & \text{if} \quad k < \ell, \end{cases} \tag{4.27}$$

defines the modal indices for the blocks and dictates the cyclic structure of the nonlinear terms.

Since the coefficient matrices in the quadratic and cubic terms of (4.12) have the same block structure as the Jacobian, they are also diagonalized by the linear modal transformation. The quadratic terms contain the block-diagonal matrix

$$\hat{\mathbf{K}}_b^{(\beta)} = \mathrm{diag}(\mathbf{K}_{bk}^{(\beta)}), \tag{4.28}$$

with 2×2 blocks

$$\mathbf{K}_{bk}^{(\beta)} = [\partial_b^{(\beta)}\mathfrak{J}_0]^* + [\partial_b^{(\beta)}\mathfrak{J}_1]^*\,\mathrm{e}^{\mathrm{i}\frac{2\pi k}{N}}, \tag{4.29}$$

for $k = 0,\ldots,N-1$, while the cubic terms contain the block-diagonal matrix

$$\hat{\mathbf{L}}_{bd}^{(\beta\,\delta)} = \mathrm{diag}(\mathbf{L}_{bdk}^{(\beta\,\delta)}), \tag{4.30}$$

with 2×2 blocks

$$\mathbf{L}_{bdk}^{(\beta\,\delta)} = [\partial_b^{(\beta)} \partial_d^{(\delta)} \mathfrak{J}_0]^* + [\partial_b^{(\beta)} \partial_d^{(\delta)} \mathfrak{J}_1]^* \mathrm{e}^{\mathrm{i}\frac{2\pi k}{N}}, \tag{4.31}$$

for $k = 0, \ldots, N-1$. The asterisk in (4.29) and (4.31) still indicates that the matrices are evaluated at the equilibrium.

The linear coordinate transformation (4.22) serves two purposes. First, it simplifies the linear analysis of the system: the linear part is decoupled into N pairs of complex differential equations, representing the oscillation modes. Thus, linear stability can be analyzed separately for each mode and stability is ensured when all the modes are stable. Moreover, the transformation (4.22) block-diagonalizes the nonlinear coefficient matrices in the quadratic and cubic terms (notice the similarity between (4.24,4.25), (4.28,4.29), and (4.30,4.31)), and transforms the matrices $\hat{\mathbf{H}}_0(\hat{\mathbf{y}})$ and $\hat{\mathbf{H}}_1(\hat{\mathbf{y}})$ into modal matrices $\hat{\mathbf{S}}_0(\hat{\mathbf{z}})$ and $\hat{\mathbf{S}}_1(\hat{\mathbf{z}})$, cf. (4.12,4.23). The cyclic structure (4.27), that appears in both the quadratic and the cubic terms, allows us to define nonlinear near-identity transformations for cyclic systems.

4.2.3 Nonlinear network-based coordinate transformations

After obtaining the modal coordinates where the linear terms are decoupled, we proceed to simplify the quadratic and cubic terms using network-based transformations. These transformations exploit the structure of the network and allow us to eliminate the second-order and third-order terms for a given mode by solving a small number of algebraic equations. Specifically, for a cyclic system with two equations per node, we need to solve 8 coupled algebraic equations to eliminate the quadratic terms for a given mode, and 16 coupled equations to eliminate the cubic terms for a given mode. For n equations per mode these are n^3 and n^4, respectively. For a given mode we can either eliminate the nonlinear terms up to third order or obtain the normal form if the mode undergoes a bifurcation. We emphasize that this method is independent of the number of nodes N in the system.

4.2.3.1 Network-based quadratic near-identity transformation

To eliminate the quadratic terms in (4.23) we use the quadratic near identity transformation

$$\hat{\mathbf{z}} = \big(\hat{\mathbf{I}} + \hat{\mathbf{\Psi}}(\hat{\mathbf{u}})\big)\hat{\mathbf{u}}, \tag{4.32}$$

where $\hat{\mathbf{u}} = \mathrm{col}\,[\mathbf{u}_0 \ \ldots \ \mathbf{u}_k \ \ldots \ \mathbf{u}_{N-1}]$ and $\mathbf{u}_k = [u_k^{(1)}\, u_k^{(2)}]^{\mathrm{T}}$. In $\hat{\mathbf{\Psi}}(\hat{\mathbf{u}})$ the 2×2 block corresponding to the mode numbers $k, \ell = 0, \ldots, N-1$ is given by

$$\mathbf{\Psi}_{k\ell}(\mathbf{u}_{f_{k\ell}}) = \begin{bmatrix} \overline{\psi}_{k\ell}^{(11)} \cdot \mathbf{u}_{f_{k\ell}} & \overline{\psi}_{k\ell}^{(12)} \cdot \mathbf{u}_{f_{k\ell}} \\ \overline{\psi}_{k\ell}^{(21)} \cdot \mathbf{u}_{f_{k\ell}} & \overline{\psi}_{k\ell}^{(22)} \cdot \mathbf{u}_{f_{k\ell}} \end{bmatrix}, \tag{4.33}$$

where $\psi_{k\ell}^{(mn)} = [\psi_{k\ell}^{(mn1)}\ \psi_{k\ell}^{(mn2)}]^{\mathrm{T}}$, the bar denotes complex conjugate, $f_{k\ell}$ is given by (4.27), and the dot stands for the inner product defined as

$$\mathbf{a}\cdot\mathbf{b} = \overline{a}_1 b_1 + \overline{a}_2 b_2\,. \tag{4.34}$$

The matrix $\hat{\mathbf{\Psi}}(\hat{\mathbf{u}})$ has the same structure as the modal matrices in (4.26) that appear in the quadratic terms of (4.23).

In order to derive the coefficients we obtain $\dot{\hat{\mathbf{z}}}$ in two different ways up to second order. On one hand, we substitute (4.32) into the right hand side of (4.23). On the other hand, we take the time derivative of (4.32). Comparing these two approaches and considering

$$\dot{\hat{\mathbf{u}}} = \hat{\mathbf{D}}\hat{\mathbf{u}} + \mathscr{O}(\hat{\mathbf{u}}^3)\,, \tag{4.35}$$

we obtain

$$\Big(\hat{\mathbf{\Psi}}(\hat{\mathbf{D}}\,\hat{\mathbf{u}}) + \hat{\mathbf{\Psi}}(\hat{\mathbf{u}})\,\hat{\mathbf{D}} - \hat{\mathbf{D}}\,\hat{\mathbf{\Psi}}(\hat{\mathbf{u}})\Big)\hat{\mathbf{u}} = \frac{1}{2}\Big(\sum_{b=0,1}\sum_{\beta=1,2} \hat{\mathfrak{L}}^{(\beta)}\big(\hat{\mathbf{S}}_b(\hat{\mathbf{u}})\big)\,\hat{\mathbf{K}}_b^{(\beta)}\Big)\hat{\mathbf{u}}\,, \tag{4.36}$$

where the left hand side contains the coefficients of the transformation matrix, while the right hand side contains the quadratic terms we seek to eliminate via the transformation. The similar structure of the matrices on the two sides of (4.36) allows us to eliminate vector $\hat{\mathbf{u}}$ and comparing the appropriate blocks yields

$$\mathbf{\Psi}_{k\ell}(\mathbf{D}_{f_{k\ell}}\mathbf{u}_{f_{k\ell}}) + \mathbf{\Psi}_{k\ell}(\mathbf{u}_{f_{k\ell}})\mathbf{D}_\ell - \mathbf{D}_k\mathbf{\Psi}_{k\ell}(\mathbf{u}_{f_{k\ell}}) = \frac{1}{2}\sum_{b=0,1}\sum_{\beta=1,2} \mathfrak{L}^{(\beta)}\left(\mathbf{S}_{bk\ell}(\mathbf{u}_{f_{k\ell}})\right)\mathbf{K}_{b\ell}^{(\beta)}. \tag{4.37}$$

For each k,ℓ pair this gives a linear system of 8 equations with 8 unknowns of the form

$$\mathbf{A}_{k\ell}\mathbf{b}_{k\ell} = \mathbf{c}_{k\ell}, \tag{4.38}$$

where the coefficient matrix $\mathbf{A}_{k\ell} \in \mathbb{C}^{8\times 8}$ is composed of 2×2 blocks as

$$\begin{aligned}\mathbf{A}_{k\ell} &= -\mathbf{D}_k \otimes \mathbf{I} \otimes \mathbf{I} + \mathbf{I} \otimes \mathbf{D}_\ell^{\mathrm{T}} \otimes \mathbf{I} + \mathbf{I} \otimes \mathbf{I} \otimes \mathbf{D}_{f_{k\ell}}^{\mathrm{T}} \\ &= \begin{bmatrix} \mathbf{D}_{f_{k\ell}}^{\mathrm{T}} + \xi_{k\ell}^{(11)\,*}\mathbf{I} & \kappa_{\ell 0}^{(21)\,*}\mathbf{I} & -\kappa_{k0}^{(12)\,*}\mathbf{I} & \mathbf{0} \\ \kappa_{\ell 0}^{(12)\,*}\mathbf{I} & \mathbf{D}_{f_{k\ell}}^{\mathrm{T}} + \xi_{k\ell}^{(21)\,*}\mathbf{I} & \mathbf{0} & -\kappa_{k0}^{(12)\,*}\mathbf{I} \\ -\kappa_{k0}^{(21)\,*}\mathbf{I} & \mathbf{0} & \mathbf{D}_{f_{k\ell}}^{\mathrm{T}} + \xi_{k\ell}^{(12)\,*}\mathbf{I} & \kappa_{\ell 0}^{(21)\,*}\mathbf{I} \\ \mathbf{0} & -\kappa_{k0}^{(21)\,*}\mathbf{I} & \kappa_{\ell 0}^{(12)\,*}\mathbf{I} & \mathbf{D}_{f_{k\ell}}^{\mathrm{T}} + \xi_{k\ell}^{(22)\,*}\mathbf{I} \end{bmatrix}. \end{aligned} \tag{4.39}$$

Here we have

$$\kappa_{k\ell}^{(\beta\,\delta)} = \partial_0^{(\delta)} g^{(\beta)} + \partial_1^{(\delta)} g^{(\beta)}\, \mathrm{e}^{\mathrm{i}\frac{2\pi(k-\ell)}{N}}, \tag{4.40}$$

and

$$\xi_{k\ell}^{(\beta\,\delta)\,*} = \kappa_{\ell 0}^{(\beta\,\beta)\,*} - \kappa_{k0}^{(\delta\,\delta)\,*}, \tag{4.41}$$

for $\beta,\ \delta = 1, 2$ where the asterisk indicates that the derivatives are evaluated at the equilibrium. The vector $\mathbf{b}_{k\ell} \in \mathbb{C}^8$ contains the near-identity coefficients defined in (4.33) that appear on the left hand side of (4.37), i.e.,

$$\mathbf{b}_{k\ell} = [\psi_{k\ell}^{(111)}\ \ \psi_{k\ell}^{(112)}\ \ \psi_{k\ell}^{(121)}\ \ \psi_{k\ell}^{(122)}\ \ \psi_{k\ell}^{(211)}\ \ \psi_{k\ell}^{(212)}\ \ \psi_{k\ell}^{(221)}\ \ \psi_{k\ell}^{(222)}]^{\mathrm{T}}, \tag{4.42}$$

while the vector $\mathbf{c}_{k\ell} \in \mathbb{C}^8$ contains the terms that appear on the right hand side of (4.37), that

is,

$$\mathbf{c}_{k\ell} = \frac{1}{2}\begin{bmatrix} \left[\left(\partial_0^{(1)} + \partial_1^{(1)} e^{i\frac{2\pi\ell}{N}}\right)\left(\kappa_{k\ell}^{(11)}\right)\right]^* \\ \left[\left(\partial_0^{(1)} + \partial_1^{(1)} e^{i\frac{2\pi\ell}{N}}\right)\left(\kappa_{k\ell}^{(12)}\right)\right]^* \\ \left[\left(\partial_0^{(2)} + \partial_1^{(2)} e^{i\frac{2\pi\ell}{N}}\right)\left(\kappa_{k\ell}^{(11)}\right)\right]^* \\ \left[\left(\partial_0^{(2)} + \partial_1^{(2)} e^{i\frac{2\pi\ell}{N}}\right)\left(\kappa_{k\ell}^{(12)}\right)\right]^* \\ \left[\left(\partial_0^{(1)} + \partial_1^{(1)} e^{i\frac{2\pi\ell}{N}}\right)\left(\kappa_{k\ell}^{(21)}\right)\right]^* \\ \left[\left(\partial_0^{(1)} + \partial_1^{(1)} e^{i\frac{2\pi\ell}{N}}\right)\left(\kappa_{k\ell}^{(22)}\right)\right]^* \\ \left[\left(\partial_0^{(2)} + \partial_1^{(2)} e^{i\frac{2\pi\ell}{N}}\right)\left(\kappa_{k\ell}^{(21)}\right)\right]^* \\ \left[\left(\partial_0^{(2)} + \partial_1^{(2)} e^{i\frac{2\pi\ell}{N}}\right)\left(\kappa_{k\ell}^{(22)}\right)\right]^* \end{bmatrix}. \tag{4.43}$$

We remark that (4.38) can be solved for each k,ℓ pair separately, that is, when focusing on a chosen mode k we need to solve N decoupled systems of 8 equations. On the other hand, using traditional near-identity transformations would require one to solve $8N^2$ coupled equations. Unless a fold bifurcation (or any other resonance) occurs, we shall be able to select the matrix $\hat{\mathbf{\Psi}}(\hat{\mathbf{u}})$ so that the dynamics of the system do not contain second order terms. Using the new coordinates, (4.35) can be expressed as

$$\begin{aligned} \dot{\hat{\mathbf{u}}} = \hat{\mathbf{D}}\hat{\mathbf{u}} + \frac{1}{2}\sum_{b=0,1}\sum_{\beta=1,2}\Big(\hat{\mathfrak{L}}^{(\beta)}\big(\hat{\mathbf{S}}_b(\hat{\mathbf{\Psi}}(\hat{\mathbf{u}})\hat{\mathbf{u}})\big)\hat{\mathbf{K}}_b^{(\beta)} + \hat{\mathfrak{L}}^{(\beta)}\big(\hat{\mathbf{S}}_b(\hat{\mathbf{u}})\big)\hat{\mathbf{K}}_b^{(\beta)}\hat{\mathbf{\Psi}}(\hat{\mathbf{u}})\Big)\hat{\mathbf{u}} \\ + \frac{1}{6}\sum_{b=0,1}\sum_{\beta=1,2}\sum_{d=0,1}\sum_{\delta=1,2}\hat{\mathfrak{L}}^{(\beta)}\big(\hat{\mathbf{S}}_b(\hat{\mathbf{u}})\big)\hat{\mathfrak{L}}^{(\delta)}\big(\hat{\mathbf{S}}_d(\hat{\mathbf{u}})\big)\hat{\mathbf{L}}_{bd}^{(\beta\,\delta)}\hat{\mathbf{u}}. \end{aligned} \tag{4.44}$$

When comparing (4.23) and (4.44) one may notice that while the second order terms disappear, the transformation generates additional third order terms. The cubic terms in the bottom row of (4.44) originate from the cubic terms present in the modal system (4.23) while the cubic terms in the top row appear due to the quadratic near-identity transformation. It is shown in Appendix C that the two terms appearing in the top row are equal, which

yields

$$\begin{aligned}\dot{\hat{\mathbf{u}}} = \hat{\mathbf{D}}\hat{\mathbf{u}} + \sum_{b=0,1}\sum_{\beta=1,2}\hat{\mathfrak{L}}^{(\beta)}\big(\hat{\mathbf{S}}_b(\hat{\mathbf{u}})\big)\hat{\mathbf{K}}_b^{(\beta)}\hat{\mathbf{\Psi}}(\hat{\mathbf{u}})\hat{\mathbf{u}} \\ + \frac{1}{6}\sum_{b=0,1}\sum_{\beta=1,2}\sum_{d=0,1}\sum_{\delta=1,2}\hat{\mathfrak{L}}^{(\beta)}\big(\hat{\mathbf{S}}_b(\hat{\mathbf{u}})\big)\hat{\mathfrak{L}}^{(\delta)}\big(\hat{\mathbf{S}}_d(\hat{\mathbf{u}})\big)\hat{\mathbf{L}}_{bd}^{(\beta\,\delta)}\hat{\mathbf{u}}.\end{aligned} \tag{4.45}$$

4.2.3.2 Network-based cubic near-identity transformation

Based on the structure of the cubic terms in (4.45), we define the cubic near-identity transformation

$$\hat{\mathbf{u}} = \big(\hat{\mathbf{I}} + \hat{\mathbf{\Gamma}}(\hat{\mathbf{w}})\,\hat{\mathbf{\Phi}}(\hat{\mathbf{w}})\big)\hat{\mathbf{w}}, \tag{4.46}$$

where $\hat{\mathbf{w}} = \mathrm{col}\,[\mathbf{w}_0\ \ldots\ \mathbf{w}_k\ \ldots\ \mathbf{w}_{N-1}]$ and $\mathbf{w}_k = [w_k^{(1)}\ w_k^{(2)}]^{\mathrm{T}}$. The matrices $\hat{\mathbf{\Gamma}}(\hat{\mathbf{w}})$ and $\hat{\mathbf{\Phi}}(\hat{\mathbf{w}})$ have a circulant block structure, where the blocks for mode numbers $k, \ell = 0, \ldots, N-1$ are given by

$$\mathbf{\Gamma}_{k\ell}(\mathbf{w}_{f_{k,\ell}}) = \begin{bmatrix}\overline{\gamma}_{k\ell}^{(11)}\cdot\mathbf{w}_{f_{k\ell}} & \overline{\gamma}_{k\ell}^{(12)}\cdot\mathbf{w}_{f_{k\ell}} \\ \overline{\gamma}_{k\ell}^{(21)}\cdot\mathbf{w}_{f_{k\ell}} & \overline{\gamma}_{k\ell}^{(22)}\cdot\mathbf{w}_{f_{k\ell}}\end{bmatrix}, \quad \mathbf{\Phi}_{k\ell}(\mathbf{w}_{f_{k\ell}}) = \begin{bmatrix}\overline{\phi}_{k\ell}^{(11)}\cdot\mathbf{w}_{f_{k\ell}} & \overline{\phi}_{k\ell}^{(12)}\cdot\mathbf{w}_{f_{k\ell}} \\ \overline{\phi}_{k\ell}^{(21)}\cdot\mathbf{w}_{f_{k\ell}} & \overline{\phi}_{k\ell}^{(22)}\cdot\mathbf{w}_{f_{k\ell}}\end{bmatrix}, \tag{4.47}$$

where $\gamma_{k\ell}^{(mn)} = [\gamma_{k\ell}^{(mn1)}\ \gamma_{k\ell}^{(mn2)}]^{\mathrm{T}}$ and $\phi_{k\ell}^{(mn)} = [\phi_{k\ell}^{(mn1)}\ \phi_{k\ell}^{(mn2)}]^{\mathrm{T}}$, $f_{k\ell}$ is given by (4.27), and the inner product is defined by (4.34).

Again, we may obtain $\dot{\hat{\mathbf{u}}}$ in two ways. On one hand, we may substitute (4.46) into (4.45), while on the other hand, we may differentiate (4.46) with respect to time. Considering

$$\dot{\hat{\mathbf{w}}} = \hat{\mathbf{D}}\,\hat{\mathbf{w}} + \mathscr{O}(\hat{\mathbf{w}}^4), \tag{4.48}$$

we obtain

$$\begin{aligned}&\Big(\hat{\mathbf{\Gamma}}(\hat{\mathbf{D}}\hat{\mathbf{w}})\,\hat{\mathbf{\Phi}}(\hat{\mathbf{w}}) + \hat{\mathbf{\Gamma}}(\hat{\mathbf{w}})\,\hat{\mathbf{\Phi}}(\hat{\mathbf{D}}\hat{\mathbf{w}}) + \hat{\mathbf{\Gamma}}(\hat{\mathbf{w}})\,\hat{\mathbf{\Phi}}(\hat{\mathbf{w}})\hat{\mathbf{D}} - \hat{\mathbf{D}}\hat{\mathbf{\Gamma}}(\hat{\mathbf{w}})\hat{\mathbf{\Phi}}(\hat{\mathbf{w}})\Big)\hat{\mathbf{w}} \\ &= \Big(\sum_{b=0,1}\sum_{\beta=1,2}\hat{\mathfrak{L}}^{(\beta)}\big(\hat{\mathbf{S}}_b(\hat{\mathbf{w}})\big)\hat{\mathbf{K}}_b^{(\beta)}\hat{\mathbf{\Psi}}(\hat{\mathbf{w}}) + \frac{1}{6}\sum_{b=0,1}\sum_{\beta=1,2}\sum_{d=0,1}\sum_{\delta=1,2}\hat{\mathfrak{L}}^{(\beta)}\big(\hat{\mathbf{S}}_b(\hat{\mathbf{w}})\big)\hat{\mathfrak{L}}^{(\delta)}\big(\hat{\mathbf{S}}_d(\hat{\mathbf{w}})\big)\hat{\mathbf{L}}_{bd}^{(\beta\,\delta)}\Big)\hat{\mathbf{w}}.\end{aligned} \tag{4.49}$$

where the left hand side contains the coefficients of the transformation matrices, while the right hand side contains the cubic terms we seek to eliminate via the transformation. Again, exploiting the similarity of structure of the matrices on the two sides of (4.49) we

can eliminate $\hat{\mathbf{w}}$ and compare the appropriate blocks to get

$$\begin{aligned}
&\sum_{j=0}^{N-1}\Big(\boldsymbol{\Gamma}_{kj}(\mathbf{D}_{f_{kj}}\mathbf{w}_{f_{kj}})\boldsymbol{\Phi}_{j\ell}(\mathbf{w}_{f_{j\ell}}) \\
&+\boldsymbol{\Gamma}_{kj}(\mathbf{w}_{f_{kj}})\boldsymbol{\Phi}_{j\ell}(\mathbf{D}_{f_{j\ell}}\mathbf{w}_{f_{j\ell}})+\boldsymbol{\Gamma}_{kj}(\mathbf{w}_{f_{kj}})\boldsymbol{\Phi}_{j\ell}(\mathbf{w}_{f_{j\ell}})\mathbf{D}_{\ell}-\mathbf{D}_{k}\boldsymbol{\Gamma}_{kj}(\mathbf{w}_{f_{kj}})\boldsymbol{\Phi}_{j\ell}(\mathbf{w}_{f_{j\ell}})\Big) \\
&=\sum_{j=0}^{N-1}\Bigg(\sum_{b=0,1}\sum_{\beta=1,2}\mathfrak{L}^{(\beta)}\big(\mathbf{S}_{bkj}(\mathbf{w}_{f_{kj}})\big)\mathbf{K}_{bj}^{(\beta)}\boldsymbol{\Psi}_{j\ell}(\mathbf{w}_{f_{j\ell}}) \\
&+\frac{1}{6}\sum_{b=0,1}\sum_{\beta=1,2}\sum_{d=0,1}\sum_{\delta=1,2}\mathfrak{L}^{(\beta)}\big(\mathbf{S}_{bkj}(\mathbf{w}_{f_{kj}})\big)\,\mathfrak{L}^{(\delta)}\big(\mathbf{S}_{dj\ell}(\mathbf{w}_{f_{j\ell}})\big)\,\mathbf{L}_{bd\ell}^{(\beta\delta)}\Bigg),
\end{aligned} \tag{4.50}$$

where the sum over j appears due to the multiplication of circulant matrices.

Each triplet k, j, ℓ yields 16 equations for the products of coefficients $\gamma_{kj}\phi_{j\ell}$, (cf. (4.47)), and 32 different products exist. However we can combine certain pairs of products (that always occur together) and obtain a set of 16 equations with 16 unknowns for each k, j, ℓ triplet:

$$\tilde{\mathbf{A}}_{kj\ell}\tilde{\mathbf{b}}_{kj\ell}=\tilde{\mathbf{c}}_{kj\ell}. \tag{4.51}$$

The matrix $\tilde{\mathbf{A}}_{kj\ell}\in\mathbb{C}^{16\times 16}$ is composed of four 8×8 blocks such that

$$\begin{aligned}
\tilde{\mathbf{A}}_{kj\ell}&=-\mathbf{D}_{k}\otimes\mathbf{I}\otimes\mathbf{I}\otimes\mathbf{I}+\mathbf{I}\otimes\mathbf{D}_{\ell}^{\mathrm{T}}\otimes\mathbf{I}\otimes\mathbf{I}+\mathbf{I}\otimes\mathbf{I}\otimes\mathbf{D}_{f_{kj}}^{\mathrm{T}}\otimes\mathbf{I}+\mathbf{I}\otimes\mathbf{I}\otimes\mathbf{I}\otimes\mathbf{D}_{f_{j\ell}}^{\mathrm{T}} \\
&=\begin{bmatrix}\mathbf{E}_{kj\ell} & \mathbf{F}_{kj\ell}\\ \mathbf{G}_{kj\ell} & \mathbf{H}_{kj\ell}\end{bmatrix},
\end{aligned} \tag{4.52}$$

where

$$\mathbf{E}_{kj\ell} = \begin{bmatrix} \mathbf{D}_{f_{j\ell}}^{\mathrm{T}} + \xi_{kj\ell}^{(111)*}\mathbf{I} & \kappa_{kj}^{(21)*}\mathbf{I} & \kappa_{\ell 0}^{(21)*}\mathbf{I} & \mathbf{0} \\ \kappa_{kj}^{(12)*}\mathbf{I} & \mathbf{D}_{f_{j\ell}}^{\mathrm{T}} + \xi_{kj\ell}^{(211)*}\mathbf{I} & \mathbf{0} & \kappa_{\ell 0}^{(21)*}\mathbf{I} \\ \kappa_{\ell 0}^{(12)*}\mathbf{I} & \mathbf{0} & \mathbf{D}_{f_{j\ell}}^{\mathrm{T}} + \xi_{kj\ell}^{(121)*}\mathbf{I} & \kappa_{kj}^{(21)*}\mathbf{I} \\ \mathbf{0} & \kappa_{\ell 0}^{(12)*}\mathbf{I} & \kappa_{kj}^{(12)*}\mathbf{I} & \mathbf{D}_{f_{j\ell}}^{\mathrm{T}} + \xi_{kj\ell}^{(221)*}\mathbf{I} \end{bmatrix},$$

$$\mathbf{F}_{kj\ell} = -\kappa_{k0}^{(12)*}\begin{bmatrix} 1 & 0 & 0 & 0 \\ 0 & 1 & 0 & 0 \\ 0 & 0 & 1 & 0 \\ 0 & 0 & 0 & 1 \end{bmatrix} \otimes \mathbf{I}, \qquad \mathbf{G}_{kj\ell} = -\kappa_{k0}^{(21)*}\begin{bmatrix} 1 & 0 & 0 & 0 \\ 0 & 1 & 0 & 0 \\ 0 & 0 & 1 & 0 \\ 0 & 0 & 0 & 1 \end{bmatrix} \otimes \mathbf{I},$$

$$\mathbf{H}_{kj\ell} = \begin{bmatrix} \mathbf{D}_{f_{j\ell}}^{\mathrm{T}} + \xi_{kj\ell}^{(112)*}\mathbf{I} & \kappa_{kj}^{(21)*}\mathbf{I} & \kappa_{\ell 0}^{(21)*}\mathbf{I} & \mathbf{0} \\ \kappa_{kj}^{(12)*}\mathbf{I} & \mathbf{D}_{f_{j\ell}}^{\mathrm{T}} + \xi_{kj\ell}^{(212)*}\mathbf{I} & \mathbf{0} & \kappa_{\ell 0}^{(21)*}\mathbf{I} \\ \kappa_{\ell 0}^{(12)*}\mathbf{I} & \mathbf{0} & \mathbf{D}_{f_{j\ell}}^{\mathrm{T}} + \xi_{kj\ell}^{(122)*}\mathbf{I} & \kappa_{kj}^{(21)*}\mathbf{I} \\ \mathbf{0} & \kappa_{\ell 0}^{(12)*}\mathbf{I} & \kappa_{kj}^{(12)*}\mathbf{I} & \mathbf{D}_{f_{j\ell}}^{\mathrm{T}} + \xi_{kj\ell}^{(222)*}\mathbf{I} \end{bmatrix}. \tag{4.53}$$

Here we have

$$\xi_{kj\ell}^{(\beta\delta\theta)*} = \kappa_{kj}^{(\beta\beta)*} + \kappa_{\ell 0}^{(\delta\delta)*} - \kappa_{k0}^{(\theta\theta)*}, \tag{4.54}$$

for $\beta, \delta, \theta = 1, 2$ and $\kappa_{k\ell}^{(\beta\delta)}$ is defined in (4.40). The vector $\tilde{\mathbf{b}}_{kj\ell}$ contains the coefficients defined in (4.47) that appear on the left hand side of (4.50) (see Appendix D), while vector $\tilde{\mathbf{c}}_{kj\ell}$ contains the cubic coefficients that appear on the right hand side of (4.50) (see Appendix E). Similarly to the quadratic case, (4.51) can be solved for each k, j, ℓ triplet separately, that is, for a chosen k one need to solve N^2 decoupled systems of 16 equations. Again, using traditional nonlinear near identity transformations would lead to $16N^3$ coupled equations. If there are no bifurcations or resonant third order terms, (4.51) can be solved for all triplets k, j, ℓ and all cubic coefficients can be eliminated yielding the form (4.48).

When bifurcations or resonances occur certain terms cannot be eliminated. However, the set of nonlinear transformations described above allows us to decouple the mode responsible for the bifurcation from the rest of the system. By performing one more linear transformation on this small system the normal form of the bifurcation can be derived.

4.3 Network-based analysis of the connected vehicle system

First, we decompose the connected vehicle network into modes at the linear level and analyze the linear stability of the modes. Then we use nonlinear network-based analysis to eliminate the nonlinearities for the modes responsible for the stability loss. Finally, we investigate the criticality of bifurcations and determine the amplitude of nonlinear oscillations associated with the modal stability loss using normal forms.

To take advantage of the cyclic symmetry, in this chapter we consider (4.1) to govern the dynamics of all the vehicles in the CVN. Thus we consider the third order approximation (4.3) with $\beta_1 = \beta$ and $\beta_{i\sigma} = 0$. Using the vector notation $\mathbf{y}_i = [\widetilde{s}_i \;\; \widetilde{v}_i]^{\mathrm{T}}$ we can rewrite this approximation into the compact form

$$\begin{aligned}\dot{\mathbf{y}}_i = {} & [\mathfrak{J}_0]^*\mathbf{y}_i + [\mathfrak{J}_1]^*\mathbf{y}_{i+1} + \frac{1}{2}\sum_{b=0,1}\mathbf{H}_b^{(1)}(\mathbf{y}_{i+b})\left([\partial_b^{(1)}\mathfrak{J}_0]^*\mathbf{y}_i + [\partial_b^{(1)}\mathfrak{J}_1]^*\mathbf{y}_{i+1}\right) \\ & + \frac{1}{6}\sum_{b=0,1}\sum_{d=0,1}\mathbf{H}_b^{(1)}(\mathbf{y}_{i+b})\,\mathbf{H}_d^{(1)}(\mathbf{y}_{i+d})\left([\partial_b^{(1)}\partial_d^{(1)}\mathfrak{J}_0]^*\mathbf{y}_i + [\partial_b^{(1)}\partial_d^{(1)}\mathfrak{J}_1]^*\mathbf{y}_{i+1}\right).\end{aligned} \tag{4.55}$$

cf. (4.8). Notice that since only the position coordinates $\widetilde{s}_i$ appear in the nonlinear terms, we do not have to sum for the individual coordinates of $\mathbf{y}_i$. The linear terms in (4.55) contain the matrices

$$[\mathfrak{J}_0]^* = \begin{bmatrix} 0 & 1 \\ -p & -(\alpha+\beta) \end{bmatrix}, \qquad [\mathfrak{J}_1]^* = \begin{bmatrix} 0 & 0 \\ p & \beta \end{bmatrix}, \tag{4.56}$$

while the coefficient matrices in the quadratic terms are given by

$$[\partial_0^{(1)}\mathfrak{J}_0]^* = -[\partial_0^{(1)}\mathfrak{J}_1]^* = -[\partial_1^{(1)}\mathfrak{J}_0]^* = [\partial_1^{(1)}\mathfrak{J}_1]^* = \begin{bmatrix} 0 & 0 \\ q & 0 \end{bmatrix}, \tag{4.57}$$

and the cubic terms contain

$$\begin{aligned} -[\partial_0^{(1)}\partial_0^{(1)}\mathfrak{J}_0]^* = -[\partial_0^{(1)}\partial_1^{(1)}\mathfrak{J}_1]^* = -[\partial_1^{(1)}\partial_1^{(1)}\mathfrak{J}_0]^* = \begin{bmatrix} 0 & 0 \\ r & 0 \end{bmatrix}, \\ [\partial_0^{(1)}\partial_0^{(1)}\mathfrak{J}_1]^* = [\partial_0^{(1)}\partial_1^{(1)}\mathfrak{J}_0]^* = [\partial_1^{(1)}\partial_1^{(1)}\mathfrak{J}_1]^* = \begin{bmatrix} 0 & 0 \\ r & 0 \end{bmatrix}, \end{aligned} \tag{4.58}$$

where p, q, r are given by (4.4). For the whole system, (4.55) can be reformulated as

$$\dot{\hat{\mathbf{y}}} = \left(\mathbf{I}_N \otimes [\mathfrak{J}_0]^* + \mathbf{A}_N \otimes [\mathfrak{J}_1]^*\right)\hat{\mathbf{y}} + \frac{1}{2}\sum_{b=0,1} \hat{\mathfrak{L}}^{(1)}\big(\hat{\mathbf{H}}_b(\hat{\mathbf{y}})\big)\left(\mathbf{I}_N \otimes [\partial_b^{(1)}\mathfrak{J}_0]^* + \mathbf{A}_N \otimes \big[\partial_b^{(1)}\mathfrak{J}_1\big]^*\right)\hat{\mathbf{y}}$$
$$+ \frac{1}{6}\sum_{b=0,1}\sum_{d=0,1} \hat{\mathfrak{L}}^{(1)}\big(\hat{\mathbf{H}}_b(\hat{\mathbf{y}})\big)\,\hat{\mathfrak{L}}^{(1)}\big(\hat{\mathbf{H}}_d(\hat{\mathbf{y}})\big)\left(\mathbf{I}_N \otimes [\partial_b^{(1)}\partial_d^{(1)}\mathfrak{J}_0]^* + \mathbf{A}_N \otimes [\partial_b^{(1)}\partial_d^{(1)}\mathfrak{J}_1]^*\right)\hat{\mathbf{y}}, \tag{4.59}$$

cf. (4.12). The linear coordinate transformation (4.22) yields

$$\dot{\hat{\mathbf{z}}} = \hat{\mathbf{D}}\,\hat{\mathbf{z}} + \frac{1}{2}\sum_{b=0,1} \hat{\mathfrak{L}}^{(1)}\big(\hat{\mathbf{S}}_b(\hat{\mathbf{z}})\big)\,\hat{\mathbf{K}}_b^{(1)}\,\hat{\mathbf{z}} + \frac{1}{6}\sum_{b=0,1}\sum_{d=0,1} \hat{\mathfrak{L}}^{(1)}\big(\hat{\mathbf{S}}_b(\hat{\mathbf{z}})\big)\,\hat{\mathfrak{L}}^{(1)}\big(\hat{\mathbf{S}}_d(\hat{\mathbf{z}})\big)\hat{\mathbf{L}}_{bd}^{(11)}\hat{\mathbf{z}}, \tag{4.60}$$

cf. (4.23), where $\hat{\mathbf{D}}$, $\hat{\mathbf{S}}_b(\hat{\mathbf{z}})$, $\hat{\mathbf{K}}_b^{(1)}$, $\hat{\mathbf{L}}_{bd}^{(11)} \in \mathbb{C}^{2N\times 2N}$ are given by (4.24, 4.26, 4.28, 4.30).

4.3.1 Linear Stability Analysis

The linear part of (4.60) consists of N decoupled complex differential equations which represent the linear modes in the system. For the k-th mode the linear dynamics are given by

$$\begin{bmatrix} \dot{z}_k^{(1)} \\ \dot{z}_k^{(2)} \end{bmatrix} = \begin{bmatrix} 0 & 1 \\ p\,\eta_{k0} & \beta\,\eta_{k0} - \alpha \end{bmatrix} \begin{bmatrix} z_k^{(1)} \\ z_k^{(2)} \end{bmatrix}, \tag{4.61}$$

where

$$\eta_{k\ell} = \mathrm{e}^{\mathrm{i}\frac{2\pi(k-\ell)}{N}} - 1\,, \tag{4.62}$$

for $k, \ell = 0, \ldots, N-1$. Thus, using the trial solution $z_k^{(1)}(t) = z_{k\,0}^{(1)}\mathrm{e}^{\lambda t}$, $z_k^{(2)}(t) = z_{k\,0}^{(2)}\mathrm{e}^{\lambda t}$ with $\lambda, z_{k\,0}^{(1)}, z_{k\,0}^{(2)} \in \mathbb{C}$ the characteristic equation for mode k becomes

$$\lambda^2 + (\alpha+\beta)\,\lambda + p - (\beta\,\lambda + p)\,\mathrm{e}^{\mathrm{i}\frac{2\pi k}{N}} = 0\,. \tag{4.63}$$

If both solutions λ have negative real parts the mode is stable. We remark that when the solutions are complex, they are not complex conjugates, since (4.61) contains complex coefficients. In fact, mode $N-k$ provides the complex conjugate eigenvalues for mode k. The special mode $k = 0$ gives the eigenvalues $\lambda_{0,1} = 0$ and $\lambda_{0,2} = -\alpha$. The former one corresponds to a translational symmetry of the cyclically symmetric network of conventional vehicles (4.1) (see [65]), while the latter one stays in the left-half complex plane for $\alpha > 0$. We note that for even N, there is another special mode $k = N/2$ which does not

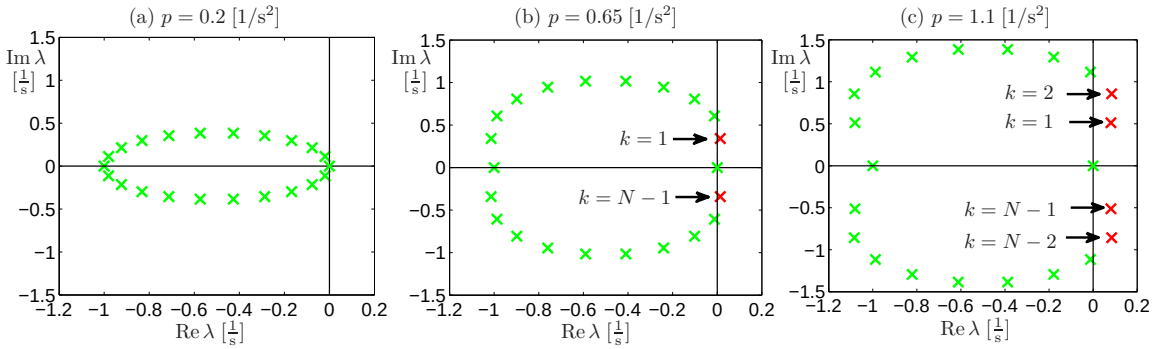

Figure 4.1: Eigenvalues in the complex plane for the human-driven vehicle network (4.1) when considering N=11 cars and parameters $\alpha = 1$ [1/s], $\beta = 0$ [1/s] and varying the parameter $p = \alpha V'(h^*)$. Stable eigenvalues are shown as green crosses, while unstable eigenvalues are depicted as red crosses. The mode numbers for unstable eigenvalues are indicated in cases (b) and (c)

have a complex conjugate mode. The eigenvalues of this mode have negative real parts for $\alpha + 2\beta > 0$.

The critical value of $p = \alpha V'(h^*)$, where modes k and $N-k$ lose stability, can be obtained by substituting $\lambda = i\omega$ into (4.63), taking the real and imaginary parts, and performing some algebraic manipulation to eliminate ω. This yields

$$p_k = \tfrac{1}{2}(2\beta+\alpha)\left((2\beta+\alpha)\tan^2\left(\tfrac{k\pi}{N}\right)+\alpha\right). \tag{4.64}$$

On the other hand, eliminating p we may obtain the critical angular frequency

$$\omega_k = (2\beta+\alpha)\tan\left(\tfrac{k\pi}{N}\right), \tag{4.65}$$

for $k = 1, \ldots, N-1$.

Fig. 5.2 shows how the eigenvalues vary with parameter p for $N = 11$ cars and parameters $\alpha = 1$ [1/s], $\beta = 0$ [1/s]. When p is increased the eigenvalues move in the complex plane and cross the imaginary axis at p_k with imaginary part ω_k. Here we restrict our discussion to $k = 1, \ldots, \lfloor \frac{N}{2} \rfloor$, because for $k = \lceil \frac{N}{2} \rceil, \ldots, N-1$ we get $p_k = p_{N-k}$, $\omega_k = -\omega_{N-k}$ due to the complex conjugacy of modes k and $N-k$. Since (4.64) is monotonically increasing with k when $1 \leq k \leq \lfloor \frac{N}{2} \rfloor$, the modes lose stability in the increasing order of mode number k. Thus, the uniform flow loses stability when modes 1 (and $N-1$) lose stability. Since the eigenvalues cross the imaginary axis with a non-zero imaginary part and with finite speed (i.e., $\omega_k > 0$, $\mathrm{Re}\frac{\partial \lambda}{\partial p}(p_k) > 0$), Hopf bifurcations occur in the corresponding nonlinear system. This leads to nonlinear oscillations with frequency close to (4.65) and wavelength

$(L+N\ell)/k$; see [67]. The corresponding periodic orbit is embedded in the modal subspace given by modes k and $N-k$. At the linear level, the oscillations can be characterized by the modal coordinates $\mathbf{z}_k$ and $\mathbf{z}_{N-k}$ (see (4.61)), while at the nonlinear level further nonlinear transformations are needed to describe the oscillations.

4.3.2 Near-identity transformations

Let us use the network-based nonlinear transformations to eliminate nonlinear terms in (4.60) at the Hopf point corresponding to the stability loss (i.e., $p = p_1$). This way we can obtain a nonlinear modal equations for modes 1 and $N-1$ that are decoupled from the rest of the system. To eliminate the quadratic terms in (4.60) we use the near-identity transformation (4.32). In this case (4.36) simplifies to

$$\Big(\hat{\boldsymbol{\Psi}}(\hat{\mathbf{D}}\hat{\mathbf{u}}) + \hat{\boldsymbol{\Psi}}(\hat{\mathbf{u}})\hat{\mathbf{D}} - \hat{\mathbf{D}}\hat{\boldsymbol{\Psi}}(\hat{\mathbf{u}})\Big)\hat{\mathbf{u}} = \frac{1}{2}\Big(\sum_{b=0,1} \hat{\mathfrak{L}}^{(1)}\big(\hat{\mathbf{S}}_b(\hat{\mathbf{u}})\big)\,\hat{\mathbf{K}}_b^{(1)}\Big)\hat{\mathbf{u}}, \tag{4.66}$$

which is equivalent to

$$\boldsymbol{\Psi}_{k\ell}(\mathbf{D}_{f_{k\ell}}\mathbf{u}_{f_{k\ell}}) + \boldsymbol{\Psi}_{k\ell}(\mathbf{u}_{f_{k\ell}})\mathbf{D}_\ell - \mathbf{D}_k\boldsymbol{\Psi}_{k\ell}(\mathbf{u}_{f_{k\ell}}) = \frac{1}{2}\sum_{b=0,1} \mathfrak{L}^{(1)}\big(\mathbf{S}_{bk\ell}(\mathbf{u}_{f_{k\ell}})\big)\mathbf{K}_{b\ell}^{(1)}, \tag{4.67}$$

cf. (4.37). Thus, in (4.38) we have

$$\mathbf{A}_{k\ell} = \begin{bmatrix} \mathbf{D}_{f_{k\ell}}^{\mathrm{T}} & \kappa_{\ell 0}^{(21)\,*}\mathbf{I} & -\mathbf{I} & \mathbf{0} \\ \mathbf{I} & \mathbf{D}_{f_{k\ell}}^{\mathrm{T}} + \kappa_{\ell 0}^{(22)\,*}\mathbf{I} & \mathbf{0} & -\mathbf{I} \\ -\kappa_{k0}^{(21)\,*}\mathbf{I} & \mathbf{0} & \mathbf{D}_{f_{k\ell}}^{\mathrm{T}} - \kappa_{k0}^{(22)\,*}\mathbf{I} & \kappa_{\ell 0}^{(21)\,*}\mathbf{I} \\ \mathbf{0} & -\kappa_{k0}^{(21)\,*}\mathbf{I} & \mathbf{I} & \mathbf{D}_{f_{k\ell}}^{\mathrm{T}} + (\kappa_{\ell 0}^{(22)\,*} - \kappa_{k0}^{(22)\,*})\mathbf{I} \end{bmatrix}, \tag{4.68}$$

where

$$\kappa_{k\ell}^{(21)\,*} = p_1\,\eta_{k\ell}, \qquad \kappa_{k\ell}^{(22)\,*} = \beta\,\eta_{k\ell} - \alpha, \tag{4.69}$$

and $\eta_{k\ell}$ is defined in (4.62). Note that unlike in (4.39) here we refrain from using $\xi_{k\ell}^{(\beta\,\delta)\,*}$ defined in (4.41) because $\kappa_{k\ell}^{(11)\,*} = 0$ for all k, ℓ. Moreover, the right hand side (4.43) simplifies to

$$\mathbf{c}_{k\ell} = \mathrm{col}[0\ \ 0\ \ 0\ \ 0\ \ \frac{q_1}{2}\,\eta_{k\ell}\,\eta_{\ell 0}\ \ 0\ \ 0\ \ 0]^{\mathrm{T}}, \tag{4.70}$$

where q_1 indicates the value of q at the bifurcation point; cf. (4.4).

Solving (4.38) allows us to eliminate all but a few quadratic terms in the $k = 0$ mode in (4.60). However, as explained above, the $k = 0$ mode does not lose stability and it does not

influence the dynamics of the other modes. The equation in the new coordinates becomes

$$\dot{\hat{\mathbf{u}}} = \hat{\mathbf{D}}\hat{\mathbf{u}} + \frac{1}{2}\hat{\mathbf{R}}(\hat{\mathbf{u}})\hat{\mathbf{u}} + \sum_{b=0,1} \hat{\mathfrak{L}}^{(1)}\big(\hat{\mathbf{S}}_b(\hat{\mathbf{u}})\big)\hat{\mathbf{K}}_b^{(1)}\hat{\mathbf{\Psi}}(\hat{\mathbf{u}})\hat{\mathbf{u}} + \frac{1}{6}\sum_{b=0,1}\sum_{d=0,1} \hat{\mathfrak{L}}^{(1)}\big(\hat{\mathbf{S}}_b(\hat{\mathbf{u}})\big)\hat{\mathfrak{L}}^{(1)}\big(\hat{\mathbf{S}}_d(\hat{\mathbf{u}})\big)\hat{\mathbf{L}}_{bd}^{(11)}\hat{\mathbf{u}}, \tag{4.71}$$

cf. (4.45), where the quadratic terms $\hat{\mathbf{R}}(\hat{\mathbf{u}})\hat{\mathbf{u}}$ appear in the $k = 0$ mode, see Appendix F.

As our goal is to obtain the nonlinear modal equations for modes 1 and $N-1$, we proceed by simplifying the cubic terms using the transformation (4.46) which leads to a simplified form of (4.49):

$$\begin{aligned}
&\Big(\hat{\mathbf{\Gamma}}(\hat{\mathbf{D}}\hat{\mathbf{w}})\,\hat{\mathbf{\Phi}}(\hat{\mathbf{w}}) + \hat{\mathbf{\Gamma}}(\hat{\mathbf{w}})\,\hat{\mathbf{\Phi}}(\hat{\mathbf{D}}\hat{\mathbf{w}}) + \hat{\mathbf{\Gamma}}(\hat{\mathbf{w}})\,\hat{\mathbf{\Phi}}(\hat{\mathbf{w}})\hat{\mathbf{D}} - \hat{\mathbf{D}}\hat{\mathbf{\Gamma}}(\hat{\mathbf{w}})\hat{\mathbf{\Phi}}(\hat{\mathbf{w}})\Big)\hat{\mathbf{w}} \\
&= \Big(\sum_{b=0,1} \hat{\mathfrak{L}}^{(1)}\big(\hat{\mathbf{S}}_b(\hat{\mathbf{w}})\big)\hat{\mathbf{K}}_b^{(1)}\hat{\mathbf{\Psi}}(\hat{\mathbf{w}}) + \frac{1}{6}\sum_{b=0,1}\sum_{d=0,1} \hat{\mathfrak{L}}^{(1)}\big(\hat{\mathbf{S}}_b(\hat{\mathbf{w}})\big)\hat{\mathfrak{L}}^{(1)}\big(\hat{\mathbf{S}}_d(\hat{\mathbf{w}})\big)\hat{\mathbf{L}}_{bd}^{(11)}\Big)\hat{\mathbf{w}},
\end{aligned} \tag{4.72}$$

that is equivalent to

$$\begin{aligned}
&\sum_{j=0}^{N-1}\Big(\mathbf{\Gamma}_{kj}(\mathbf{D}_{f_{kj}}\mathbf{w}_{f_{kj}})\mathbf{\Phi}_{j\ell}(\mathbf{w}_{f_{j\ell}}) + \mathbf{\Gamma}_{kj}(\mathbf{w}_{f_{kj}})\mathbf{\Phi}_{j\ell}(\mathbf{D}_{f_{j\ell}}\mathbf{w}_{f_{j\ell}}) + \mathbf{\Gamma}_{kj}(\mathbf{w}_{f_{kj}})\mathbf{\Phi}_{j\ell}(\mathbf{w}_{f_{j\ell}})\mathbf{D}_\ell - \mathbf{D}_k\mathbf{\Gamma}_{kj}(\mathbf{w}_{f_{kj}})\mathbf{\Phi}_{j\ell}(\mathbf{w}_{f_{j\ell}})\Big) \\
&= \sum_{j=0}^{N-1}\Big(\sum_{b=0,1} \mathfrak{L}^{(1)}\big(\mathbf{S}_{bkj}(\mathbf{w}_{f_{kj}})\big)\mathbf{K}_{bj}^{(1)}\,\mathbf{\Psi}_{j\ell}(\mathbf{w}_{f_{j\ell}}) + \frac{1}{6}\sum_{b=0,1}\sum_{d=0,1} \mathfrak{L}^{(1)}\big(\mathbf{S}_{bkj}(\mathbf{w}_{f_{kj}})\big)\,\mathfrak{L}^{(1)}\big(\mathbf{S}_{dj\ell}(\mathbf{w}_{f_{j\ell}})\big)\,\mathbf{L}_{bd\ell}^{(11)}\Big),
\end{aligned} \tag{4.73}$$

cf. (4.50). The matrix $\widetilde{\mathbf{A}}_{kj\ell}$ in (4.51) has sub-matrices

$$\begin{aligned}
\mathbf{E}_{kj\ell} &= \begin{bmatrix}
\mathbf{D}_{f_{j\ell}}^{\mathrm{T}} & \kappa_{kj}^{(21)\,*}\mathbf{I} & \kappa_{\ell 0}^{(21)\,*}\mathbf{I} & \mathbf{0} \\
\mathbf{I} & \mathbf{D}_{f_{j\ell}}^{\mathrm{T}} + \kappa_{kj}^{(22)\,*}\mathbf{I} & \mathbf{0} & \kappa_{\ell 0}^{(21)\,*}\mathbf{I} \\
\mathbf{I} & \mathbf{0} & \mathbf{D}_{f_{j\ell}}^{\mathrm{T}} + \kappa_{\ell 0}^{(22)\,*}\mathbf{I} & \kappa_{kj}^{(21)\,*}\mathbf{I} \\
\mathbf{0} & \mathbf{I} & \mathbf{I} & \mathbf{D}_{f_{j\ell}}^{\mathrm{T}} + (\kappa_{kj}^{(22)\,*} + \kappa_{\ell 0}^{(22)\,*})\mathbf{I}
\end{bmatrix}, \\
\mathbf{F}_{kj\ell} &= \begin{bmatrix} -1 & 0 & 0 & 0 \\ 0 & -1 & 0 & 0 \\ 0 & 0 & -1 & 0 \\ 0 & 0 & 0 & -1 \end{bmatrix} \otimes \mathbf{I}, \qquad \mathbf{G}_{kj\ell} = \kappa_{k0}^{(21)\,*}\mathbf{F}_{kj\ell}, \qquad \mathbf{H}_{kj\ell} = \mathbf{E}_{kj\ell} - \kappa_{k0}^{(22)\,*}\mathbf{I},
\end{aligned} \tag{4.74}$$

cf. (4.53), where the $\kappa_{k\ell}^{(21)\,*}$ and $\kappa_{k\ell}^{(22)\,*}$ are given by (4.69). Finally the right hand side (E.1)

(in Appendix E) simplifies to

$$\begin{aligned}\tilde{\mathbf{c}}_{kj\ell} &= q_1\,\eta_{kj}\,\eta_{j0}\,[0\ 0\ 0\ 0\ 0\ 0\ 0\ 0\ \psi_{j\ell}^{(111)}\ \ \psi_{j\ell}^{(112)}\ \ 0\ 0\ \ \psi_{j\ell}^{(121)}\ \ \psi_{j\ell}^{(122)}\ \ 0\ 0]^{\mathrm{T}} \\ &\quad + \frac{r_1}{6}\,\eta_{kj}\,\eta_{j\ell}\,\eta_{\ell 0}\,[0\ 0\ 0\ 0\ 0\ 0\ 0\ 0\ 0\ 1\ 0\ 0\ 0\ 0\ 0\ 0\ 0]^{\mathrm{T}},\end{aligned} \tag{4.75}$$

where $\eta_{k\ell}$ is given by (4.62), the $\psi_{j\ell}^{(\cdots)}$ are the solution of (4.38), while q_1 and r_1 give the values of q and r at the bifurcation point; cf. (4.4).

When considering the system at the Hopf bifurcation point ($p = p_1$) some cubic terms related to modes $k = 1$ and $k = N-1$ cannot be eliminated by the nonlinear transformations. In particular, considering (4.51) the determinant of the matrix $\tilde{\mathbf{A}}_{kj\ell}$ is 0 for the index combinations

$$\begin{aligned}&1)\quad k=1,\quad j=0,\quad \ell=N-1\,,\\ &2)\quad k=1,\quad j=0,\quad \ell=1\,,\\ &3)\quad k=1,\quad j=2,\quad \ell=1\,.\end{aligned} \tag{4.76}$$

Thus, we obtain that the dynamics of mode 1 are governed by two complex differential equations

$$\begin{aligned}\begin{bmatrix}\dot{w}_1^{(1)}\\ \dot{w}_1^{(2)}\end{bmatrix} &= \begin{bmatrix}0 & 1\\ \kappa_{10}^{(21)\,*} & \kappa_{10}^{(22)\,*}\end{bmatrix}\begin{bmatrix}w_1^{(1)}\\ w_1^{(2)}\end{bmatrix} + \frac{\eta_{10}^2\,\overline{\eta}_{10}\,r_1}{2}\begin{bmatrix}0\\ (w_1^{(1)})^2\,w_{N-1}^{(1)}\end{bmatrix}\\ &+ \overline{\eta}_{10}\,\eta_{20}\,q_1\begin{bmatrix}0\\ \psi_{21}^{(111)}\big(w_1^{(1)}\big)^2\,w_{N-1}^{(1)} + \big(\psi_{21}^{(112)}+\psi_{21}^{(121)}\big)w_1^{(1)}\,w_1^{(2)}\,w_{N-1}^{(1)} + \psi_{21}^{(122)}\big(w_1^{(2)}\big)^2\,w_{N-1}^{(1)}\end{bmatrix},\end{aligned} \tag{4.77}$$

where $\eta_{k\ell}$ is defined in (4.62), while $\kappa_{k\ell}^{(21)\,*}$ and $\kappa_{k\ell}^{(22)\,*}$ are given by (4.69). The equations for $w_{N-1}^{(1)}$ and $w_{N-1}^{(2)}$ can be obtained by taking the complex conjugate of (4.77). Explicit expressions for the quadratic near-identity coefficients $\psi_{21}^{(111)}$, $\psi_{21}^{(112)}+\psi_{21}^{(121)}$ and $\psi_{21}^{(122)}$ are given in Appendix G. We note that modes 1 and $N-1$ result in cubic terms in other modes. However, the dynamics for modes $k = 1$ and $k = N-1$ are not affected by the other modes.

4.3.3 Bifurcation analysis

To characterize the nonlinear oscillations in the vicinity of the stability loss we derive the normal form of the Hopf bifurcation using the nonlinear modal equation (4.77). Because modes 1 and $N-1$ contain eigenvalues that cross the imaginary axis at $p = p_1$, the corresponding four-dimensional manifold contains the two-dimensional center manifold. We can obtain the normal form of the Hopf bifurcation by projecting the modal system onto the center manifold. Due to the complex conjugacy of the modes 1 and $N-1$ involved in the bifurcation, we only need to use one mode to perform the projection and we choose mode 1. At the bifurcation point, mode 1 has one purely imaginary eigenvalue $\lambda_{\rm cr} = \mathrm{i}\omega_1$, where ω_1 is given by (4.65). Using (4.69) in the linear part of (4.77) one may obtain the corresponding eigenvector

$$\mathbf{e} = \begin{bmatrix} 1 \\ \mathrm{i}\,\omega_1 \end{bmatrix}, \tag{4.78}$$

while left eigenvector corresponding to $\overline{\lambda}_{\rm cr} = -\mathrm{i}\omega_1$ is given by

$$\mathbf{f} = \frac{1}{\alpha + \omega_1\,(2\tan(\frac{\pi}{N}) - \mathrm{i})} \begin{bmatrix} \alpha + \omega_1 \tan(\frac{\pi}{N}) \\ 1 + \mathrm{i}\tan(\frac{\pi}{N}) \end{bmatrix}. \tag{4.79}$$

The coefficient in front of the left eigenvector is obtained from the orthogonality condition $\mathbf{f}\cdot\mathbf{e} = 1$, where the inner product is defined by (4.34).

Let us define the complex variable

$$\zeta = \mathbf{f}\cdot\mathbf{w}_1\,. \tag{4.80}$$

Multiplying (4.77) by $\mathbf{f}$ from the left we may project the dynamics onto the center manifold; see [46]. Exploiting $\mathbf{w}_1 \approx \zeta\mathbf{e}$ we obtain the dynamics

$$\dot{\zeta} = \mathrm{i}\omega_1\,\zeta + \delta\,\zeta^2\,\overline{\zeta}\,, \tag{4.81}$$

where the cubic coefficient is given by

$$\delta = \frac{\overline{\eta}_{10}\big(1 - \mathrm{i}\tan(\frac{\pi}{N})\big)}{2\big(\alpha + \omega_1\,(2\tan(\frac{\pi}{N}) + \mathrm{i})\big)} \left(r_1\,\eta_{10}^2 + 2\,q_1\,\eta_{20}\Big(\psi_{21}^{(111)} + \mathrm{i}\omega_1\,(\psi_{21}^{(112)} + \psi_{21}^{(121)}) - \omega_1^2\,\psi_{21}^{(122)}\Big)\right). \tag{4.82}$$

The sign of Re δ determines whether the Hopf bifurcation is supercritical or subcritical.

For a supercritical Hopf bifurcation ($\operatorname{Re}\delta < 0$) stable oscillations arise around the unstable equilibrium, while in the subcritical case ($\operatorname{Re}\delta > 0$) unstable oscillations emerge around the stable equilibrium. Subcritical Hopf bifurcations may lead to bistability as discussed in [67]. Thus, it is important to determine the criticality of the bifurcation in order to evaluate the effect of the CCC controllers at the nonlinear level.

To calculate the amplitude of the nonlinear oscillations near the Hopf point we also need the "speed" of the critical eigenvalues crossing the imaginary axis as the parameter p is varied:

$$\operatorname{Re}\frac{\mathrm{d}\lambda}{\mathrm{d}p}(p_1) = \frac{\omega_1 \sin(\frac{2\pi}{N})}{\left(\omega_1 \tan(\frac{\pi}{N}) + \alpha\right)^2 \cos^4(\frac{\pi}{N}) + 4\tan^2(\frac{\pi}{N})\left(\beta(1+\sin^2(\frac{\pi}{N})) + \alpha\right)^2}. \quad (4.83)$$

In the vicinity of the Hopf point, the invariant oscillations are well approximated by

$$\zeta(t) \approx \mathrm{Amp}_\zeta \mathrm{e}^{\mathrm{i}(\omega_1 t + \alpha_0)}, \quad (4.84)$$

where the phase α_0 can be chosen arbitrarily, the frequency ω_1 is given by (4.65), while the amplitude is given by

$$\mathrm{Amp}_\zeta = \sqrt{-\frac{\operatorname{Re}\frac{\mathrm{d}\lambda}{\mathrm{d}p}(p_1)}{\operatorname{Re}\delta}(p-p_1)}. \quad (4.85)$$

Using (4.80) the approximations $\mathbf{w}_1 \approx \zeta\mathbf{e}$ and $\mathbf{z}_1 \approx \mathbf{w}_1$ result in

$$\mathbf{z}_1(t) = \begin{bmatrix} z_1^{(1)}(t) \\ z_1^{(2)}(t) \end{bmatrix} \approx \begin{bmatrix} \mathrm{Amp}_\zeta\, \mathrm{e}^{\mathrm{i}(\omega_1 t + \alpha_0)} \\ \omega_1\, \mathrm{Amp}_\zeta\, \mathrm{e}^{\mathrm{i}(\omega_1 t + \frac{\pi}{2} + \alpha_0)} \end{bmatrix}. \quad (4.86)$$

Finally, using (4.22) and $\mathbf{y}_i = [\widetilde{s}_i, \widetilde{v}_i]^{\mathrm{T}}$, the velocity of the i-th vehicle can be approximated as

$$\widetilde{v}_i(t) = \mathrm{e}^{\mathrm{i}\frac{2\pi(i-1)}{N}} z_1^{(2)} + \mathrm{e}^{-\mathrm{i}\frac{2\pi(i-1)}{N}} z_{N-1}^{(2)} \approx \frac{\mathrm{Amp_v}}{2}\cos(\omega_1 t + \alpha_i), \quad (4.87)$$

where the peak-to-peak amplitude is given by

$$\mathrm{Amp_v} = 4\,\omega_1 \sqrt{-\frac{\operatorname{Re}\frac{\mathrm{d}\lambda}{\mathrm{d}p}(p_1)}{\operatorname{Re}\delta}(p-p_1)}, \quad (4.88)$$

and $\alpha_i = \alpha_0 + \frac{\pi}{2} + \frac{2\pi}{N}(i-1)$ is the phase offset for the i-th car. Choosing $\alpha_0 = -\frac{\pi}{2} + \frac{2\pi}{N}$ yields $\alpha_i = \frac{2\pi}{N} i$; making it obvious that (4.87) describes a traveling wave [65].

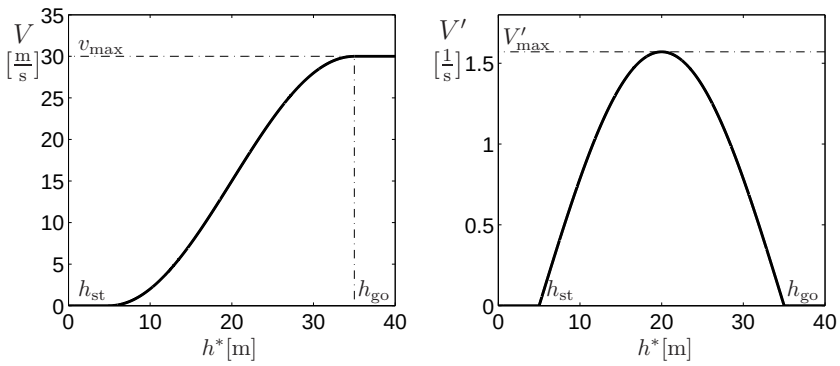

Figure 4.2: The nonlinear range policy function (2.5,2.8) (left) and its derivative (right). The headways h_{st} and h_{go}, the free-flow speed $v_{\max}$, and the maximum of the derivative $V'_{\max}$ are indicated. In this case $h_{\mathrm{st}} = 5\,[\mathrm{m}]$, $h_{\mathrm{go}} = 35\,[\mathrm{m}]$, $v_{\max} = 30\,[\mathrm{m/s}]$, $V'_{\max} = \frac{\pi}{2}\,[1/\mathrm{s}]$

Notice that according to (4.4) we have $p_1 = \alpha V'(h^*_{\mathrm{cr}})$, that is, when varying the average distance of vehicles h^*, the parameter p changes and the critical value of p_1 corresponds to some critical headway h^*_{cr}. If we wish to consider h^* as the bifurcation parameter, we can use (4.4) to obtain

$$\mathrm{Re}\,\frac{\mathrm{d}\lambda}{\mathrm{d}h^*}(h^*_{\mathrm{cr}}) = \mathrm{Re}\,\frac{\mathrm{d}\lambda}{\mathrm{d}p}(p_1)\,\frac{\mathrm{d}p}{\mathrm{d}h^*}(h^*_{\mathrm{cr}}) = q_1\,\mathrm{Re}\frac{\mathrm{d}\lambda}{\mathrm{d}p}(p_1)\,, \tag{4.89}$$

and rewrite the peak-to-peak amplitude for velocity oscillations (4.88) as

$$\mathrm{Amp_v} = 4\,\omega_1\sqrt{-q_1\,\frac{\mathrm{Re}\,\frac{\mathrm{d}\lambda}{\mathrm{d}p}(p_1)}{\mathrm{Re}\,\delta}\,(h^* - h^*_{\mathrm{cr}})}\,. \tag{4.90}$$

4.4 Numerical Verification

In this section we validate our analytical results using numerical continuation for the smooth range policy (2.5,2.8); that is plotted together with its derivative in Fig. 4.2 for $h_{\mathrm{st}} = 5\,[\mathrm{m}]$, $h_{\mathrm{go}} = 35\,[\mathrm{m}]$, and $v_{\max} = 30\,[\mathrm{m/s}]$ yielding $V'_{\max} = 30\,[1/\mathrm{s}]$ that is used in the rest of the section. Because all of the vehicles use the same range policy shown in Figure 4.2, we denote the average spacing $h^*_{\mathrm{avg}} = L/N$ as h^*, as for uniform flow the average spacing would indeed equal the headway of each vehicle. We chose h^* as the bifurcation parameter and present the results for different values of the parameters α and β to evaluate the effects of the CCC controller on the system dynamics. Note that due to the properties of the range policy (2.5,2.8), each p_1 corresponds to two h^*_{cr} values, such that $p > p_1$ for the middle

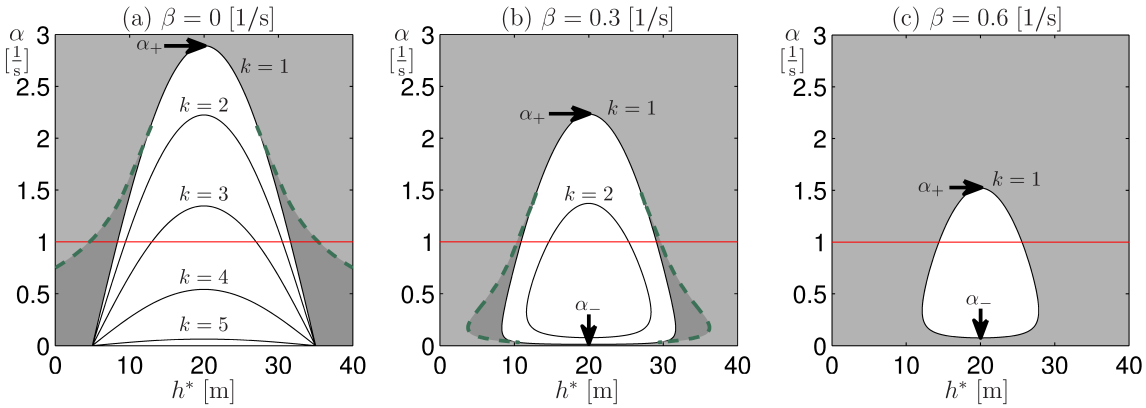

Figure 4.3: Two-dimensional bifurcation diagrams in the (h^*, α)-plane for $N = 11$ cars when considering different values of β as indicated. The black curves are the linear stability boundaries for the modes $k = 1, \ldots, 5$. The dashed green curves show where the periodic solutions for $k = 1$ undergo fold bifurcations. Light gray shading indicates globally stable uniform flow. In the white region the uniform flow is unstable and stable oscillations appear. The dark gray region corresponds to bistability between the equilibrium and oscillations. The red horizontal lines correspond to the panels in Fig. 4.4

range of headways.

4.4.1 Bifurcation diagrams

In Fig. 4.3 the results are summarized in the (h^*, α)-plane for different values of the parameter β when considering $N = 11$ cars. Solid black curves denote the modal stability boundaries, while green dashed curves denote the fold bifurcations of the oscillatory solutions for $k = 1$ (explained further below). In the light gray region the uniform flow equilibrium is globally stable. In the white region the equilibrium is unstable and there exist globally stable oscillatory solutions. In the dark gray region bistability occurs between the stable uniform flow and the oscillations. Since the stability boundaries for modes k and $N-k$ are the same due to complex conjugacy we only consider $k = 1, \ldots, \lfloor \frac{N}{2} \rfloor$. Each modal boundary encloses a region in the parameter space where the corresponding mode is linearly unstable. Notice that the instability regions for higher mode numbers are contained in the instability regions for lower mode numbers. This corresponds to the fact that (4.64) increases monotonically with the mode number k between 1 and $\lfloor \frac{N}{2} \rfloor$. Thus, $k = 1$ gives the stability boundary of the uniform flow. Fig. 4.3(a) shows the two dimensional bifurcation diagram without relative velocity feedback ($\beta = 0$). In this case all five modal stability boundaries appear. For $\beta > 0$ the modal stability boundaries become closed curves and the modal instability regions shrink (and may even disappear) when β is increased as depicted in Fig. 4.3(b,c).

In order to quantify how the stability chart changes with β, we determine the maximum α_+ and the minimum α_-; see Fig. 4.3, and use these extrema to calculate the critical value of β where the linearly unstable domain disappears. To find $\alpha_\pm$ we substitute $V'(h) = V'_{\max}$ and $k = 1$ into (4.64) which yields

$$\alpha_\pm = (\beta + V'_{\max})\cos^2(\tfrac{\pi}{N}) - 2\beta \pm \sqrt{\left((\beta + V'_{\max})\cos^2(\tfrac{\pi}{N}) - 2\beta\right)^2 - 4\sin^2(\tfrac{\pi}{N})\beta^2}\,. \tag{4.91}$$

One can show that α_- increases while α_+ decreases with β and the instability region disappears when $\alpha_+ = \alpha_-$ that occurs at the β value

$$\beta_{\text{cr}} = V'_{\max}\,\frac{1-\sin(\frac{\pi}{N})}{1+\sin(\frac{\pi}{N})}\,. \tag{4.92}$$

That is, for $\beta > \beta_{\text{cr}}$ no unstable region exists. For $N = 11$ cars we obtain $\beta_{\text{cr}} \approx 0.880\,[1/\text{s}]$.

While the linear stability analysis reveals where the uniform traffic flow loses linear stability, the bifurcation analysis gives insight about what happens at the nonlinear level. Here we compare the peak-to-peak amplitude (4.90) calculated analytically to the amplitudes computed using numerical continuation [78]. In Fig. 4.4 we plot the branches of oscillations for mode 1 considering different values of β for $N = 11$ cars and $\alpha = 1\,[1/\text{s}]$; see the red horizontal lines in Fig. 4.3. The horizontal axis represents the uniform flow equilibrium. Stable and unstable solutions are shown as solid green and dashed red curves, respectively. The oscillatory solutions arise from Hopf bifurcations marked by blue stars, and may undergo fold bifurcations marked by black pluses. The zoom-ins at the bottom compare the analytical results (black) and the numerical results (colored) at the vicinity of the Hopf bifurcation points. The bifurcation diagrams are symmetric about $h^* = \frac{h_{\text{go}}+h_{\text{st}}}{2}$ due to the symmetry of the range policy function (2.5,2.8). In each case the bifurcations partition the diagrams into different regimes of qualitative behavior.

In Fig. 4.4(a) the Hopf bifurcations are supercritical and give rise to stable periodic solutions, but the stability changes via fold bifurcation soon after birth (see the zoomed panels at the bottom). For large amplitudes the stability of the periodic orbits changes again through fold bifurcations leading to stable large-amplitude oscillations. These bifurcations yield four qualitatively different regimes. For headways outside the high amplitude fold points the uniform flow is globally stable and no oscillations appear. In the region in between the

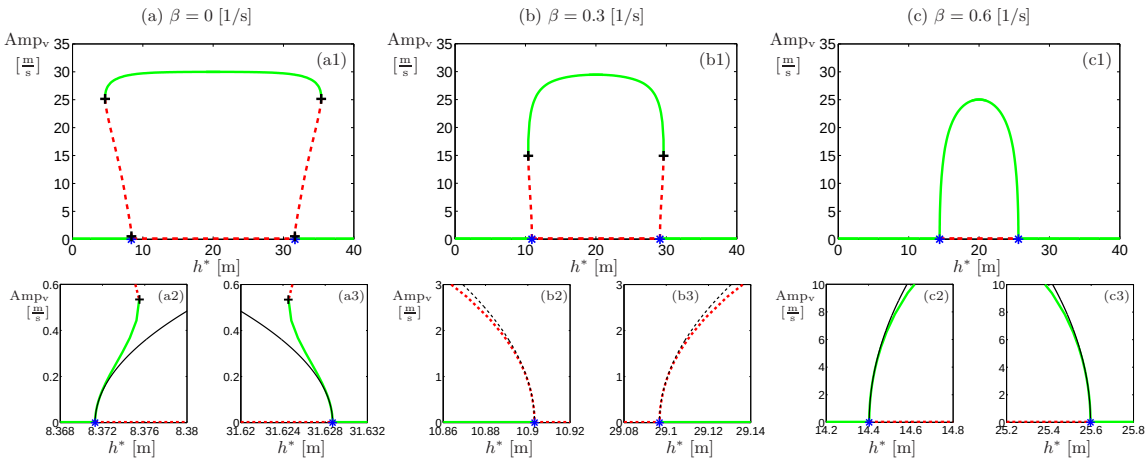

Figure 4.4: Bifurcation diagrams for $N = 11$ cars and $\alpha = 1\,[1/\mathrm{s}]$ for different values of β as indicated. In each panel, the peak-to-peak velocity amplitude $\mathrm{Amp_v}$ is shown as a function of the bifurcation parameter h^*. The horizontal axis represents the uniform flow equilibrium. Stable states are depicted as solid green and unstable states are shown as dashed red curves. Hopf bifurcations are marked by blue stars and fold bifurcations of periodic orbits are marked by black pluses. The bottom panels zoom onto the at the Hopf points and also show the analytical predictions (4.90) as black lines

low-amplitude fold points the uniform flow is unstable while the high amplitude oscillations are globally stable. In the bistable regimes bordered by a high-amplitude fold point and a Hopf point the uniform flow is linearly stable, but stable large-amplitude oscillations are also present, and the stable states are separated by unstable oscillations. Other bistable regimes are bordered by a Hopf point and a low-amplitude fold point where the uniform flow is unstable, but there exist stable low-amplitude and high-amplitude oscillations separated by unstable oscillations. We remark that this behavior happens in a very narrow parameter domain and is not visible in the two dimensional bifurcation diagram in Fig. 4.3(a).

When β is increased the domain where the equilibrium is unstable shrinks as can be observed in Fig. 4.4(b) (cf. Fig. 4.3(b)). Nonlinear analysis shows that the Hopf bifurcations are now subcritical, leading to unstable oscillations. The low-amplitude fold bifurcations disappear while the high amplitude fold points move closer to each other. Here the bifurcations create three regimes of qualitatively different behavior. Again outside the fold points the uniform flow is globally stable while between the Hopf points the uniform flow is unstable and the high amplitude velocity oscillations are globally stable. However only one kind of bistable regime exists between the Hopf and fold points, where the equilibrium and the large-amplitude oscillations are both stable. For larger β values stable oscillatory solutions exist only between the Hopf points where the uniform flow is

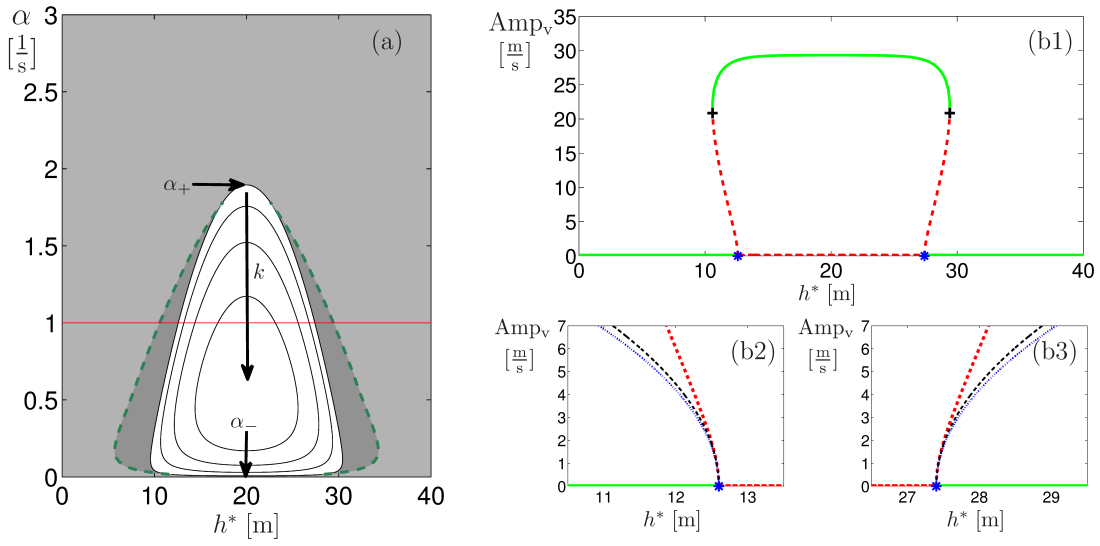

Figure 4.5: (a) Two-dimensional bifurcation diagram for $N = 33$ cars and $\beta = 0.6\,[1/\mathrm{s}]$. (b) Bifurcation diagram for $N = 33$ cars, $\alpha = 1\,[1/\mathrm{s}]$, and $\beta = 0.6\,[1/\mathrm{s}]$. The same notation is used as in Fig. 4.3 and Fig. 4.4. The blue dotted curves in panels (b2) and (b3) show the analytical prediction for $N \to \infty$ as given by (4.96)

unstable as shown in Fig. 4.4(c) and outside this regime the uniform flow is globally stable. When β is increased even further, the Hopf points move closer to each other and the branch of stable oscillations disappears at $\beta \approx 0.786\,[1/\mathrm{s}]$.

4.4.2 Large N limit

Now we demonstrate how the number of cars N influences the nonlinear behavior. Indeed, we are interested in the large N limit. First, we consider $N = 33$ cars and $\beta = 0.6\,[1/\mathrm{s}]$. Fig. 4.5(a) shows a two-dimensional bifurcation diagram in the (h^*, α)-plane (cf. Fig. 4.3(b)), while a bifurcation diagram is displayed in Fig. 4.5(b) for $\alpha = 1\,[1/\mathrm{s}]$, (cf. Fig. 4.4(b)). The linearly unstable region is similar to the 11-car case but we have larger number of modal stability boundaries. Still mode 1 determines the linear stability of the uniform flow. One may observe that stability is lost via subcritical Hopf bifurcations and the bifurcation diagram is qualitatively similar to the one in Fig. 4.4(b).

To get a broader picture about how the nonlinear oscillatory solutions depend on the number of vehicles, we consider $\alpha = 1\,[1/\mathrm{s}]$ and evaluate the sign of $\mathrm{Re}\,\delta$ in (4.81) while varying N and β. We plot the results in Fig. 4.6, where supercritical Hopf bifurcations occur in the green area, subcritical Hopf bifurcations occur in the red area, and no bifurcations

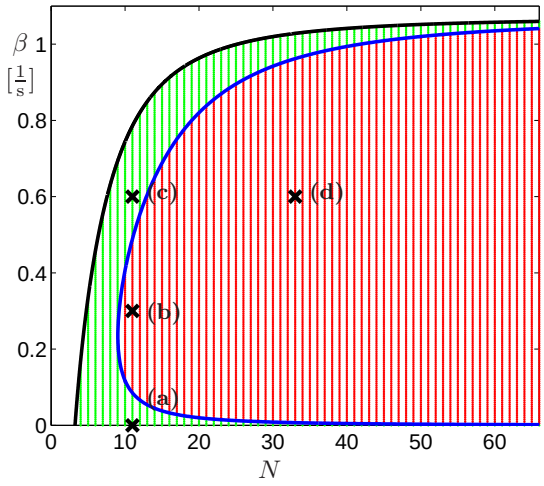

Figure 4.6: Criticality diagram for $\alpha = 1\,[1/\mathrm{s}]$. Green shading represents supercritical Hopf bifurcations, red shading represents subcritical Hopf bifurcations. These are separated by the blue curve. The system does not undergo a Hopf bifurcation in the white region and the Hopf boundary is represented by the black curve. The points marked (a), (b), (c) correspond to the three cases examined in Fig. 4.3 and Fig. 4.4, while the point marked (d) corresponds to Fig. 4.5

take place in the white area. The black curve denotes the linear stability boundary, while the blue curve denotes the boundary where criticality of the Hopf bifurcation changes. For a small numbers of cars ($N < 10$) only supercritical Hopf bifurcations are possible. When N is increased the unstable regime expands and the bifurcation turns subcritical for a range of β that also grows with N.

In the large N limit the black stability boundary approaches an asymptotic value that can be obtained by using $p_1 = \alpha V'_{\max}$ and $N \to \infty$ in (4.64):

$$\beta_{\max} = V'_{\max} - \frac{\alpha}{2}. \tag{4.93}$$

Considering the range policy (2.5,2.8) and $\alpha = 1\,[1/\mathrm{s}]$ yields $\beta_{\max} = (\pi - 1)/2 \approx 1.071\,[1/\mathrm{s}]$; see the black curve in Fig. 4.6. Also, the blue criticality boundary approaches the horizontal axis and the black Hopf bifurcation boundary which indicates that the typical behavior is subcritical for large number of cars as demonstrated in Fig. 4.5. This can also be seen when replacing the trigonometric functions in (4.82) by their Taylor series which in the large N limit yields

$$\operatorname{Re}\delta_\infty \approx \frac{3q_1^2\beta}{(3\beta+\alpha)^2\alpha^2}\left(\frac{2\pi}{N}\right)^2 > 0, \tag{4.94}$$

showing that $\operatorname{Re}\delta_\infty$ is positive for the whole domain $0 < \beta < \beta_{\max}$.

Similarly, taking the large N limit in (4.83) gives

$$\operatorname{Re}\frac{\mathrm{d}\lambda}{\mathrm{d}h^*}(h^*_{\mathrm{cr}\infty}) \approx \frac{q_1(2\beta+\alpha)}{2\,\alpha^2}\left(\frac{2\pi}{N}\right)^2. \tag{4.95}$$

Thus for large N the Hopf amplitude (4.90) is given by

$$\mathrm{Amp}_{\mathrm{v}\infty} \approx 4(3\beta+\alpha)(2\beta+\alpha)\frac{\pi}{N}\sqrt{-\frac{2\beta+\alpha}{6\beta\,q_1}(h^*-h^*_{\mathrm{cr}})}, \tag{4.96}$$

where we used (4.65) with $k = 1$. The blue dotted curves in Fig. 4.5 correspond to (4.96) and these are well approximated by the black curves shown for $N = 33$. However, observe that $\mathrm{Amp}_{\mathrm{v}\infty} \to \infty$ as $\beta \to 0$ or $q_1 \to 0$. The latter case corresponds to $\beta \to \beta_{\max}$, since the black stability boundary in Fig. 4.6 corresponds to the inflection point of the range policy. This shows that in the large N limit the lower criticality boundary tends to $\beta = 0$ while the upper criticality boundary tends to $\beta = \beta_{\max}$. Thus choosing sufficiently large β guarantees global stability of the uniform flow, which demonstrates the benefit of relative velocity feedback in CCC design.

4.5 Summary

In this chapter we analyzed the dynamics of connected vehicle systems where vehicles respond to the motion of other vehicles ahead. These systems were used as a motivation to develop network-based bifurcation analysis based on nonlinear normal modes (NNMs). Our method simplified the bifurcation analysis of large coupled systems with cyclic symmetry. A linear transformation was used to write the dynamics into modal coordinates, and subsequent nonlinear network-based transformations were used to eliminate the quadratic and cubic terms. These led to a small number of algebraic equations for each mode that can be solved without considering the dynamics of other modes.

We applied the algorithm to a connected vehicle system where each vehicle reacts to the distance and the relative velocity to the vehicle directly ahead (conventional vehicles). After performing the linear transformation we detected the mode responsible for the stability loss of the uniform flow. We then decoupled this mode from the rest of the system using the nonlinear near-identity transformations and projected the dynamics onto the center

manifold to find the normal form of the Hopf bifurcation. These nonlinear near-identity transformations were reduced to linear algebraic equations that were decoupled using the cyclic symmetry of the network. Specifically for a system of N nodes and 2 equations per node we need to solve N decoupled systems of 8 equations to eliminate the quadratic terms, and N^2 decoupled systems of 16 equations to eliminate the cubic terms. By comparison, if the cyclic symmetry is neglected, we would have to solve a system of $8N^2$ linear equations to eliminate the quadratic terms, and $16N^3$ equations to eliminate the cubic terms. For example, if we have 100 nodes, then for quadratic terms we only need to solve 100 decoupled linear systems of 8 unknowns as opposed to a system of 80000 coupled linear equations. For the third order terms we only need to solve 10000 decoupled linear systems of 16 unknowns as opposed to an equation with 16 million coupled linear equations. This gives a significant simplification to the nonlinear analysis of large cyclic systems. This network-based approach allowed us to analytically determine the criticality and amplitudes the nonlinear oscillations arising at the bifurcation point and observe the effects of the controller feedback law on the system dynamics. We validated our network-based algorithm by comparing the analytical results to those obtained by numerical continuation.

The developed network-based tools allowed us to characterize the traffic patterns developing in a network where identical vehicles rely on information of the vehicle directly ahead. Knowing the behavior of this baseline network, the logical next step is analyze connected vehicle networks where beyond-line-of-sight information is used in order to assess the benefits of V2V communication in connected vehicle networks.

CHAPTER 5

Network-based analysis of connected vehicle networks with beyond-line-of-sight connectivity

The advantages of a connected vehicle network over a traditional network are reaped from connected and automated vehicles exploiting the beyond-line-of-sight V2V communication. These vehicles are mixed into the traffic flow with conventional vehicles ad-hoc as shown in Figure 5.1 D). To evaluate the effect of connected automated vehicles at a system level demands methods that account for the heterogeneity of vehicles and communication strategies of mixed traffic. Such methods shall allow for reduction of the dynamics of large vehicle systems without being computationally demanding.

To simplify the analysis of a network of connected nodes, we first consider a system with simple connectivity structure and then use perturbation theory to analyze networks with more complex connectivity structures. In the literature, perturbation theory was used to analyze the modes of near-cyclic systems dealing with vibrations and localized modes of bladed disc assemblies [33, 47, 70, 105]. In particular, closed-form analytical approximations for the eigenvalues and modes of mistuned bladed disc assemblies were obtained by expanding the equations around the corresponding cyclically symmetric assembly. Such perturbation analysis was more computationally effective compared to a global eigenvalue analysis and also gave insight about the effects of mistuning on the frequencies and mode shapes for simple one-degree-of-freedom mechanical systems with nearest neighbor interactions. Recently, modal perturbation analysis was used in [95] to evaluate the performance of a CVN where each vehicle is modeled by a delay differential equation. The technique allowed the authors to characterize the modal stability boundaries of a network of 3 connected vehicles on the ring road. However, the analysis did not exploit the cyclic structure of the network and such analysis would become cumbersome (or impossible) for a larger number of vehicles with more complex dynamics and interaction laws.

In this chapter we develop a network-based modal analysis technique for perturbed cyclic systems with an arbitrary number of nodes, multiple equations per node and for multiple

acyclic perturbations. By exploiting the cyclic structure of the unperturbed system, we use a series of steps to decompose the perturbed cyclic system into decoupled modal equations. Such a modal decomposition can be performed for systems with arbitrary numbers of nodes and an arbitrary number of perturbations without significant increase in complexity. The linear stability conditions can then be evaluated independently for each mode and the effects of the perturbations on modal stability can be quantified. In addition to being convenient for systems with large numbers of nodes and acyclic perturbations, this technique allows one to determine analytical relationships between system parameters and modal behavior, which would be extremely difficult and cumbersome with traditional analytical and numerical stability analysis. We use the developed technique to examine the linear stability of a CVN consisting of both conventional vehicles and connected automated vehicles, and analyze how the gain parameter used for the long-range connections shall be selected to stabilize the traffic flow.

The layout of the chapter is as follows. A general perturbation method to estimate the modal dynamics of a cyclic system with a general class of acyclic perturbations is presented in Section 5.2. In Section 5.3 we utilize this method to estimate the modal dynamics of CVN. We also examine the stability of several specific connected vehicle configurations and validate the developed modal perturbation technique using numerical continuation. Finally, we discuss the implications of the results and lay out future research directions in Section 5.4.

5.1 Simplified model for connected automated vehicle car following

In this section we extend our analysis to general connected vehicle networks featuring connected vehicles and connected automated vehicles in addition to regular human driven vehicles. The main goal of this chapter is quantify the effects of utilizing long-range feedback due to the wireless communication of CAVs at partial penetrations of CVs and CAVs on the traffic patterns. We build up the connected vehicle network by starting with a network of N regular human-driven vehicles which we analyzed extensively in the previous chapter. Figure 5.1 A) shows such a network for 11 vehicles moving counterclockwise, marked by grey dots. The dynamics of these vehicles are given by (4.1) as discussed in the previous chapter. After this we select a few of these vehicles to become connected vehicles. For example in Figure 5.1 B), $i = 1, 3, 6, 7, 9, 11$ are selected to be connected vehicles. We then select a fraction of the connected vehicles to be connected automated vehicles

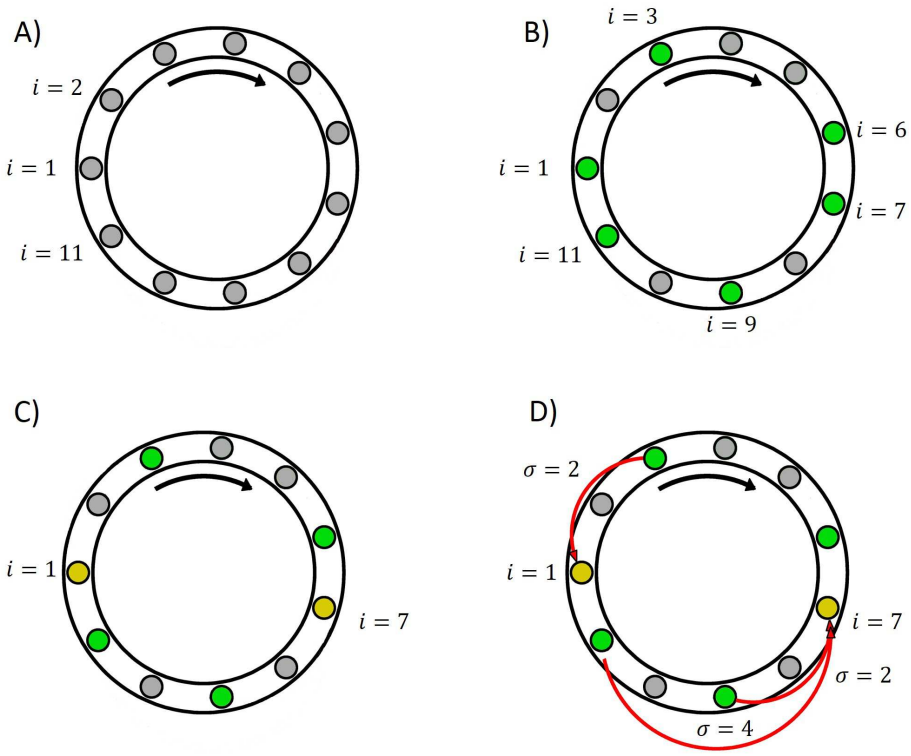

Figure 5.1: Four steps of setting up an 11-car connected vehicle network on a ring road A): Regular human driven vehicles (HVs) represented by gray circles are placed on a single lane road. The black arrow represents the direction of the traffic flow. B): Connected vehicles (CVs) are added to the network (highlighted as green). C): Some of the connected vehicles become connected automated vehicles (CAVs) highlighted by yellow dots. D): V2V links are set up between CVs and CAVs by assuming that each CAV can receive information from up to 4 CVs ahead of it.

(CAV's), while the rest of the vehicles stay connected human-driven vehicles (CHV's). In Figure 5.1 C) vehicles $i = 1, 7$ are CAVs, while $i = 3, 6, 9, 11$ are CHVs. Finally to form a connected vehicle network , the CAVs use the information from connected vehicles downstream to control their longitudinal motion. To develop our analytical tools we simplify the car-following dynamics of the connected automated vehicles (2.1,2.13,2.15,2.17) by excluding the delay and saturation. Furthermore, we model the dynamics as a continuous time process, assuming that the information coming in from wireless communication is streamed to each connected automated vehicle rather than broadcasted periodically. The latter can be interpreted as a variable delay in the dynamics [75, 76], so this simplification is in line with eliminating the delays due to reaction and actuation. The dynamics can be then

written as

$$\begin{aligned}\dot{s}_i &= v_i,\\ \dot{v}_i &= \alpha\left(V(s_{i+1}-s_i-\ell_i)-v_i\right)+\beta_1\left(v_{i+1}-v_i\right)+\sum_{\sigma=2}^{\sigma_{\max}}\beta_{i\sigma}(v_{i+\sigma}-v_i)\,.\end{aligned} \tag{5.1}$$

Note that in this case we use the same smooth range policy as for the human driven vehicles. Furthermore in (2.13) we set $a=\alpha$. We rewrite the relative velocity feedback (2.13) as a sum of feedbacks from vehicle $i+1$ (with gain β_1) and beyond-line-of-sight vehicles $i+\sigma$ where $\sigma=2,\ldots,\sigma_{\max}$, with gain $\beta_{i\sigma}$ such that

$$\beta_1+\sum_{\sigma=2}^{\sigma_{\max}}\beta_{i\sigma}=b. \tag{5.2}$$

In other words σ represents the length of the communication link between a CV and a CAV. In Figure 5.1 D) we see two links with link length $\sigma=2$ and one link with length $\sigma=4$. In connected vehicle networks links up to $\sigma\approx 4$ were shown to have significant benefit [27], so in this chapter we consider $\sigma_{\max}=4$, but the developed framework can be used for links of arbitrary length. Finally for the human driven vehicles in (4.1) we set $\beta=\beta_1$, so that the only difference between (5.1) and (4.1) are the velocity feedback terms from vehicles beyond-line-of-sight.

Due to the range policy being the same for all drivers, note that the uniform flow state (2.18-2.22) remains the same for N vehicles in the network no matter how many of them are human driven or connected automated. Thus the above simplifications allow us to analyze solely the effect of the added long-range communication links on the stability of uniform flow. The perturbations about uniform flow are defined as before (4.2) and the cubic order Taylor expansion of yields

$$\begin{aligned}\dot{\widetilde{s}}_i &= \widetilde{v}_i\,,\\ \dot{\widetilde{v}}_i &= p\,(\widetilde{s}_{i+1}-\widetilde{s}_i)+\frac{q}{2}(\widetilde{s}_{i+1}-\widetilde{s}_i)^2+\frac{r}{6}(\widetilde{s}_{i+1}-\widetilde{s}_i)^3+\beta_1\,(\widetilde{v}_{i+1}-\widetilde{v}_i)-\alpha\,\widetilde{v}_i+\sum_{\sigma=2}^{\sigma_{\max}}\beta_{i\sigma}(\widetilde{v}_{i+\sigma}-\widetilde{v}_i),\end{aligned} \tag{5.3}$$

In this chapter we investigate how a connected vehicle network where human-driven vehicles modeled by (4.1) and connected automated vehicles modeled by (5.1) performs compared to a network composed solely of human drivers. To do this investigation we develop analytical tools for scalable stability analysis of such connected vehicle networks.

5.2 Network-Based Analysis of Cyclic Systems with Acyclic Perturbations

In this section we develop methods for the linear modal analysis of systems with an underlying cyclic structure that is perturbed by long-range connections (that make the system acyclic). We write the Jacobian of the overall system as a sum of a block circulant matrix (representing the unperturbed cyclic system) and perturbation (matrices representing the long-range connections). First we obtain the modes using a linear transformation for the unperturbed cyclic system. This is a well known problem and was extensively discussed in [59]. We then develop a perturbation method to approximate the modes for the perturbed acyclic system around the cyclically symmetric configuration. We exploit the cyclic structure of the unperturbed system to reduce the complexity of calculations when solving for the modes of the perturbed acyclic system. As mentioned above, such a modal decomposition can be performed for systems with arbitrary numbers of nodes and an arbitrary number of perturbations without significant increase in complexity. Our network-based modal analysis also reveals how different parameters influence modal and system stability.

Assuming the state of the i-th node is described by the vector $\mathbf{x}_i = [x_i^{(1)},\ldots,x_i^{(M)}]^{\mathrm{T}}$, its dynamics can be written as

$$\dot{\mathbf{x}}_i = \mathbf{g}(\mathbf{x}_i,\mathbf{x}_{i+1},\cdots,\mathbf{x}_{i+N-1}) + \sum_{\sigma=0}^{\sigma_{\max}} \mathbf{h}_{i\sigma}(\mathbf{x}_i,\mathbf{x}_{i+\sigma})\varepsilon_{i\sigma}, \tag{5.4}$$

where $\mathbf{x}_{N+i} \equiv \mathbf{x}_i$ and $\mathbf{g} = [g^{(1)},\ldots,g^{(M)}]^{\mathrm{T}}$ is a vector valued function that represents the cyclic coupling of the nodes. The vector valued functions $\mathbf{h}_{i\sigma} = [h_{i\sigma}^{(1)},\ldots,h_{i\sigma}^{(M)}]^{\mathrm{T}}$ represent the acyclic perturbations to the cyclic structure, while $\varepsilon_{i\sigma}$ represents the magnitude of the perturbations. We assume that the system possesses a equilibrium where all the nodes are synchronized

$$\mathbf{x}_i \equiv \mathbf{x}^*, \tag{5.5}$$

for $i = 1,\ldots,N$ satisfying $\mathbf{g}(\mathbf{x}^*,\ldots,\mathbf{x}^*) = \mathbf{0}$ and $\mathbf{h}_{i\sigma}(\mathbf{x}^*,\mathbf{x}^*) = \mathbf{0}$.

By defining the perturbation

$$\mathbf{y}_i = \mathbf{x}_i - \mathbf{x}^*, \tag{5.6}$$

where $\mathbf{y}_i = [y_i^{(1)}\ldots y_i^{(N)}]^{\mathrm{T}}$, we linearize (5.4) around the synchronous equilibrium (5.5) and obtain

$$\dot{\mathbf{y}}_i = \sum_{j=1}^{N} \mathbf{C}_j \mathbf{y}_{i+j-1} + \sum_{\sigma=0}^{\sigma_{\max}} (\partial_1 \mathbf{h}_{i\sigma}\mathbf{y}_i + \partial_2 \mathbf{h}_{i\sigma}\mathbf{y}_{i+\sigma})\varepsilon_{i\sigma}, \tag{5.7}$$

where the $M \times M$ matrices $\mathbf{C}_j$, $\partial_1 \mathbf{h}_{i\sigma}$, $\partial_2 \mathbf{h}_{i\sigma}$ are given by

$$[\mathbf{C}_j]_{bd} = \left.\frac{\partial g^{(b)}}{\partial x^{(d)}_{i+j-1}}\right|_*, \quad [\partial_1 \mathbf{h}_{i\sigma}]_{bd} = \left.\frac{\partial h^{(b)}_{i\sigma}}{\partial x^{(d)}_{i}}\right|_*, \quad [\partial_2 \mathbf{h}_{i\sigma}]_{bd} = \left.\frac{\partial h^{(b)}_{i\sigma}}{\partial x^{(d)}_{i+\sigma}}\right|_*, \tag{5.8}$$

where the asterisk denotes that the derivatives are evaluated at the synchronous equilibrium. Notice that $\mathbf{C}_j$ does not depend on i because the nodes are cyclically coupled. By defining the state vector $\hat{\mathbf{y}} = [\mathbf{y}_1^{\mathrm{T}} \dots \mathbf{y}_N^{\mathrm{T}}]^{\mathrm{T}}$ we can rewrite (5.7) into the compact form

$$\dot{\hat{\mathbf{y}}} = \hat{\mathbf{J}}\,\hat{\mathbf{y}}, \tag{5.9}$$

where the Jacobian

$$\hat{\mathbf{J}} = \hat{\mathbf{J}}_0 + \sum_{i_1=1}^{N} \sum_{\sigma_1=0}^{\sigma_{\max}} \hat{\mathbf{P}}(i_1, \sigma_1)\varepsilon_{i_1\sigma_1}, \tag{5.10}$$

is divided into parts corresponding to the cyclic system and the perturbations. Indeed, the cyclic coupling between the nodes is represented by

$$\hat{\mathbf{J}}_0 = \mathrm{circ}(\mathbf{C}_1, \dots, \mathbf{C}_N) = \begin{bmatrix} \mathbf{C}_1 & \mathbf{C}_2 & \cdots & \mathbf{C}_N \\ \mathbf{C}_N & \mathbf{C}_1 & \cdots & \mathbf{C}_{N-1} \\ \vdots & \vdots & \ddots & \vdots \\ \mathbf{C}_2 & \mathbf{C}_3 & \cdots & \mathbf{C}_1 \end{bmatrix}, \tag{5.11}$$

that is a block-circulant matrix of type (M,N); see [59]. The terms

$$\hat{\mathbf{P}}(i_1, \sigma_1) = \mathbf{\Delta}_{i_1 i_1} \otimes \partial_1 \mathbf{h}_{i_1\sigma_1} + \mathbf{\Delta}_{i_1 i_1+\sigma_1} \otimes \partial_2 \mathbf{h}_{i_1\sigma_1}, \tag{5.12}$$

represent the perturbations to the cyclic structure where $\mathbf{\Delta}_{ij} \in \mathbb{R}^{N\times N}$ contains a "1" in the i-th row and the j-th column, and zeros everywhere else. The symbol $\otimes$ denotes the Kronecker product. Indeed, the matrix $\hat{\mathbf{P}}(i_1, \sigma_1)$ corresponds to a particular link of length σ_1 starting at node $i_1 + \sigma_1$ and ending at node i_1, cf. Figure 5.1 D). In $\hat{\mathbf{P}}(i_1, \sigma_1)$ we use brackets instead of subscripts in order to improve the readability.

5.2.1 Modal analysis of cyclic systems

Before obtaining approximations of the modes for the system with acyclic perturbations we obtain the modes of the cyclic system; see [59]. In particular, we use a linear modal transformation that exploits the circulant structure of the Jacobian $\hat{\mathbf{J}}_0$ given in (5.10). When considering (5.9,5.10) with $\varepsilon_{i_1\sigma_1} = 0$, (5.11) can be represented as a linear combination of

its generating elements using the Kronecker product

$$\hat{\mathbf{J}}_0 = \sum_{j=1}^{N} (\mathbf{A}_N)^{(j-1)} \otimes \mathbf{C}_j, \tag{5.13}$$

where the N-dimensional forward shift matrix $\mathbf{A}_N = [a_{ij}]$ contains elements defined as

$$a_{ij} = \begin{cases} 1 & \text{if} \quad j = i+1, \\ 0 & \text{otherwise}. \end{cases} \tag{5.14}$$

We define the linear coordinate transformation

$$\hat{\mathbf{y}} = \hat{\mathbf{T}}_0 \hat{\mathbf{z}}, \tag{5.15}$$

with modal coordinates $\mathbf{z}_k = [z_k^{(1)} \ \dots \ z_k^{(M)}]^{\mathrm{T}}$, $\hat{\mathbf{z}} = [\mathbf{z}_1^{\mathrm{T}} \ \dots \ \mathbf{z}_N^{\mathrm{T}}]^{\mathrm{T}}$, and matrix

$$\hat{\mathbf{T}}_0 = \mathbf{T}_N \otimes \mathbf{I}_M. \tag{5.16}$$

Here $\mathbf{T}_N = \begin{bmatrix} \mathbf{e}_1 & \cdots & \mathbf{e}_N \end{bmatrix}$ and $\mathbf{e}_k$ is the k-th eigenvector of the forward shift matrix $\mathbf{A}_N$ corresponding to the k-th modal eigenvalue $\mathrm{e}^{\mathrm{i}\frac{2\pi(k-1)}{N}}$, where $\mathrm{i}^2 = -1$, $k = 1, \dots, N$, and $\mathbf{I}_M$ is the M-dimensional identity matrix. This transformation is also known as the discrete Fourier transformation; see [59].

Notice that the mode number $k = 1$ corresponds to a translational symmetry of the system, the mode numbers $k = 2, \dots, \lfloor \frac{N}{2} + 1 \rfloor$ correspond to having $k-1$ waves along the ring, while the mode numbers $k = \lceil \frac{N}{2} + 1 \rceil, \dots, N$ correspond to having $N - k + 2$ waves along the ring; see [26, 59]. Note that by abuse of notation we use mode numbers $k = 1, \dots, N$, in this chapter as opposed to $k = 0, \dots, N-1$, in Chapter 4. Applying the modal transformation (5.15) the equation $\dot{\hat{\mathbf{y}}} = \hat{\mathbf{J}}_0 \hat{\mathbf{y}}$ (cf. (5.9,5.10)) without perturbations can be rewritten as

$$\dot{\hat{\mathbf{z}}} = \hat{\mathbf{D}}_0 \hat{\mathbf{z}}, \tag{5.17}$$

where the block diagonal matrix $\hat{\mathbf{D}}_0 \in \mathbb{C}^{NM \times NM}$ is given by

$$\hat{\mathbf{D}}_0 = \hat{\mathbf{T}}_0^{-1} \hat{\mathbf{J}}_0 \hat{\mathbf{T}}_0 = \mathrm{diag}([\hat{\mathbf{D}}_0]_k^k). \tag{5.18}$$

In particular, the block

$$[\hat{\mathbf{D}}_0]_k^k = \sum_{j=1}^{N} \mathbf{C}_j \mathrm{e}^{\mathrm{i}\frac{2\pi}{N}(k-1)(j-1)} \tag{5.19}$$

gives the dynamics of the k-th mode of the cyclic system. We note that the mode/block-eigenvector relationships for mode k can be formulated as

$$(\hat{\mathbf{J}}_0 - \mathbf{I}_N \otimes [\hat{\mathbf{D}}_0]_k^k)[\hat{\mathbf{T}}_0]_k = 0, \tag{5.20}$$

and

$$[\hat{\mathbf{T}}_0^{-1}]^k(\hat{\mathbf{J}}_0 - \mathbf{I}_N \otimes [\hat{\mathbf{D}}_0]_k^k) = 0, \tag{5.21}$$

where $[\hat{\mathbf{T}}_0]_k$ is the so-called k-th "block eigenvector", that is the k-th set of M columns of $\hat{\mathbf{T}}_0$ and $[\hat{\mathbf{T}}_0^{-1}]^k$ is the so-called k-th "left block eigenvector", that is the k-th set of M rows of $\hat{\mathbf{T}}_0^{-1}$. Formulae (5.20) and (5.21) will be used extensively to obtain approximations of modes and block-eigenvectors for the perturbed system in the next subsection.

Note that the linear coordinate transformation simplifies the linear analysis of the system: the linear part is decoupled into N sets of complex differential equations representing the oscillation modes. Thus, the linear stability can be analyzed separately for each mode and the stability of the synchronous state (5.5) is ensured when all modes are stable.

5.2.2 Modal analysis of cyclic systems with acyclic perturbations

In this section we build upon the analysis of the cyclic system to obtain an approximation for the modes of the mistuned cyclic system (5.9,5.10) when $\varepsilon_{i_1\sigma_1} > 0$ are small for all $i_1 = 1,\ldots,N$, $\sigma_1 = 0,\ldots,\sigma_{\max}$.

We assume that $\hat{\mathbf{J}}$ can be transformed to a block-diagonal matrix $\hat{\mathbf{D}}$ using the transformation

$$\hat{\mathbf{z}} = \hat{\mathbf{T}}\hat{\mathbf{y}}, \tag{5.22}$$

yielding

$$\dot{\mathbf{z}} = \hat{\mathbf{D}}\mathbf{z}, \tag{5.23}$$

with

$$\hat{\mathbf{D}} = \hat{\mathbf{T}}^{-1}\hat{\mathbf{J}}\hat{\mathbf{T}} = \mathrm{diag}([\hat{\mathbf{D}}]_k^k). \tag{5.24}$$

Indeed $[\hat{\mathbf{D}}]_k^k$ (k-th modal block) and $\left[\hat{\mathbf{T}}\right]_k$ (the k-th block-eigenvector) satisfy the equation

$$(\hat{\mathbf{J}} - \mathbf{I}_N \otimes [\hat{\mathbf{D}}]_k^k)\left[\hat{\mathbf{T}}\right]_k = 0, \tag{5.25}$$

cf. (5.20).

We construct $\hat{\mathbf{D}}$ as an expansion about $\hat{\mathbf{D}}_0$ up to third-order in $\varepsilon_{i\sigma}$:

$$\begin{aligned}\hat{\mathbf{D}} = \hat{\mathbf{D}}_0 &+ \sum_{i_1=1}^{N}\sum_{\sigma_1=0}^{\sigma_{\max}} \hat{\mathbf{D}}^{(1)}\,\varepsilon_{i_1\sigma_1} + \frac{1}{2}\sum_{i_1,i_2=1}^{N}\sum_{\sigma_1,\sigma_2=0}^{\sigma_{\max}} \hat{\mathbf{D}}^{(1,2)}\,\varepsilon_{i_1\sigma_1}\varepsilon_{i_2\sigma_2} \\ &+ \frac{1}{6}\sum_{i_1,i_2,i_3=1}^{N}\sum_{\sigma_1,\sigma_2,\sigma_3=0}^{\sigma_{\max}} \hat{\mathbf{D}}^{(1,2,3)}\,\varepsilon_{i_1\sigma_1}\varepsilon_{i_2\sigma_2}\varepsilon_{i_3\sigma_3} + \ldots,\end{aligned} \tag{5.26}$$

where we introduced the compact notation

$$\begin{aligned}\mathbf{M}^{(1)} &= \mathbf{M}_1(i_1,\sigma_1),\\ \mathbf{M}^{(1,2)} &= \mathbf{M}_2(i_1,\sigma_1,i_2,\sigma_2),\\ \mathbf{M}^{(1,2,3)} &= \mathbf{M}_3(i_1,\sigma_1,i_2,\sigma_2,i_3,\sigma_3).\end{aligned} \tag{5.27}$$

In order to be able to derive the coefficient matrices in (5.26) we expand $\hat{\mathbf{T}}$ up to second-order

$$\hat{\mathbf{T}} = \hat{\mathbf{T}}_0 + \sum_{i_1=1}^{N}\sum_{\sigma_1=0}^{\sigma_{\max}} \hat{\mathbf{T}}^{(1)}\,\varepsilon_{i_1\sigma_1} + \frac{1}{2}\sum_{i_1,i_2=1}^{N}\sum_{\sigma_1,\sigma_2=0}^{\sigma_{\max}} \hat{\mathbf{T}}^{(1,2)}\,\varepsilon_{i_1\sigma_1}\varepsilon_{i_2\sigma_2} + \ldots. \tag{5.28}$$

Since we already know $\hat{\mathbf{D}}_0$ and $\hat{\mathbf{T}}_0$ from (5.18,5.19) and (5.16), respectively, we use (5.25) and (5.24) sequentially to obtain the higher order terms of $\hat{\mathbf{D}}$ and $\hat{\mathbf{T}}$ as depicted in Fig. 5.2.

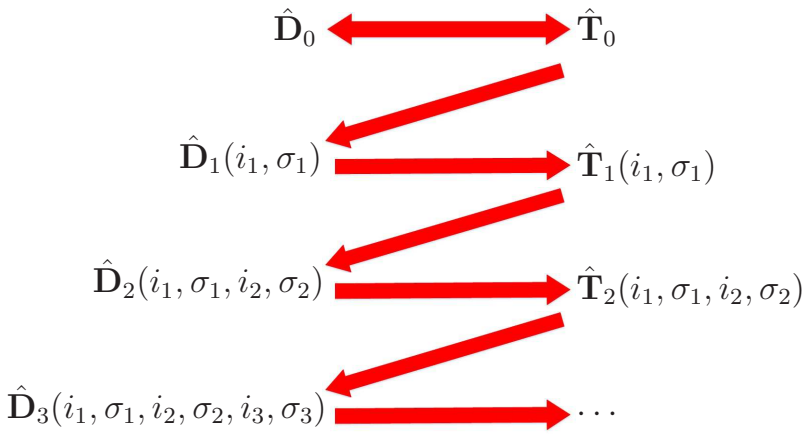

Figure 5.2: Diagram showing the sequential method of obtaining the approximations for the modal blocks and block-eigenvectors of the perturbed system by solving (5.25) and (5.24).

In particular, to determine the higher order terms in $[\hat{\mathbf{D}}]_k^k$ we differentiate (5.25) with respect to $\varepsilon_{i\sigma}$, while to obtain the higher order terms of $[\hat{\mathbf{T}}]_k$ we compare the left and right hand sides of (5.24). To obtain the first-order perturbation of the dynamics of the k-th

mode $[\hat{\mathbf{D}}^{(1)}]_k^k$ for an arbitrary i_1, σ_1 we take the derivative of (5.25) with respect to $\varepsilon_{i_1\sigma_1}$ pair (denoted by ∂_{ε_1}) to obtain

$$\Big(\partial_{\varepsilon_1}\hat{\mathbf{J}} - \mathbf{I}_N \otimes \partial_{\varepsilon_1}[\hat{\mathbf{D}}]_k^k\Big)[\hat{\mathbf{T}}]_k + \Big(\hat{\mathbf{J}} - \mathbf{I}_N \otimes [\hat{\mathbf{D}}]_k^k\Big)\partial_{\varepsilon_1}[\hat{\mathbf{T}}]_k = 0. \tag{5.29}$$

We then evaluate this at $\varepsilon_{i_1\sigma_1} = 0$, yielding

$$\big(\hat{\mathbf{P}}^{(1)} - \mathbf{I}_N \otimes [\hat{\mathbf{D}}^{(1)}]_k^k\big)[\hat{\mathbf{T}}_0]_k + \big(\hat{\mathbf{J}}_0 - \mathbf{I}_N \otimes [\hat{\mathbf{D}}_0]_k^k\big)[\hat{\mathbf{T}}^{(1)}]_k = 0, \tag{5.30}$$

where we use the compact notation $\mathbf{M}^{(1)} = \mathbf{M}(i_1, \sigma_1)$; cf. (5.27) and see (5.10,5.11,5.12). Multiplying (5.30) with $[\hat{\mathbf{T}}_0^{-1}]^k$ from the left and using (5.21) we can eliminate the second term, that is,

$$[\hat{\mathbf{T}}_0^{-1}]^k\big(\hat{\mathbf{P}}^{(1)} - \mathbf{I}_N \otimes [\hat{\mathbf{D}}^{(1)}]_k^k\big)[\hat{\mathbf{T}}_0]_k = 0, \tag{5.31}$$

which can be simplified and solved for

$$[\hat{\mathbf{D}}^{(1)}]_k^k = [\hat{\mathbf{T}}_0^{-1}]^k\, \hat{\mathbf{P}}^{(1)}[\hat{\mathbf{T}}_0]_k, \tag{5.32}$$

We can substitute the definition (5.12) of $\hat{\mathbf{P}}^{(1)}$ to obtain a general expression for the first-order perturbation of the k mode due to a link between nodes i_1 and $i_1 + \sigma_1$:

$$[\hat{\mathbf{D}}^{(1)}]_k^k = [\hat{\mathbf{D}}_1(i_1, \sigma_1)]_k^k = \frac{1}{N}\Big(\partial_1 \mathbf{h}_{i_1\sigma_1} + \mathrm{e}^{\mathrm{i}\frac{2\pi}{N}\sigma_1(k-1)}\partial_2 \mathbf{h}_{i_1\sigma_1}\Big). \tag{5.33}$$

To expand the modal dynamics up to second-order in terms of mistunings we must first obtain the expansion of matrix $\hat{\mathbf{T}}$ and its block-eigenvectors up to first-order. Notice that the expansion for $\hat{\mathbf{T}}^{-1}$ can be written as

$$\begin{aligned}\hat{\mathbf{T}}^{-1} \approx \hat{\mathbf{T}}_0^{-1} &- \sum_{i_1=1}^{N}\sum_{\sigma_1=0}^{\sigma_{\max}} \hat{\mathbf{T}}_0^{-1}\hat{\mathbf{T}}^{(1)}\hat{\mathbf{T}}_0^{-1}\varepsilon_{i_1\sigma_1} \\ &+ \sum_{i_1,i_2=1}^{N}\sum_{\sigma_1,\sigma_2=0}^{\sigma_{\max}} \Big(\hat{\mathbf{T}}_0^{-1}\hat{\mathbf{T}}^{(1)}\hat{\mathbf{T}}_0^{-1}\hat{\mathbf{T}}^{(2)}\hat{\mathbf{T}}_0^{-1} - \frac{1}{2}\hat{\mathbf{T}}_0^{-1}\hat{\mathbf{T}}^{(1,2)}\hat{\mathbf{T}}_0^{-1}\Big)\varepsilon_{i_1\sigma_1}\varepsilon_{i_2\sigma_2} + \ldots,\end{aligned} \tag{5.34}$$

where we exploited the Neumann series, given by

$$(\mathbf{I} + \mathbf{M})^{-1} \approx \mathbf{I} - \mathbf{M} + \mathbf{M}^2 + \ldots, \tag{5.35}$$

where $\mathbf{M}$ is a square matrix whose eigenvalues are less than 1 and $\mathbf{I}$ is an identity matrix. Substituting (5.26), (5.28), and (5.34) into (5.24) and matching the first-order terms in $\varepsilon_{i_1\sigma_1}$

yields

$$\sum_{i_1=1}^{N}\sum_{\sigma_1=0}^{\sigma_{\max}}\hat{\mathbf{D}}^{(1)}\varepsilon_{i_1\sigma_1}=\sum_{i_1=1}^{N}\sum_{\sigma_1=0}^{\sigma_{\max}}\Big(-\hat{\mathbf{T}}_0^{-1}\hat{\mathbf{T}}^{(1)}\hat{\mathbf{T}}_0^{-1}\hat{\mathbf{J}}_0\hat{\mathbf{T}}_0+\hat{\mathbf{T}}_0^{-1}\hat{\mathbf{P}}^{(1)}\hat{\mathbf{T}}_0+\hat{\mathbf{T}}_0^{-1}\hat{\mathbf{J}}_0\hat{\mathbf{T}}^{(1)}\Big)\varepsilon_{i_1\sigma_1}. \tag{5.36}$$

We equate the terms corresponding to a perturbation corresponding to an arbitrary i_1, σ_1 pair and use (5.18) to simplify the formula to obtain a Sylvester equation

$$\hat{\mathbf{D}}_0\hat{\mathbf{U}}^{(1)}-\hat{\mathbf{U}}^{(1)}\hat{\mathbf{D}}_0=\hat{\mathbf{D}}^{(1)}-\hat{\mathbf{T}}_0^{-1}\hat{\mathbf{P}}^{(1)}\hat{\mathbf{T}}_0, \tag{5.37}$$

for the matrix $\hat{\mathbf{U}}^{(1)}=\hat{\mathbf{T}}_0^{-1}\hat{\mathbf{T}}^{(1)}$ of $(MN)^2$ unknowns.

The complexity of (5.37) can be reduced significantly by exploiting the cyclic structure of the unperturbed system. In (5.37), $\hat{\mathbf{U}}^{(1)}$ is multiplied by block-diagonal matrices from the left and right. Thus, the coefficients contained by $[\hat{\mathbf{U}}^{(1)}]_\ell^k$ remain in the k-th block row and ℓ-th block column after the multiplications, which yields

$$[\hat{\mathbf{D}}_0]_k^k[\hat{\mathbf{U}}^{(1)}]_\ell^k-[\hat{\mathbf{U}}^{(1)}]_\ell^k[\hat{\mathbf{D}}_0]_\ell^\ell=[\hat{\mathbf{D}}^{(1)}]_\ell^k-[\hat{\mathbf{T}}_0^{-1}]^k\,\hat{\mathbf{P}}^{(1)}[\hat{\mathbf{T}}_0]_\ell. \tag{5.38}$$

Using (5.12) and (5.33), this can be written as

$$[\hat{\mathbf{D}}_0]_k^k[\hat{\mathbf{U}}^{(1)}]_\ell^k-[\hat{\mathbf{U}}^{(1)}]_\ell^k[\hat{\mathbf{D}}_0]_\ell^\ell=\frac{1}{N}\mathrm{e}^{\mathrm{i}\frac{2\pi}{N}(i_1-1)(\ell-k)}\Big(\partial_1\mathbf{h}_{i_1\sigma_1}+\mathrm{e}^{\mathrm{i}\frac{2\pi}{N}\sigma_1(\ell-1)}\partial_2\mathbf{h}_{i_1\sigma_1}\Big)(\delta_{k\ell}-1), \tag{5.39}$$

where $\delta_{k\ell}$ denotes the Kronecker delta. This Sylvester equation can be rewritten into the standard form of a linear algebraic equation

$$\mathbf{A}_{k\,\ell}^{(1)}\mathbf{b}_{k\,\ell}^{(1)}=\mathbf{c}_{k\,\ell}^{(1)}, \tag{5.40}$$

where

$$\mathbf{A}_{k\,\ell}^{(1)}=\mathbf{I}_M\otimes[\hat{\mathbf{D}}_0]_k^k-[\hat{\mathbf{D}}_0^{\mathrm{T}}]_\ell^\ell\otimes\mathbf{I}_M, \tag{5.41}$$

and

$$\mathbf{b}_{k\,\ell}^{(1)}=\mathrm{vec}([\hat{\mathbf{U}}^{(1)}]_\ell^k). \tag{5.42}$$

Here $\mathrm{vec}(\cdot)$ is the vectorization operator that stacks the columns of a matrix into a column vector. Similarly, $\mathbf{c}_{k\,\ell}^{(1)}$ is the vectorization of the right hand side of (5.39). Thus, by exploiting the cyclic structure of the unperturbed system (5.13) we need to solve N^2 decoupled linear equations each with M^2 unknowns. In contrast (5.37) would require us to solve $(MN)^2$ coupled equations. For the diagonal $M\times M$ blocks of $\hat{\mathbf{U}}^{(1)}$, equation (5.40) has multiple

possible solutions due to a non-zero nullity. Here we set

$$[\hat{\mathbf{U}}^{(1)}]_k^k = \mathbf{0}. \tag{5.43}$$

Once all the $M \times M$ blocks of $\hat{\mathbf{U}}^{(1)}$ are solved for, we can calculate $\hat{\mathbf{T}}^{(1)} = \hat{\mathbf{T}}_0 \hat{\mathbf{U}}^{(1)}$.

To obtain the second-order perturbation of the dynamics of the k-th mode $[\hat{\mathbf{D}}^{(1,2)}]_k^k$ for an arbitrary $i_1, \sigma_1, i_2, \sigma_2$ quadruple we take the derivative of (5.29) with respect to $\varepsilon_{i_2\sigma_2}$ (denoted by ∂_{ε_2}) yielding

$$\begin{aligned}
&\Big(\partial_{\varepsilon_1}\partial_{\varepsilon_2}\hat{\mathbf{J}} - \mathbf{I}_N \otimes \partial_{\varepsilon_1}\partial_{\varepsilon_2}[\hat{\mathbf{D}}]_k^k\Big)[\hat{\mathbf{T}}]_k + \Big(\partial_{\varepsilon_1}\hat{\mathbf{J}} - \mathbf{I}_N \otimes \partial_{\varepsilon_1}[\hat{\mathbf{D}}]_k^k\Big)\partial_{\varepsilon_2}[\hat{\mathbf{T}}]_k \\
&+ \Big(\partial_{\varepsilon_2}\hat{\mathbf{J}} - \mathbf{I}_N \otimes \partial_{\varepsilon_2}[\hat{\mathbf{D}}]_k^k\Big)\partial_{\varepsilon_1}[\hat{\mathbf{T}}]_k + \Big(\hat{\mathbf{J}} - \mathbf{I}_N \otimes [\hat{\mathbf{D}}]_k^k\Big)\partial_{\varepsilon_1}\partial_{\varepsilon_2}[\hat{\mathbf{T}}]_k = 0,
\end{aligned} \tag{5.44}$$

and evaluate this at $\varepsilon_{i_1\sigma_1} = 0$, $\varepsilon_{i_2\sigma_2} = 0$ to get

$$\begin{aligned}
&\frac{1}{2}\mathbf{I}_N \otimes ([\hat{\mathbf{D}}^{(1,2)}]_k^k + [\hat{\mathbf{D}}^{(2,1)}]_k^k)[\hat{\mathbf{T}}_0]_k = \\
&\big(\hat{\mathbf{P}}^{(1)} - \mathbf{I}_N \otimes [\hat{\mathbf{D}}^{(1)}]_k^k\big)[\hat{\mathbf{T}}^{(2)}]_k + \big(\hat{\mathbf{P}}^{(2)} - \mathbf{I}_N \otimes [\hat{\mathbf{D}}^{(2)}]_k^k\big)[\hat{\mathbf{T}}^{(1)}]_k \\
&+ \frac{1}{2}\big(\hat{\mathbf{J}}_0 - \mathbf{I}_N \otimes [\hat{\mathbf{D}}_0]_k^k\big)\big([\hat{\mathbf{T}}^{(1,2)}]_k + [\hat{\mathbf{T}}^{(2,1)}]_k\big),
\end{aligned} \tag{5.45}$$

where we used the compact notation $\mathbf{M}^{(1,2)} = \mathbf{M}_2(i_1, \sigma_1, i_2, \sigma_2)$, cf. (5.27) and see (5.10,5.11,5.12). We eliminate the last term in the expression above by multiplying by $[\hat{\mathbf{T}}_0^{-1}]^k$ from the left and use (5.21) to obtain

$$\begin{aligned}
&[\hat{\mathbf{D}}^{(1,2)}]_k^k + [\hat{\mathbf{D}}^{(2,1)}]_k^k = \\
&2[\hat{\mathbf{T}}_0^{-1}]^k\big(\hat{\mathbf{P}}^{(1)} - \mathbf{I}_N \otimes [\hat{\mathbf{D}}^{(1)}]_k^k\big)[\hat{\mathbf{T}}^{(2)}]_k + 2[\hat{\mathbf{T}}_0^{-1}]^k\big(\hat{\mathbf{P}}^{(2)} - \mathbf{I}_N \otimes [\hat{\mathbf{D}}^{(2)}]_k^k\big)[\hat{\mathbf{T}}^{(1)}]_k.
\end{aligned} \tag{5.46}$$

Since the above expression contains two unknowns ($[\hat{\mathbf{D}}^{(1,2)}]_k^k$ and $[\hat{\mathbf{D}}^{(2,1)}]_k^k$) for each $i_1, \sigma_1, i_2, \sigma_2$ quadruple, we have the freedom to set

$$[\hat{\mathbf{D}}^{(1,2)}]_k^k = 2[\hat{\mathbf{T}}_0^{-1}]^k\big(\hat{\mathbf{P}}^{(1)} - \mathbf{I}_N \otimes [\hat{\mathbf{D}}^{(1)}]_k^k\big)[\hat{\mathbf{T}}^{(2)}]_k. \tag{5.47}$$

Since $[\hat{\mathbf{T}}_0^{-1}]^k(\mathbf{I}_N \otimes [\hat{\mathbf{D}}^{(1)}]_k^k)[\hat{\mathbf{T}}^{(2)}]_k = 0$ we obtain the simplified form

$$[\hat{\mathbf{D}}^{(1,2)}]_k^k = 2[\hat{\mathbf{T}}_0^{-1}]^k\hat{\mathbf{P}}^{(1)}[\hat{\mathbf{T}}^{(2)}]_k. \tag{5.48}$$

Using (5.12) this can be written as

$$[\hat{\mathbf{D}}^{(1,2)}]_k^k = [\hat{\mathbf{D}}_2(i_1,\sigma_1,i_2,\sigma_2)]_k^k = \sum_{j=1}^{N} \frac{2}{N} \mathrm{e}^{\mathrm{i}\frac{2\pi}{N}(i_1-1)(j-k)} \big(\partial_1 \mathbf{h}_{i_1\sigma_1} + \mathrm{e}^{\mathrm{i}\frac{2\pi}{N}\sigma_1(j-1)} \partial_2 \mathbf{h}_{i_1\sigma_1}\big) [\hat{\mathbf{U}}^{(2)}]_k^j, \tag{5.49}$$

where the components of $\hat{\mathbf{U}}^{(2)} = \hat{\mathbf{U}}_1(i_2,\sigma_2) = \hat{\mathbf{T}}_0^{-1}\hat{\mathbf{T}}_1(i_2,\sigma_2)$ are given by the solution of (5.40).

To expand the modal dynamics up to third-order we must first obtain the expansion of matrix $\hat{\mathbf{T}}$ up to second-order. The process is similar to the process of expanding $\hat{\mathbf{T}}$ up to first-order; cf. (5.36-5.43). Substituting (5.26), (5.28), and (5.34) into (5.24) and collecting the second-order terms yields

$$\begin{aligned}\frac{1}{2}\sum_{i_1,i_2=1}^{N}\sum_{\sigma_1,\sigma_2=0}^{\sigma_{\max}} \hat{\mathbf{D}}^{(1,2)} \varepsilon_{i_1\sigma_1}\varepsilon_{i_2\sigma_2} = \sum_{i_1,i_2=1}^{N}\sum_{\sigma_1,\sigma_2=0}^{\sigma_{\max}} \Big(&-\frac{1}{2}\hat{\mathbf{T}}_0^{-1}\hat{\mathbf{T}}^{(1,2)}\hat{\mathbf{T}}_0^{-1}\hat{\mathbf{J}}_0\hat{\mathbf{T}}_0 \\ &+ \hat{\mathbf{T}}_0^{-1}\hat{\mathbf{T}}^{(1)}\hat{\mathbf{T}}_0^{-1}\hat{\mathbf{T}}^{(2)}\hat{\mathbf{T}}_0^{-1}\hat{\mathbf{J}}_0\hat{\mathbf{T}}_0 - \hat{\mathbf{T}}_0^{-1}\hat{\mathbf{T}}^{(1)}\hat{\mathbf{T}}_0^{-1}\hat{\mathbf{P}}^{(2)}\hat{\mathbf{T}}_0 \\ &- \hat{\mathbf{T}}_0^{-1}\hat{\mathbf{T}}^{(1)}\hat{\mathbf{T}}_0^{-1}\hat{\mathbf{J}}_0\hat{\mathbf{T}}^{(2)} + \hat{\mathbf{T}}_0^{-1}\hat{\mathbf{P}}^{(1)}\hat{\mathbf{T}}^{(2)} + \frac{1}{2}\hat{\mathbf{T}}_0^{-1}\hat{\mathbf{J}}_0\hat{\mathbf{T}}^{(1,2)}\Big)\varepsilon_{i_1\sigma_1}\varepsilon_{i_2\sigma_2}.\end{aligned} \tag{5.50}$$

Equating the terms corresponding to $\varepsilon_{i_1\sigma_1}\varepsilon_{i_2\sigma_2}$, and using (5.18) and (5.37) and some algebraic manipulation we obtain the Sylvester equation

$$\hat{\mathbf{D}}_0\hat{\mathbf{U}}^{(1,2)} - \hat{\mathbf{U}}^{(1,2)}\hat{\mathbf{D}}_0 = \hat{\mathbf{D}}^{(1,2)} + 2\hat{\mathbf{U}}^{(1)}\hat{\mathbf{D}}^{(2)} - 2\hat{\mathbf{T}}_0^{-1}\hat{\mathbf{P}}^{(1)}\hat{\mathbf{T}}_0\hat{\mathbf{U}}^{(2)}, \tag{5.51}$$

for the matrix $\hat{\mathbf{U}}^{(1,2)} = \hat{\mathbf{T}}_0^{-1}\hat{\mathbf{T}}^{(1,2)}$.

We again compare individual blocks on the two sides of (5.51) and reduce it to a low order Sylvester equation

$$[\hat{\mathbf{D}}_0]_k^k[\hat{\mathbf{U}}^{(1,2)}]_\ell^k - [\hat{\mathbf{U}}^{(1,2)}]_\ell^k[\hat{\mathbf{D}}_0]_\ell^\ell = [\hat{\mathbf{D}}^{(1,2)}]_\ell^k + 2[\hat{\mathbf{U}}^{(1)}]_\ell^k[\hat{\mathbf{D}}^{(2)}]_\ell^\ell - 2[\hat{\mathbf{T}}_0^{-1}]^k\hat{\mathbf{P}}^{(1)}\hat{\mathbf{T}}_0[\hat{\mathbf{U}}^{(2)}]_\ell. \tag{5.52}$$

Using (5.33) this becomes

$$\begin{aligned}[\hat{\mathbf{D}}_0]_k^k[\hat{\mathbf{U}}^{(1,2)}]_\ell^k - [\hat{\mathbf{U}}^{(1,2)}]_\ell^k[\hat{\mathbf{D}}_0]_\ell^\ell &= \frac{2}{N}[\hat{\mathbf{U}}^{(1)}]_\ell^k(\partial_1\mathbf{h}_{i_2\sigma_2} + \mathbf{e}^{\mathrm{i}\frac{2\pi}{N}\sigma_2(\ell-1)}\partial_2\mathbf{h}_{i_2\sigma_2}) \\ -\sum_{j=1}^{N}\frac{2}{N}\mathrm{e}^{\mathrm{i}\frac{2\pi}{N}(i_1-1)(j-k)}&\Big(\partial_1\mathbf{h}_{i_1\sigma_1} + \mathrm{e}^{\mathrm{i}\frac{2\pi}{N}\sigma_1(j-1)}\partial_2\mathbf{h}_{i_1\sigma_1}\Big)[\hat{\mathbf{U}}^{(2)}]_\ell^j(1-\delta_{k\ell}).\end{aligned} \tag{5.53}$$

that can be written into the form of a linear algebraic equation

$$\mathbf{A}_{k\,\ell}^{(1,2)}\ \mathbf{b}_{k\,\ell}^{(1,2)} = \mathbf{c}_{k\,\ell}^{(1,2)}, \tag{5.54}$$

where

$$\mathbf{A}^{(1,2)}_{k\,\ell} = \mathbf{I}_M \otimes [\hat{\mathbf{D}}_0]^k_k - [\hat{\mathbf{D}}_0^{\mathrm{T}}]^\ell_\ell \otimes \mathbf{I}_M, \tag{5.55}$$

and

$$\mathbf{b}^{(1,2)}_{k\,\ell} = \mathrm{vec}\big([\hat{\mathbf{U}}^{(1,2)}]^k_\ell\big), \tag{5.56}$$

and $\mathbf{c}^{(1,2)}_{k\ell}$ is the vectorization of the right hand side of (5.53); cf. (5.40, 5.41, 5.42). Here again we need to solve N^2 decoupled equations equations with M^2 unknowns. In contrast in (5.52) would require us to solve $(NM)^2$ coupled equations.

The third-order perturbation for the dynamics of the k-th mode can then be obtained similarly to the way the first and second-order perturbations were obtained. The detailed derivation is given in Appendix H. The result can be simplified to

$$[\hat{\mathbf{D}}^{(1,2,3)}]^k_k = [\hat{\mathbf{D}}_3(i_1,\sigma_1,i_2,\sigma_2,i_3,\sigma_3)]^k_k = \frac{3}{N}\sum_{j=1}^{N} \mathrm{e}^{\mathrm{i}\frac{2\pi}{N}(i_1-1)(j-k)}\big(\partial_1\mathbf{h}_{i_1\sigma_1} + \mathrm{e}^{\mathrm{i}\frac{2\pi}{N}\sigma_1(j-1)}\partial_2\mathbf{h}_{i_1\sigma_1}\big)[\hat{\mathbf{U}}^{(2,3)}]^j_k, \tag{5.57}$$

where the compact notation $\mathbf{M}^{(1,2,3)} = \mathbf{M}(i_1,\sigma_1,i_2,\sigma_2,i_3,\sigma_3)$ was used (cf. (5.27)). Using (5.13), (5.33), (5.49), and (5.57) the dynamics of the k-th mode can be expressed by

$$\dot{\mathbf{z}}_k = [\hat{\mathbf{D}}]^k_k \mathbf{z}_k, \tag{5.58}$$

where

$$\begin{aligned}
[\hat{\mathbf{D}}]^k_k = &\sum_{j=1}^{N} \mathbf{C}_j \mathrm{e}^{\mathrm{i}\frac{2\pi}{N}(k-1)(j-1)} + \frac{1}{N}\sum_{i_1=1}^{N}\sum_{\sigma_1=0}^{\sigma_{\max}}\Big(\partial_1\mathbf{h}_{i_1\sigma_1} + \mathrm{e}^{\mathrm{i}\frac{2\pi}{N}\sigma_1(k-1)}\partial_2\mathbf{h}_{i_1\sigma_1}\Big)\varepsilon_{i_1\sigma_1} \\
&+ \frac{1}{N}\sum_{i_1,i_2=1}^{N}\sum_{\sigma_1,\sigma_2=0}^{\sigma_{\max}}\sum_{j=1}^{N} \mathrm{e}^{\mathrm{i}\frac{2\pi}{N}(i_1-1)(j-k)}\big(\partial_1\mathbf{h}_{i_1\sigma_1} + \mathrm{e}^{\mathrm{i}\frac{2\pi}{N}\sigma_1(j-1)}\partial_2\mathbf{h}_{i_1\sigma_1}\big)[\hat{\mathbf{U}}^{(2)}]^j_k \varepsilon_{i_1\sigma_1}\varepsilon_{i_2\sigma_2} \\
&+ \frac{1}{2N}\sum_{i_1,i_2,i_3=1}^{N}\sum_{\sigma_1,\sigma_2,\sigma_3=0}^{\sigma_{\max}}\sum_{j=1}^{N} \mathrm{e}^{\mathrm{i}\frac{2\pi}{N}(i_1-1)(j-k)}\big(\partial_1\mathbf{h}_{i_1\sigma_1} + \mathrm{e}^{\mathrm{i}\frac{2\pi}{N}\sigma_1(j-1)}\partial_2\mathbf{h}_{i_1\sigma_1}\big)[\hat{\mathbf{U}}^{(2,3)}]^j_k \varepsilon_{i_1\sigma_1}\varepsilon_{i_2\sigma_2}\varepsilon_{i_3\sigma_3},
\end{aligned} \tag{5.59}$$

and $[\hat{\mathbf{U}}^{(2)}]$ and $[\hat{\mathbf{U}}^{(2,3)}]$ are the solutions of (5.37) and (5.51), respectively.

That is we obtained N decoupled systems of M linear complex ordinary differential equations. Each system can then be separately analyzed to estimate the stability of the corresponding mode (assuming that the perturbations are small). To evaluate the linear stability of the synchronous state (5.5) we calculate the characteristic polynomial for mode

k, given by

$$\det(\lambda \mathbf{I}_M - [\hat{\mathbf{D}}]_k^k) = 0, \tag{5.60}$$

and solve for its M eigenvalues $\lambda \in \mathbb{C}$. Indeed, the synchronous solution is stable when all modes are stable.

5.3 Modal approximation for heterogeneous connected vehicle network

In this section we analyze the connected vehicle network where the human-driven vehicles are governed by (4.1) and the connected automated vehicles are governed by (5.1) using the framework developed above. First, we decompose the underlying cyclic system with nearest neighbor coupling and analyze the linear stability of the corresponding modes. Then, we use the developed perturbation analysis to approximate the modes in the presence of long-range links. Decoupling the modes of the connected vehicle network allows us to analyze the linear stability of the modes individually, and characterize the oscillations that arise when these modes lose their stability. This allows us to study the effects of long-range V2V links on the stability of connected vehicle networks.

Consider the Taylor approximation (4.3) up to first order, in other words, setting $p = q = 0$. Using the vector notation $\mathbf{y}_i = \operatorname{col}[\widetilde{s}_i \;\; \widetilde{v}_i]$, we can rewrite the dynamics of the i-th car (4.3) around the uniform flow as

$$\dot{\mathbf{y}}_i = \mathbf{C}_0 \mathbf{y}_i + \mathbf{C}_1 \mathbf{y}_{i+1} + \sum_{\sigma=2}^{\sigma_{\max}} (\partial_1 \mathbf{h}_{i\sigma} \mathbf{y}_i + \partial_2 \mathbf{h}_{i\sigma} \mathbf{y}_{i+\sigma}) \beta_{i\sigma}\,, \tag{5.61}$$

(cf. 5.7). Here

$$\mathbf{C}_0 = \begin{bmatrix} 0 & 1 \\ -p & -\alpha - \beta_1 \end{bmatrix}, \quad \mathbf{C}_1 = \begin{bmatrix} 0 & 0 \\ p & \beta_1 \end{bmatrix}, \tag{5.62}$$

represent the nearest neighbor coupling,

$$\partial_1 \mathbf{h}_{i\sigma} = \begin{bmatrix} 0 & 0 \\ 0 & -1 \end{bmatrix}, \quad \partial_2 \mathbf{h}_{i\sigma} = \begin{bmatrix} 0 & 0 \\ 0 & 1 \end{bmatrix}, \tag{5.63}$$

correspond to the long-range connections, cf. (5.8) and $\beta_{i\sigma}$ stands for $\varepsilon_{i\sigma}$. Then we write (5.61) into the form (5.9,5.10) where

$$\hat{\mathbf{J}}_0 = \operatorname{circ}(\mathbf{C}_0, \mathbf{C}_1, \mathbf{0}, \ldots, \mathbf{0}) = (\mathbf{I}_N \otimes \mathbf{C}_0 + \mathbf{A}_N \otimes \mathbf{C}_1), \tag{5.64}$$

(cf. (5.11,5.13)) and $\hat{\mathbf{P}}(i_1, \sigma_1)$ is defined in (5.12).

5.3.1 Modal analysis of connected vehicle network with nearest neighbor coupling

Prior to performing the linear modal analysis on the heterogeneous connected vehicle network, we first find the modes for the homogenous network, i.e., (5.61) with $\beta_{i\sigma} = 0$. This analysis was performed in detail in [8] and here we summarize the main findings. Performing the coordinate transformation (5.15) we obtain the dynamics of the k-th mode to be

$$[\hat{\mathbf{D}}_0]_k^k = \begin{bmatrix} 0 & 1 \\ p\,\eta_{k1} & \beta_1 \eta_{k1} - \alpha \end{bmatrix}, \tag{5.65}$$

(cf. (5.19)) where

$$\eta_{k\ell} = \mathrm{e}^{\mathrm{i}\frac{2\pi}{N}(k-1)} - \mathrm{e}^{\mathrm{i}\frac{2\pi}{N}(\ell-1)}, \tag{5.66}$$

for $k, \ell = 1, \ldots, N$. Note that the dynamics of modes k and $N-k+2$ are complex conjugates of each other. Mode $k = 1$ corresponds to a translational symmetry of the system, see [65]. This mode does not become unstable for $\alpha > 0$. We also remark that for even N, there is another special mode $k = N/2+1$ which does not have a complex conjugate mode. This mode remains stable for $\alpha + 2\beta_1 > 0$.

Modes k and $N-k+2$ lose stability at a critical value of $p = \alpha V'(h^*)$ given by

$$p_k = \tfrac{1}{2}(2\beta_1 + \alpha)\Big((2\beta_1 + \alpha)\tan^2\Big(\tfrac{(k-1)\pi}{N}\Big) + \alpha\Big), \tag{5.67}$$

and the stability of these modes is lost to oscillations of frequencies

$$\omega_k = (2\beta_1 + \alpha)\tan\Big(\tfrac{(k-1)\pi}{N}\Big), \tag{5.68}$$

for $k = 2, \ldots, N$. Since (5.67) is monotonically increasing with k when $2 \le k \le \lfloor \frac{N}{2} + 1 \rfloor$, the modes lose stability in the increasing order of mode number k. Thus, the uniform flow loses stability when modes 2 (and N) lose stability for the cyclically symmetric system with nearest neighbor coupling. At the linear level, the oscillations can be characterized by the modal coordinates $\mathbf{z}_k$ and $\mathbf{z}_{N+2-k}$. In order to perform a similar analysis for a connected vehicle network that includes long-range V2V links, we perform perturbation analysis to decouple the modes.

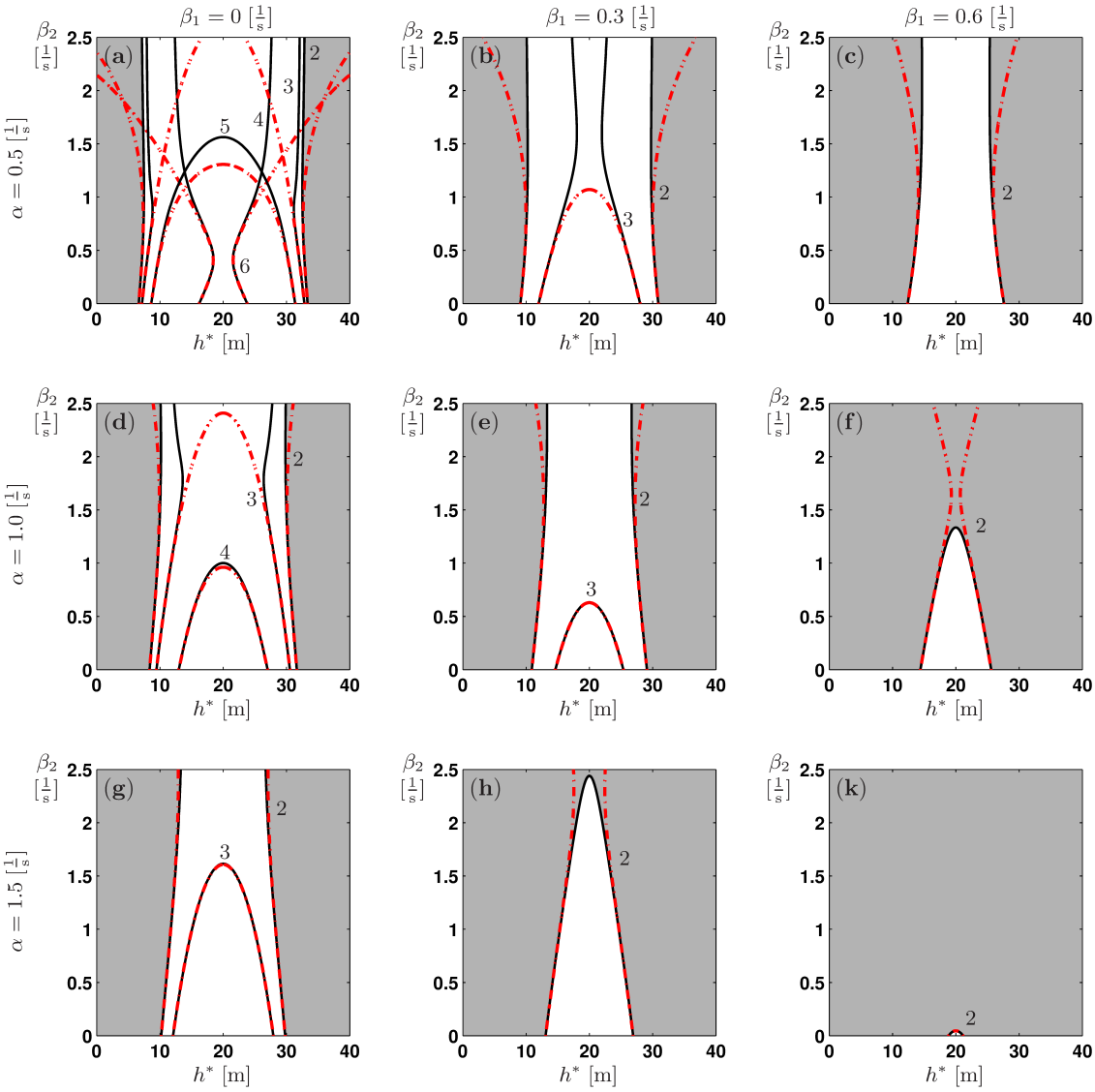

Figure 5.3: Stability charts in the (h^*, β_2) plane when a V2V link of length 2 is added to an 11-car network. The β_1 and α values are indicated at each panel. The red curves denote the stability boundaries for the modes $k = 2, \ldots, 6$ obtained through analytical approximation up to third-order in β_σ. The black curves denote the linear stability boundaries for modes obtained by numerical continuation. The grey shaded region corresponds to stable uniform flow.

5.3.2 Stability analysis of connected vehicle network with long-range V2V connections

Now we consider the case that $\beta_{i_1\sigma_1}$ are small for all $i_1 = 1, \ldots, N$ and $\sigma_1 = 2, \ldots, \sigma_{\max}$. Considering (5.61) and using (5.25) with the approximations defined in (5.26), (5.28), and

(5.34) we can obtain the perturbations to the modal dynamics and the modal transformation. We use (5.33) to obtain the first-order perturbation for the dynamics of the k-th mode associated with a link of length σ_1 terminated at vehicle i_1. This reads

$$[\hat{\mathbf{D}}_1(i_1,\sigma_1)]_k^k = \begin{bmatrix} 0 & 0 \\ 0 & \frac{1}{N}\left(\mathrm{e}^{\mathrm{i}\frac{2\pi}{N}\sigma_1(k-1)}-1\right) \end{bmatrix}. \tag{5.69}$$

We see that to first-order the contributions of the long-range links are independent from one another. In other words, to first-order, the contribution of all the links to the dynamics of mode k is the sum of the contributions of the individual links. To obtain the modal coordinate transformation (5.22) up to first-order we solve (5.40) with the matrices

$$\mathbf{A}_{k\ell}^{(1)} = \begin{bmatrix} 0 & 1 & -p\eta_{\ell 1} & 0 \\ p\eta_{k1} & \beta_1\eta_{k1}-\alpha & 0 & -p\eta_{\ell 1} \\ -1 & 0 & -\beta_1\eta_{\ell 1}+\alpha & 1 \\ 0 & -1 & p\eta_{k1} & \beta_1\eta_{k\ell} \end{bmatrix}, \tag{5.70}$$

and

$$\mathbf{c}_{k\ell}^{(1)} = \begin{bmatrix} 0 \\ 0 \\ 0 \\ \frac{1}{N}\mathrm{e}^{\mathrm{i}\frac{2\pi}{N}(i_1-1)(\ell-k)}\left(\mathrm{e}^{\mathrm{i}\frac{2\pi}{N}\sigma_1(\ell-1)}-1\right)(\delta_{k\ell}-1) \end{bmatrix}, \tag{5.71}$$

to obtain

$$\mathbf{b}_{k\ell}^{(1)} = \begin{bmatrix} u_{k\ell,11}^{(1)} \\ u_{k\ell,21}^{(1)} \\ u_{k\ell,12}^{(1)} \\ u_{k\ell,22}^{(1)} \end{bmatrix} = \frac{(1-\delta_{k\ell})\left(\mathrm{e}^{\mathrm{i}\frac{2\pi}{N}\sigma_1(\ell-1)}-1\right)\mathrm{e}^{\mathrm{i}\frac{2\pi}{N}(i_1-1)(\ell-k)}}{N\eta_{k\ell}(p-\alpha\beta_1)} \begin{bmatrix} \beta_1\eta_{\ell 1} \\ -p\eta_{\ell 1} \\ -1 \\ \alpha \end{bmatrix}. \tag{5.72}$$

Using the first-order pertubations upon $\hat{\mathbf{T}}$ we can obtain the second-order perturbation on the dynamics of mode k with respect to any two long-range links described by the indices $i_1,\sigma_1,i_2,\sigma_2$. In particular, (5.49) yields

$$[\hat{\mathbf{D}}^{(1,2)}]_k^k = [\hat{\mathbf{D}}_2(i_1,\sigma_1,i_2,\sigma_2)]_k^k = \begin{bmatrix} 0 & 0 \\ -2K_0(i_1,\sigma_1,i_2,\sigma_2) & -2K_1(i_1,\sigma_1,i_2,\sigma_2) \end{bmatrix}, \tag{5.73}$$

where

$$K_0(i_1,\sigma_1,i_2,\sigma_2) = \frac{p\eta_{k1}}{N^2(p-\alpha\beta_1)} \sum_{j=1,j\neq k}^{N} \frac{(e^{i\frac{2\pi}{N}\sigma_1(j-1)}-1)(e^{i\frac{2\pi}{N}\sigma_2(k-1)}-1)e^{i\frac{2\pi}{N}(i_1-i_2)(j-k)}}{\eta_{jk}},$$
$$K_1(i_1,\sigma_1,i_2,\sigma_2) = \frac{-\alpha}{N^2(p-\alpha\beta_1)} \sum_{j=1,j\neq k}^{N} \frac{(e^{i\frac{2\pi}{N}\sigma_1(j-1)}-1)(e^{i\frac{2\pi}{N}\sigma_2(k-1)}-1)e^{i\frac{2\pi}{N}(i_1-i_2)(j-k)}}{\eta_{jk}}. \tag{5.74}$$

Note that the second-order terms for two different links will depend on the parameters α, β_1, p, the indices of receiving cars (i_1,i_2), and the link lengths (σ_1,σ_2). Thus, a second-order approximation accounts for the interactions between the long-range links.

To get the second-order terms for the modal coordinate transformation (5.22) we solve (5.54) with matrices

$$\mathbf{A}_{k\ell}^{(1,2)} = \begin{bmatrix} 0 & 1 & -p\eta_{\ell 1} & 0 \\ p\eta_{k1} & \beta_1\eta_{k1}-\alpha & 0 & -p\eta_{\ell 1} \\ -1 & 0 & -\beta_1\eta_{\ell 1}+\alpha & 1 \\ 0 & -1 & p\eta_{k1} & \beta_1\eta_{k\ell} \end{bmatrix}, \tag{5.75}$$

and

$$\mathbf{c}_{k\ell}^{(1,2)} = \frac{2}{N} \begin{bmatrix} 0 \\ -\sum_{j=1}^{N} e^{i\frac{2\pi}{N}(i_1-1)(j-k)}(e^{i\frac{2\pi}{N}\sigma_1(j-1)}-1)u_{j\ell,21}^{(2)} \\ u_{k\ell,12}^{(1)}(e^{i\frac{2\pi}{N}\sigma_2(\ell-1)}-1) \\ u_{k\ell,22}^{(1)}(e^{i\frac{2\pi}{N}\sigma_2(\ell-1)}-1) - \sum_{j=1}^{N} e^{i\frac{2\pi}{N}(i_1-1)(j-k)}(e^{i\frac{2\pi}{N}\sigma_1(j-1)}-1)u_{j\ell,22}^{(2)} \end{bmatrix}, \tag{5.76}$$

where $u_{k\ell,\cdot\cdot}^{(1)}$ represent the elements of the 2×2 block $[\hat{\mathbf{U}}^{(1)}]_\ell^k$ are given by (5.72). The solution for the $\mathbf{b}_{k\ell}^{(1,2)}$ is given in Appendix I.

Using the elements of $\mathbf{b}_{k\ell}^{(1,2)}$ (cf. (I.2)) we can obtain the third-order perturbations of the dynamics due to any three long-range links defined by the indices $i_1,\sigma_1,i_2,\sigma_2,i_3,\sigma_3$ as

$$[\hat{\mathbf{D}}^{(1,2,3)}]_k^k = [\hat{\mathbf{D}}_3(i_1,\sigma_1,i_2,\sigma_2,i_3,\sigma_3)]_k^k = \begin{bmatrix} 0 & 0 \\ -6L_0(i_1,\sigma_1,i_2,\sigma_2,i_3,\sigma_3) & -6L_1(i_1,\sigma_1,i_2,\sigma_2,i_3,\sigma_3) \end{bmatrix}, \tag{5.77}$$

where $L_0(i_1,\sigma_1,i_2,\sigma_2,i_3,\sigma_3)$ and $L_1(i_1,\sigma_1,i_2,\sigma_2,i_3,\sigma_3)$ are given in Appendix J (see (J.1)).

Thus, based on (5.59) the dynamics for mode k approximated up to third-order in $\beta_{i\sigma}$ become

$$\begin{aligned}\dot{\mathbf{z}}_k = \Bigg(&\begin{bmatrix} 0 & 1 \\ p\eta_{k1} & \beta_1\eta_{k1} - \alpha \end{bmatrix} + \frac{1}{N}\sum_{i_1=1}^{N}\sum_{\sigma_1=2}^{\sigma_{\max}} \begin{bmatrix} 0 & 0 \\ 0 & \left(\mathrm{e}^{\mathrm{i}\frac{2\pi}{N}\sigma_1(k-1)} - 1\right) \end{bmatrix} \beta_{i_1\sigma_1} \\ &+ \sum_{i_1,i_2=1}^{N}\sum_{\sigma_1,\sigma_2=2}^{\sigma_{\max}} \begin{bmatrix} 0 & 0 \\ -K_0(i_1,\sigma_1,i_2,\sigma_2) & -K_1(i_1,\sigma_1,i_2,\sigma_2) \end{bmatrix} \beta_{i_1\sigma_1}\beta_{i_2\sigma_2} \\ &+ \sum_{i_1,i_2,i_3=1}^{N}\sum_{\sigma_1,\sigma_2,\sigma_3=2}^{\sigma_{\max}} \begin{bmatrix} 0 & 0 \\ -L_0(i_1,\sigma_1,i_2,\sigma_2,i_3,\sigma_3) & -L_1(i_1,\sigma_1,i_2,\sigma_2,i_3,\sigma_3) \end{bmatrix} \beta_{i_1\sigma_1}\beta_{i_2\sigma_2}\beta_{i_3\sigma_3} \Bigg) \mathbf{z}_k, \end{aligned} \tag{5.78}$$

where the coefficients for the second and third-order terms are given in (5.74) and (J.1), respectively.

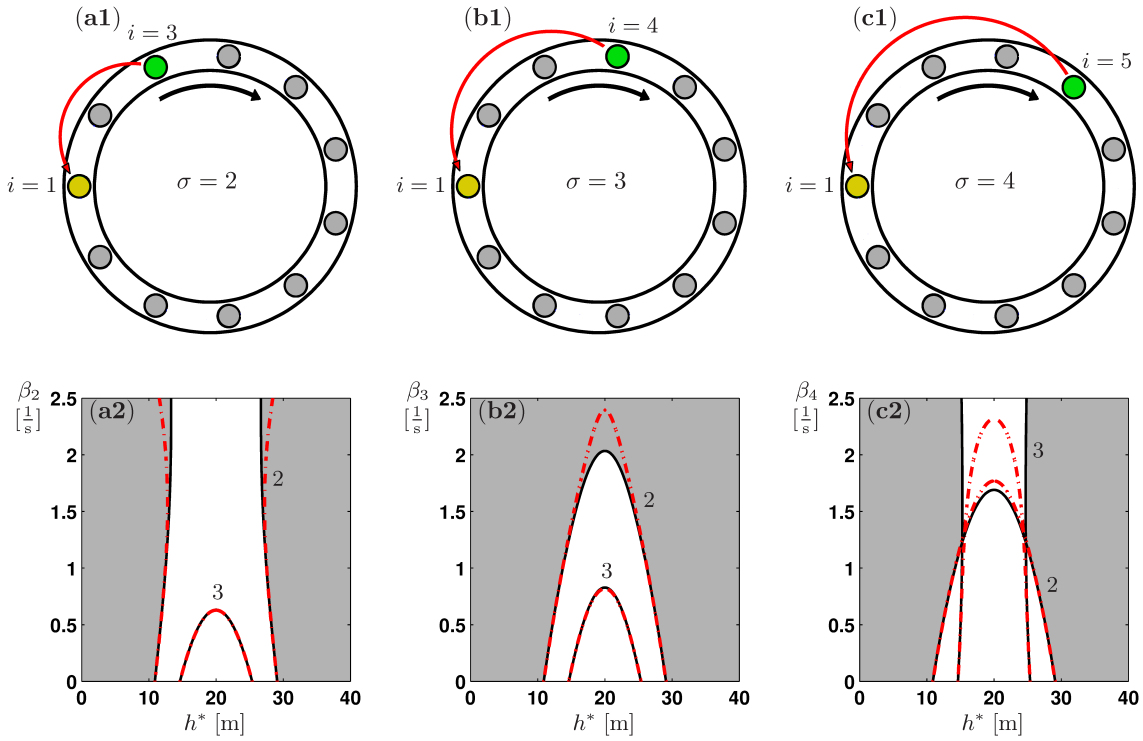

Figure 5.4: Top row: Diagrams of the vehicle configurations with a long-range V2V link for different link lengths for 11 cars. Bottom row: Corresponding stability charts in the (h^*, β_σ) plane when considering $\beta_1 = 0.3\,[\frac{1}{\mathrm{s}}]$ and $\alpha = 1\,[\frac{1}{\mathrm{s}}]$. The red curves denote the stability boundaries for the modes 2 and 3 obtained through the derived analytical approximation up to third-order in β_σ, while the black curves denote the linear stability boundaries obtained by numerical continuation. The grey shaded region corresponds to stable uniform flow.

To analyze the stability the modes we use the trial solution $\mathbf{z}_k(t) = \mathbf{z}_{k\,0}\mathrm{e}^{\lambda t}$ with $\mathbf{z}_{k\,0} \in \mathbb{C}^2$

and $\lambda \in \mathbb{C}$ for mode k. Thus (5.78) yield the characteristic equation for

$$\lambda^2 + \Bigg(-\beta_1 \eta_{k1} + \alpha + \frac{1}{N} \sum_{i_1=1}^{N} \sum_{\sigma_1=2}^{\sigma_{\max}} (1 - \mathrm{e}^{\mathrm{i}\frac{2\pi}{N}\sigma_1(k-1)}) \beta_{i_1\sigma_1} + \sum_{i_1,i_2=1}^{N} \sum_{\sigma_1,\sigma_2=2}^{\sigma_{\max}} K_1(i_1,\sigma_1,i_2,\sigma_2)\beta_{i_1\sigma_1}\beta_{i_2\sigma_2} + \sum_{i_1,i_2,i_3=1}^{N} \sum_{\sigma_1,\sigma_2,\sigma_3=2}^{\sigma_{\max}} L_1(i_1,\sigma_1,i_2,\sigma_2,i_3,\sigma_3)\beta_{i_1\sigma_1}\beta_{i_2\sigma_2}\beta_{i_3\sigma_3} \Bigg)\lambda + \Bigg(-p\eta_{k1} + \sum_{i_1,i_2=1}^{N} \sum_{\sigma_1,\sigma_2=2}^{\sigma_{\max}} K_0(i_1,\sigma_1,i_2,\sigma_2)\beta_{i_1\sigma_1}\beta_{i_2\sigma_2} + \sum_{i_1,i_2,i_3=1}^{N} \sum_{\sigma_1,\sigma_2,\sigma_3=2}^{\sigma_{\max}} L_0(i_1,\sigma_1,i_2,\sigma_2,i_3,\sigma_3)\beta_{i_1\sigma_1}\beta_{i_2\sigma_2}\beta_{i_3\sigma_3} \Bigg) = 0. \tag{5.79}$$

We examine the stability of the connected vehicle network and its modes with respect to the equilibrium headway h^*. By considering the critical case $\lambda = \mathrm{i}\omega$ we calculate the critical value of p_k using (5.79) which results in the corresponding headway h_k^* using (2.5,2.8,2.19) and determine the corresponding frequency ω_k. As both p_k and ω_k depend on the gains $\beta_{i\sigma}$ and we write these as expansions in $\beta_{i\sigma}$ up to third-order as

$$\begin{aligned} p_k = p_{k0} &+ \sum_{i_1=1}^{N} \sum_{\sigma_1=2}^{\sigma_{\max}} p_{k1}(i_1,\sigma_1)\beta_{i_1\sigma_1} + \frac{1}{2} \sum_{i_1,i_2=1}^{N} \sum_{\sigma_1,\sigma_2=2}^{\sigma_{\max}} p_{k2}(i_1,\sigma_1,i_2,\sigma_2)\beta_{i_1\sigma_1}\beta_{i_2\sigma_2} \\ &+ \frac{1}{6} \sum_{i_1,i_2,i_3=1}^{N} \sum_{\sigma_1,\sigma_2,\sigma_3=2}^{\sigma_{\max}} p_{k3}(i_1,\sigma_1,i_2,\sigma_2,i_3,\sigma_3)\beta_{i_1\sigma_1}\beta_{i_2\sigma_2}\beta_{i_3\sigma_3} + \ldots, \end{aligned} \tag{5.80}$$

and

$$\begin{aligned} \omega_k = \omega_{k0} &+ \sum_{i_1=1}^{N} \sum_{\sigma_1=2}^{\sigma_{\max}} \omega_{k1}(i_1,\sigma_1)\beta_{i_1\sigma_1} + \frac{1}{2} \sum_{i_1,i_2=1}^{N} \sum_{\sigma_1,\sigma_2=2}^{\sigma_{\max}} \omega_{k2}(i_1,\sigma_1,i_2,\sigma_2)\beta_{i_1\sigma_1}\beta_{i_2\sigma_2} \\ &+ \frac{1}{6} \sum_{i_1,i_2,i_3=1}^{N} \sum_{\sigma_1,\sigma_2,\sigma_3=2}^{\sigma_{\max}} \omega_{k3}(i_1,\sigma_1,i_2,\sigma_2,i_3,\sigma_3)\beta_{i_1\sigma_1}\beta_{i_2\sigma_2}\beta_{i_3\sigma_3} + \ldots. \end{aligned} \tag{5.81}$$

To obtain the coefficients in (5.80) and (5.81), we substitute them into (5.79), differentiate the result with respect to the $\beta_{i\sigma}$, evaluate the results at $\beta_{i\sigma} = 0$, and solve the two resulting algebraic equations for the terms of p_k and ω_k. The corresponding details are given in Appendix K.

The approximation to the stability boundary above can be used to directly determine the values of h_k^* at which stability is lost for mode k. Alternatively, given an equilibrium headway h^* one can find the set of gains to guarantee the linear stability of all modes.

5.3.3 Stability diagrams

In this subsection we visualize the results presented in the previous subsection using stability charts for connected vehicle networks with different connectivity structures. We plot the analytical approximations of the modal stability boundaries derived above and validate these results using numerical continuation. We consider long-range V2V links of length $2, 3$, and 4. For simplicity, we assume that links of the same length use the same gain, i.e.,

$$\beta_{i2} = \beta_2, \quad \beta_{i3} = \beta_3, \quad \beta_{i4} = \beta_4. \tag{5.82}$$

We use the range policy (2.5,2.8) with $h_{\text{st}} = 5\,[\text{m}]$, $h_{\text{go}} = 35\,[\text{m}]$, and $v_{\max} = 30\,[\frac{\text{m}}{\text{s}}]$.

We first examine the effect of a single long-range link on the stability of connected vehicle networks. When vehicle $i = 1$ is receiving information through a link of length σ, as depicted in Figure 5.4(a1-c1), the linearized dynamics is described by (5.9) with matrix

$$\hat{\mathbf{J}} = \hat{\mathbf{J}}_0 + \hat{\mathbf{P}}(1,\sigma)\beta_\sigma, \tag{5.83}$$

cf. (5.10) where $\varepsilon_{1\sigma} = \beta_\sigma$ is the gain for the link of length σ terminated at vehicle 1.

We first analyze the effect of link of length $\sigma = 2$ on the modal stability boundaries in the (h^*, β_2) plane for various values of α and β_1. Note, like in the previous section due to the fact that the range policy is the same for all vehicles $h^* = h^*_{\text{avg}}$. The results are summarized in Figure 5.3. The dashed red curves represent the analytical approximations of the modal stability boundaries up to third-order in β_2, while the solid black curves denote the boundaries obtained through numerical continuation [78]. Grey shading denotes stable uniform flow. The corresponding mode numbers k are shown next to each boundary. Only modes corresponding to $k = 2 \ldots \lfloor \frac{N}{2} + 1 \rfloor$ are shown, since modes k and $N + 2 - k$ are complex conjugates and therefore correspond to the same set of stability boundaries. The instability region for each mode is confined between the modal boundaries of that mode. Although the exact boundaries may cross each other (see Figure 5.3(a)), the stability for the connected vehicle network, is always given by mode 2 for the cases examined here.

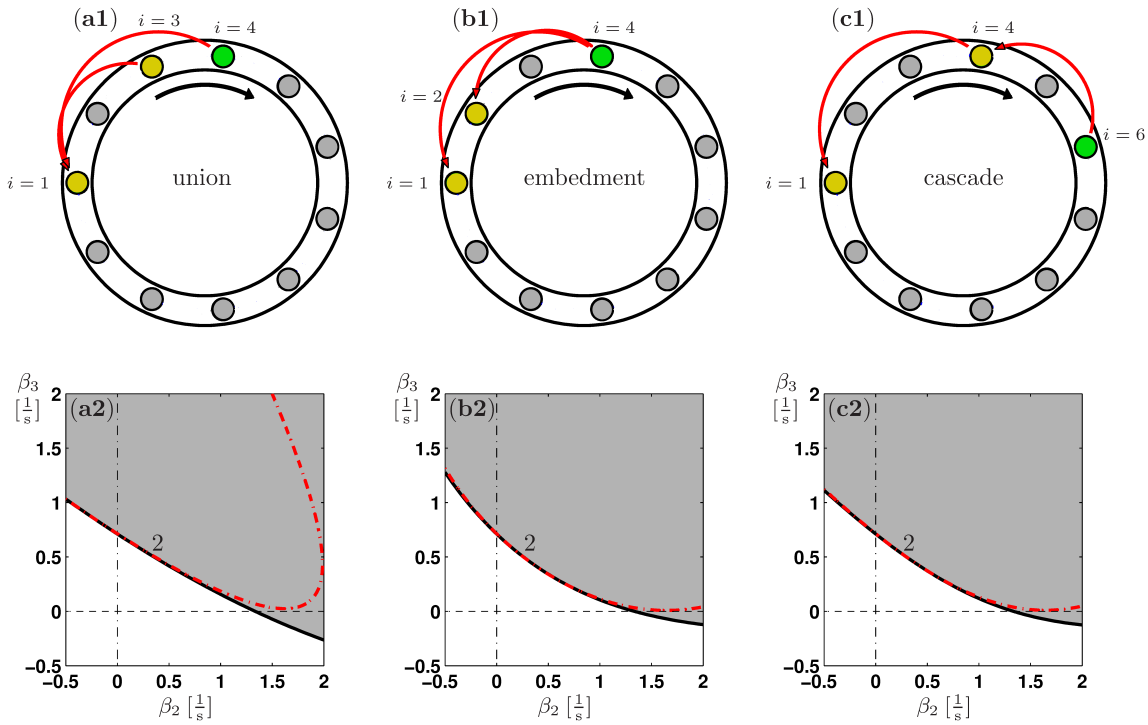

Figure 5.5: Top row: Connected vehicle networks with 11 cars and links of length 2 and 3 arranged in different configurations. Bottom row: Stability charts in the (β_2, β_3) plane for $h^* = 20\,[\mathrm{m}]$, $\beta_1 = 0.6\,[\frac{1}{\mathrm{s}}]$, and $\alpha = 1\,[\frac{1}{\mathrm{s}}]$. The same notation is used as in Figure 5.4.

Figure 5.3(a) contains four stability boundaries $k = 2, \ldots, 6$. When increasing β_2, the instability region for each mode shrinks and the uniform flow becomes stable for a wider range of h^*. As β_2 increases further some modal stability boundaries ($k = 3$ and 5) fold back, increasing the corresponding regions of instability. However, the $k = 2$ stability boundary (that gives the primary instability) is nearly vertical, so changing β_2 does not change the stability region significantly. As we increase the values of α and β_1 (going down and to the right in Figure 5.3), stability boundaries for higher mode numbers disappear, and the range of h^* for which the system is stable increases. In fact, in Figure 5.3(f,h,k) the connected vehicle network can be completely stabilized for a large enough gain β_2. Notice that the analytical approximations for the modal boundaries become more accurate for larger values of α and β_1 due to stronger cyclically symmetrical coupling.

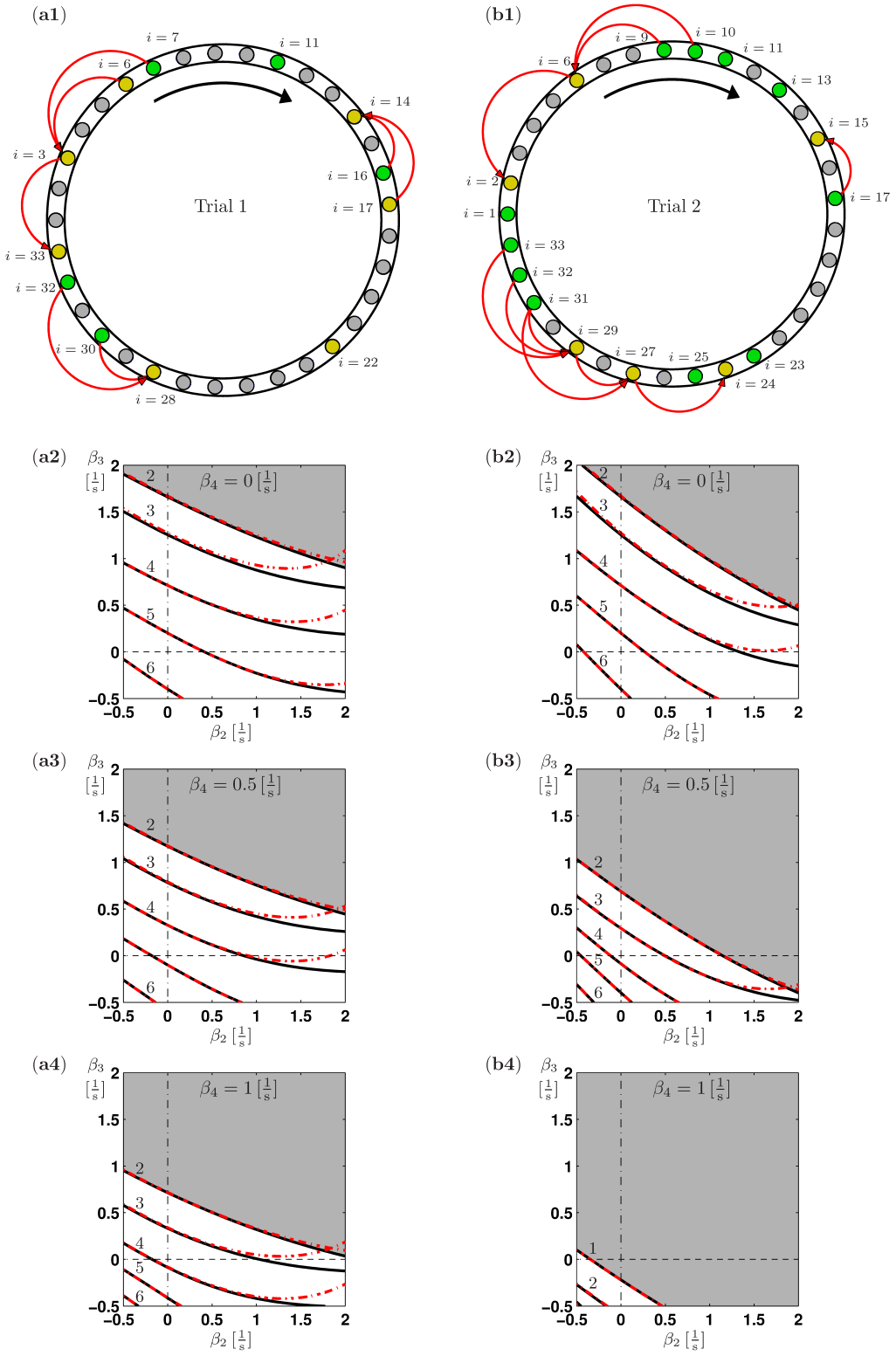

Figure 5.6: (a1,b1):Two connected vehicle networks with 33 vehicles. (a2-a4,b2-b4): Corresponding stability charts in the (β_2, β_3) plane corresponding to for $h^* = 20\,[\mathrm{m}]$, $\alpha = 1\,[1/\mathrm{s}]$, $\beta_1 = 0.6\,[1/\mathrm{s}]$, and various values of β_4 as indicated. The same notation is used as in Figure 5.4.

Next we consider the effect of varying the length of the long-range link. In Figure 5.4 we compare the linear stability charts when a long-range link of length $\sigma = 2$, $\sigma = 3$, $\sigma = 4$ is added to an 11-car network. The configurations are depicted in Figure 5.4(a1), (b1), (c1), respectively, where the corresponding stability boundaries are shown in Figure 5.4 (a2), (b2), (c2). In the case of $\sigma = 3$, increasing the gain β_σ corresponding to V2V link improves the stability (still determined by mode 2) more than in the case of $\sigma = 2$. In fact, a sufficiently large gain β_3 can be used to stabilize the uniform flow for all values of h^*. However, increasing β_3 has a smaller effect on the stability of mode 3 than increasing β_2, and it takes a larger value of β_3 to stabilize mode 3 for all values of h^*. In the case of $\sigma = 4$ increasing β_4 benefits the stability of the network for low values of β_4 where the stability boundary is given by mode 2. However, for $\beta_4 \gtrsim 1.23\ [1/\mathrm{s}]$ the stability of the network is governed by mode 3, and increasing β_4 further has limited impact on the stability of the network.

After examining the effects of individual V2V links on stability of connected vehicle networks, we analyze the effects of combinations of these links. We first consider the scenario when the connected vehicle network contains two V2V links of different lengths ($\sigma = 2$ and $\sigma = 3$), and examine the stability for different configurations. A detailed description of different configurations can be found in [109] while examples of such combinations for an 11-car network are given at the top of Figure 5.5. In the union configuration shown in Figure 5.5(a1) a single connected automated vehicle ($i = 1$) utilizes information from multiple vehicles ahead ($i = 3$ and $i = 4$). In the embedment configuration depicted in Figure 5.5(b1) two distinct connected automated vehicles ($i = 1$ and $i = 2$) utilize information from a single connected human-driven vehicle ($i = 4$). In the cascade configuration shown in Figure 5.5(c1), a connected automated vehicle ($i = 1$) utilizes information from a connected vehicle ahead ($i = 4$), which also utilizes information from a vehicle further ahead ($i = 6$). The bottom row of Figure 5.5 shows the stability charts for the three configurations in the (β_2, β_3) plane. The regions of stability for the three different configurations are similar, but the stability boundaries for the embedment and cascade cases are more concave. This indicates that the cascade and embedment configurations may have a greater benefit on the stability of the network than the "sum" of the individual links in these configurations.

After analyzing the typical configurations appearing in connected vehicle networks, we use the methodology outlined in Figure 2.1 to construct a connected vehicle network for a ring with 33 cars. We set up the network as explained in Figure 2.1 B-D by first randomly selecting the connected vehicles with a probability of 0.5 and then randomly selecting the connected automated vehicles with a probability of 0.5 out of the connected vehicles. Two of such connected vehicle networks are shown in Figure 5.6(a1,b1), labeled by "Trial 1" and

"Trial 2". In both cases combinations of unions, embedment and cascades appear. Figure 5.6(a2-b2) shows stability charts for the two trials in the (β_2, β_3) plane for different values of β_4. In Figure 5.6(a2,b2), we have $\beta_4 = 0$, and stability boundaries for modes 2 through 6 appear. Note that the origin denotes the case of no V2V communication where modes 2 through 5 are unstable. Observe that the uniform flow can be stabilized by selecting sufficiently large gains β_2 and β_3. As β_4 is increased, the modal stability boundaries move down, and the network can be stabilized using smaller values of β_2 and β_3. In Figure 5.6(b4) only stability boundaries for modes 2 through 4 are present. Furthermore, Figure 5.6(b4) demonstrates that uniform flow can be stabilized only by using links of length 4, since the origin is located in the region of stable uniform flow.

5.4 Summary

In this chapter we analyzed the dynamics of connected vehicle networks consisting of conventional vehicles that respond to the vehicle immediately ahead, connected vehicles that are able to transmit and receive information through wireless vehicle-to-vehicle communication and connected automated vehicles equipped with connected cruise control (CCC) that use wireless vehicle-to-vehicle communication to respond to multiple vehicles ahead.

The nontrivial connectivity structure of such connected vehicle networks (CVNs) motivated us to develop a perturbation technique to approximate the modal dynamics of networks with heterogeneous connectivity by perturbing the modes of a corresponding cyclically symmetric network. First, the modal dynamics of the underlying cyclically symmetric network were determined through a discrete Fourier transformation. Subsequently the approximations to the modes of the heterogeneous network were obtained about the symmetric state. These expansions were obtained using linear algebraic equations that were decoupled by exploiting the symmetry of the underlying cyclically symmetric network. Specifically for a system with N nodes and M equations per node this reduction allows one to solve N^2 decoupled linear systems of M^2 unknowns instead of solving a single linear system with $(NM)^2$ unknowns. For example, if $N = 100$ and $N = 2$, we wold need to solve 10000 decoupled linear systems with 4 unknowns rather than a linear system with 40000 unknowns, which is a significant simplification. Furthermore the resulting N^2 decoupled linear systems hare similar structure, which allows one to algorithmize the solution for increased efficiency.

This modal approximation technique was applied to heterogeneous connected vehicle systems including connected automated vehicles which can also react to the velocity of up to four vehicles ahead. We first obtained the modal dynamics of the cyclically symmetric system containing no connected automated vehicles. To obtain approximations of the modal

equations when the connected vehicle network contains connected automated vehicles, we calculated the modal expansions around the symmetric modes up to third-order in the V2V link gains. Using the obtained approximations we were able to analytically determine the modal stability boundaries for the heterogeneous connected vehicle networks. We validated the results by comparing these analytical boundaries to those obtained by numerical continuation.

We conclude that adding connected automated vehicles to a vehicle network of human driven vehicles may stabilize the uniform flow. We observed that longer V2V links are more effective at stabilizing modes of low wave numbers, and less effective at stabilizing modes of high wave numbers. When adding multiple V2V links to a vehicle network, specific combinations of V2V links may enhance the impacts of the individual links on the stability of uniform flow. Finally, we demonstrated that in a large CVN having a few appropriately designed V2V links may be adequate to stabilize the uniform flow.

We found the network-based modal approximation technique to be effective in analyzing the linear stability of large connected vehicle networks with heterogeneous connectivity. After analytically showing that V2V communication can be beneficial to stabilizing uniform flow in connected vehicle networks, it would be interesting to assess the effects of V2V communication on the nonlinear dynamics of a connected vehicle network. Furthermore incorporating human reaction delays and vehicle acceleration limits into the model would give us a better interpretation of the impacts of connected and automated vehicles on traffic flow.

CHAPTER 6

Simulations of large connected vehicle networks

The experiments on the 3-car connected vehicle network performed in Chapter 3 demonstrate that changing the way the connected automated vehicle responds to information from vehicles traveling ahead may influence the behavior of the overall connected vehicle network. In particular, we noted that a connected automated vehicle using long-range feedback may allow all vehicles in the network to travel faster and approach uniform flow. Furthermore, we demonstrated that for well-tuned parameters the car following models are able to reproduce experimental results. Supplementarily, in Chapter 4 we have seen that human drivers tend to develop stop-and-go traffic jams in large vehicle networks for a wide range of parameters. Furthermore we have shown that for some traffic densities uniform flows and traffic jams may develop based on the perturbation introduced by vehicles into the network. In Chapter 5 we analytically showed that adding connected and connected automated vehicles may stabilize the uniform flow of networks if the gains were tuned appropriately.

In this chapter we investigate effects of connected automated vehicles on traffic by considering large connected vehicle networks consisting of regular human-driven vehicles (HVs), connected human-driven vehicles (CHVs), and connected automated vehicles (CAVs). We use the models defined in Chapter 1 without any simplification and with parameters determined in Appendix B to characterize human drivers in these simulations. We develop a criterion to baseline the performance of a network of regular human-driven vehicles and then investigate the effects of adding connected vehicles and connected automated vehicles.

6.1 Connected vehicle network setup

We simulate a connected vehicle network of N vehicles on a ring road of length L so that the the first vehicle travels behind the N-th vehicle resulting in the periodic boundary conditions $s_{N+1} = s_1 + L$ and $v_{N+1} = v_1$. Similarly to the previous chapters we consider the ring configuration outlined in section 2.2.2, but we do not consider ring road geometry (that

would require to model lateral and yaw dynamics) but rather simply utilize these periodic boundary condition to obtain a closed system. Correspondingly, the distances between the vehicles are calculated using arclengths rather than secants.

Each of the cars is then assigned to be a human-driven vehicle (HV), a connected human-driven vehicle (CHV), or a connected automated vehicle (CAV). We first randomly select n_{cv} vehicles in the network to be connected. Then we select n_{cav} of the connected vehicles to be connected automated. Indeed, the number of connected human-driven vehicles in this network $n_{\text{cv}} - n_{\text{cav}}$. We define the connected vehicle penetration rate as $100\frac{n_{\text{cv}}}{N}$ % and the connected automated vehicle penetration rate as $100\frac{n_{\text{cav}}}{n_{\text{cv}}}$ %.

In order to model highway scenarios, we set $h_{\text{st}} = 5$ [m] and $v_{\max} = 30$ [m/s] for all drivers, cf. (2.5,2.7) and Figures 2.2 D. To account for the variation between human drivers we assign h_{go} for each human driver from a uniform random distribution in the interval $[45, 55]$ [m]. The other human parameters are set to $\tau_h = 1.0$ [s], $\alpha = 0.14\ [1/\text{s}]$ and $\beta = 0.54\ [1/\text{s}]$, as determined from model matching; see Appendix B. Likewise we adjust the range policy of the CAV so that $v_{\max} = 30$ [m/s] while we still use κ to tune the "aggressiveness" of the CAVs; see (2.14) and Figure 2.2. We investigate the effects of κ as well as the effects of long-range V2V communication on the global behavior of the constructed connected vehicle networks.

When using long-range feedback the connected automated vehicle i considers connected vehicles up to a look-ahead distance D that are moving slower than the immediate predecessor (vehicle $i+1$). For these vehicles we calculate the weighted downstream velocity $\bar{v}_i^{(\text{d})}$ using (2.15) from Chapter 3 with weights:

$$w_{ij} = \begin{cases} w_i \text{ if } j = i+1 \\ w_i \text{ if } 0 < s_j - s_i < D \text{ and } v_j < v_{i+1}\,, \\ 0 \text{ otherwise}\,, \end{cases} \tag{6.1}$$

Note that we limit the number of vehicles in the set E_i^k to 5, as prior research shows that looking at more than 5 vehicles does not yield significant improvement in performance [27, 28].

One can show that the dynamics of the connected vehicle network (2.1)-(2.17) admits a uniform flow equilibrium where all the vehicles travel with constant speed while maintaining

constant spacings, that is,

$$\begin{aligned} &v_i(t) \equiv v^*, \\ &s_{i+1}(t) - s_i(t) - \ell_i \equiv h_i^*, \end{aligned} \tag{6.2}$$

where v^* and h_i^* are the uniform flow velocity and uniform flow spacing such that

$$v^* = V_i(h_i^*), \quad \sum_{i=1}^{N} (h_i^* + \ell_i) = L. \tag{6.3}$$

Indeed, we have the average spacing $h_{\text{avg}}^* = \frac{1}{N}\sum_{i=1}^{N} h_i^*$ cf. (3.7). Depending on the stability of the uniform flow, the connected vehicle network may converge to or diverge from the uniform flow after a perturbation is introduced. In the latter case traveling waves may form.

6.1.1 Testing procedure

We initialize simulations with all the cars traveling at uniform flow except the first vehicle, whose motion is perturbed according the speed profile shown in Figure 2.2 F. The magnitude of the perturbation is characterized by a dimensionless quantity $0 \leq \Delta \leq 1$ called severity. When $\Delta = 0$ no perturbation occurs and the car continues to move with the uniform flow. When $\Delta = 1$ the perturbed car first decelerates from v^* to 0 at the deceleration rate $a_{\min} < 0$; cf. Figure 2.2A. This deceleration happens over a time interval $T_{\text{b}} = -v^*/a_{\min}$. Then the car remains stationary for a time interval T_{c}. Finally, the car accelerates back to v^* at the acceleration rate $a_{\max} > 0$ (cf. Figure 2.2A) over a time $T_{\text{a}} = v^*/a_{\max}$.

For $0 < \Delta < 1$, the selected car reduces its speed by $\Delta \cdot v^*$ during the interval $0 \leq t < T_{\text{b}}$ using a constant deceleration. During $T_{\text{b}} \leq t < T_{\text{b}} + T_{\text{c}}$ the car coasts at a constant velocity of $(1-\Delta)v^*$. For our simulations we use $T_{\text{c}} = 5\,[\text{s}]$. Lastly, during $T_{\text{b}} + T_{\text{c}} \leq t < T_{\text{b}} + T_{\text{c}} + T_{\text{a}}$ the car increases its speed back to v^* using constant acceleration. During $0 \leq t \leq T_{\text{b}} + T_{\text{c}} + T_{\text{a}}$ the dynamics of the other vehicles in the network are governed by (2.1)-(2.17). For $t \geq T_{\text{b}} + T_{\text{c}} + T_{\text{a}}$ the dynamics of all vehicles are governed by these equations.

After introducing the perturbation, we observe the response of the network. As we are examining the merits of connected automated vehicles in benefiting traffic flow, we select our performance metric to be an average flux

$$q = \frac{1}{N}\sum_{i=1}^{N} q_i, \tag{6.4}$$

where the time-averaged flux of car i is given by

$$q_i = \frac{N+1}{t_{\mathrm{f}} - t_{\mathrm{set}}}. \tag{6.5}$$

Here the time t_{set} denotes the time where the simulation converges to a steady behavior and t_{f} is found by solving

$$s_i(t_{\mathrm{f}}) = L + s_i(t_{\mathrm{set}}). \tag{6.6}$$

In other words we determine the time it takes each vehicle to go once around the ring after the connected vehicle network gets close to steady motion. When vehicle i returns to the same point after going completely around the ring, $N+1$ vehicles would have traveled through that point. Given this, we can determine the flux from the perspective of car i in (6.5). We then average these results over all the vehicles in the connected vehicle network using (6.4).

6.2 Results

In this section we first examine the performance of vehicle networks consisting of regular human-driven vehicles (HVs) while varying the perturbation severity and the traffic density (the average vehicle spacing h^*_{avg} via adapting the ring length L, cf. (3.7)). We then investigate the dynamics when connected vehicles and connected automated vehicles are added to the traffic flow.

6.2.1 Human-driven network

We first look at the performance of a network solely consisting of regular human-driven vehicles in order to establish a baseline to which we can compare the performance of connected vehicle networks.

In Figure 6.1 the behavior of a vehicle network composed of 100 human drivers is shown, focusing on the effects of average vehicle spacing and perturbation severity on the large-scale traffic patterns. From Figures 6.1 A, C we observe that for $h^*_{\mathrm{avg}} = 35$ [m] a stop-and-go wave develops independent of the size of perturbations introduced to the network. While some of the vehicles are traveling at free flow speed others are stopped in congestion. When the average vehicle spacing is increased to $h^*_{\mathrm{avg}} = 45$ [m], the humans are able to return to the uniform flow after a small perturbation, see Figure 6.1 B, but large perturbations still lead to stop-and-go motion; see Figure 6.1 D.

In order to better understand the traffic patterns, we plot the average flux (6.4) as a function of the perturbation severity in Figure 6.1 E, F, that are generated using 10 different distributions of human drivers to account for the variation in human behavior. The mean values are plotted as points with the standard deviations captured by the error bars. For $h^*_{\text{avg}} = 35$ [m] the flux for all perturbations remains around 1600 [cars/hr]. This is related to the fact that congestion forms for all perturbations for the spacing $h^*_{\text{avg}} = 35$ [m]. For $h^*_{\text{avg}} = 45$ [m] the flux of the network at low perturbations is around 2200 [cars/hr], which corresponds to highway traffic capacity per lane. However, applying perturbations of severity 0.5 and larger the flux reduces to about 1700 [cars/hr] due to congestion waves.

To obtain a relationship between the flux and vehicle spacing, we plot the flux as a function of average vehicle spacing for $\Delta = 0.01$ and $\Delta = 1.0$ in Figure 6.1 G. For $h^*_{\text{avg}} \leq 40$ [m] both small and large perturbations lead to the same flux. For these spacings congestion develops even for a small perturbations, as demonstrated by Figure 6.1 A,C. For $40 \leq h^*_{\text{avg}} \leq 50$ [m] small perturbations result in a significantly higher flux than large perturbations since the human drivers are able mitigate small perturbations while large perturbations trigger congestion, as demonstrated by Figure 6.1 B,D. For $h^*_{\text{avg}} \geq 50$ [m], the flux resulting from small and large perturbations is the same again, since human drivers are able to sustain uniform flow for all perturbations examined.

6.2.2 Effects of connected automated vehicles

After baselining the performance of the human-driven network, we add connected and connected automated vehicles to the network and examine the performance of the resulting connected vehicle network. As an example, we consider 100% CV penetration and 30% CAV of CV penetration, that is 70 CHVs and 30 CAVs. This represents a scenario in which V2X communication is ubiquitous, but the penetration of automated vehicles is still limited.

First we show that in this scenario of partial penetration of connected automated vehicles, implementing nearest neighbor feedback (where the connected automated vehicle uses information solely from the vehicle immediately ahead) yields marginal benefits to traffic flux as the large-scale traffic patterns do not qualitatively change regardless of whether the connected automated vehicles are tuned to be more or less aggressive ($\kappa = 0.6$ or $\kappa = 1.0$ [1/s]).

Figures 6.2 and 6.3 A, C show that for $h^*_{\text{avg}} = 35$ [m] stop-and-go waves still develop for large and small perturbations regardless of κ being 0.6 or 1.0 [1/s]. For $h^*_{\text{avg}} = 45$ [m], likewise, the connected vehicle network goes to uniform flow for small perturbations, and a congestion wave forms for large perturbations for both κ values; see Figures 6.2 and 6.3

B, D. However, panel D shows less congestion compared to the human-driven network as vehicles do not stop in congestion.

To account for the distribution of the CAVs in the network for figures E, F, G, we use the results of 30 different connected vehicle networks. The points in each of these figures correspond to the mean flux, and the error bars indicate standard deviations. Adding connected automated vehicles leads to a slight (100 [cars/hr]) increase in flux at $h^*_{\text{avg}} = 35$ [m] for both the $\kappa = 0.6$ [1/s] and $\kappa = 1.0$ [1/s]; see panel E. For $h^*_{\text{avg}} = 45$ [m], using $\kappa = 0.6$ decreases the flux slightly compared to human drivers for perturbations for $\Delta < 0.5$; see Figure 6.2 F. This can be attributed to larger spacings between vehicles at uniform flow in the connected vehicle network. For $\Delta > 0.5$ the connected vehicle network maintains a higher flux than the human driven network as the congestion for the connected vehicle network is smaller. For $\kappa = 1.0$ [1/s] (Figure 6.3 F), the connected vehicle network always maintains a slightly higher flux than the human driver network, as the vehicles are closely packed at uniform flow and the congestion is less severe for higher perturbations.

Figure 6.2 G demonstrates that the connected vehicle network with $\kappa = 0.6$ [1/s] performs as good or better than the human-driver network for all h^*_{avg} except between 41 to 45 [m], where for the low perturbations the human-driver network does better. The difference in performance however is not large. When $\kappa = 1.0$ [1/s] (Figure 6.3 G) the connected vehicle network performs as good or slightly better than the human-driver network without any drawbacks. In particular from $19 \leq h^*_{\text{avg}} \leq 39$ the connected vehicle network slightly outperforms the human driven network for both large and small perturbations. For $41 \leq h^*_{\text{avg}} \leq 49$ [m] the connected vehicle network performs better than the human-driver network for large perturbations, and maintains the performance of the human-driver network for small perturbations.

Now we demonstrate that by using long-range feedback, the connected automated vehicles can significantly improve the flux of the connected vehicle network even at partial penetration. As before, we consider 100% CV penetration and 30% CAV of CV penetration, that is 70 CHVs and 30 CAVs.

Figure 6.4 A shows that at $h^*_{\text{avg}} = 35$ [m] the network stays close to uniform flow: in steady state the velocities oscillate by 1-2 [m/s]. Congestion does not develop unlike in the human driven network, or the connected vehicle networks with nearest-neighbor feedback. Large perturbations still result in stop-and-go congestion; see Figure 6.4 C. For $h^*_{\text{avg}} = 45$ [m], adding the connected automated vehicles with long-range feedback allows for the connected vehicle network to return to uniform flow even for large perturbations as demonstrated in Figure 6.4 D. These changes in traffic patterns are reflected in improvements in flux. In Figure 6.4 E, we see that at $h^*_{\text{avg}} = 35$ [m] for small perturbations the flux is

increased to 2400 [cars/hr], which corresponds to a 50% improvement over the previous networks examined. At $h^*_{\text{avg}} = 45$ [m] we see that the robustness of the connected vehicle network to perturbations is significantly improved, as the flux stays close to 2200 [cars/hr] for all perturbations.

As depicted in Figure 6.4 G the most significant improvement in flux over the previous network is for $35 \leq h^*_{\text{avg}} \leq 39$ [m] for small perturbations. In the case the connected vehicle network with long-range feedback is able to maintain uniform flow for these spacings. In general there are no drawbacks in terms of flux for using long-range feedback in connected automated vehicles compared to nearest-neighbor feedback, however, the significant flux improvements above give this strategy a significant advantage over nearest-neighbor feedback.

6.2.3 Penetration study

After seeing that long-range feedback is an effective strategy to improve traffic flow at partial penetrations of connected automated vehicles, we conduct a penetration study to see how many connected and connected automated vehicles are necessary to benefit the flux. In our 100 car network we vary the CV penetration in increments of 25% from 0% to 100%, which represent how "connected" the traffic environment is. We also vary the CAV of CV penetration in increments of 25% from 0% to 100%, which indicates the fraction of the connected vehicles that are automated.

Because most common perturbations are not severe (it's rare for someone to do a full stop on the highway), we chose to perturb the networks with $\Delta = 0.1$ (corresponding to a 10%) deviation of the speed from uniform flow. After the start of the perturbation we let the network run for 5 minutes and calculate the flux as in (6.4,6.5,6.6) with $t_f = 300$ [s] corresponding to the end of the simulation. The resulting flux of the connected vehicle network as a function of spacing $q_{\text{CVN}}(h^*_{\text{avg}})$ is compared to that of a network with 100 human-driven vehicles $q_{\text{HVN}}(h^*_{\text{avg}})$. The first metric we define yields the maximum increase in flux over all traffic densities

$$\delta q_{\max} = \max_{h \in [h_{\min}, h_{\max}]} \frac{q_{\text{CVN}}(h) - q_{\text{HVN}}(h)}{q_{\text{HVN}}(h)}. \tag{6.7}$$

To investigate the change in flux for a wide range of densities, we consider averaging the flux increase over the densities examined (between $h_{\min}$ and $h_{\max}$) and define another metric

$$\delta \bar{q} = \frac{1}{h_{\max} - h_{\min}} \int_{h_{\min}}^{h_{\max}} \frac{q_{\text{CVN}}(h) - q_{\text{HVN}}(h)}{q_{\text{HVN}}(h)} \mathrm{d}h. \tag{6.8}$$

We use $h_{\min} = 25$ [m] and $h_{\max} = 49$ [m]. The results for both $\delta q_{\max}$ and $\delta \bar{q}$ are shown in Figure 6.5 A, B. Note in this case we consider vehicles from $D = 300$ [m] ahead as before, as this was the range in which we observed no significant packet losses during experiments. From Figure 6.5 A we see that even when there is 25% CV penetration and 25% CAV of CV penetration (ie: 25 % connected vehicles and 6 connected automated vehicles in the network), the flux can be increased up to 6 % compared to the human connected vehicle network. With full connectivity (100% CV penetration) just 25% CAV penetration yields 25% increase in flux. Figure 6.5 B shows that on average 50% CV penetration and 25% CAV of CV penetration (50 CV's and 13 CAV's) yields close to 5% increase in flux on average over the human driven network. For full connectivity, even 25 CAV's improve the flux by over 10% on average. Note that for a given number of CAVs, increasing the number of CHV's yields an improvement in flux. That is, 50% CV penetration and 25% CAV of CV penetration yields higher metrics than 25% CV penetration and 50% CAV of CV penetration, while both scenarios have 13 connected automated vehicles.

In Figures 6.5 C,D we show the results in which we take the look ahead-distance D to be 600 [m] rather than 300 [m]. The results are not significantly different for either metric. Even when we increase the look ahead distance to 900 [m], as shown in Figures 6.5 E,F, there is no significant difference in performance compared to when the CAV's only look ahead 300 [m].

6.3 Summary

To characterize the effect of vehicle-to-vehicle connectivity on traffic patterns, we designed a small-scale experiment featuring three cars: two connected human-driven vehicles and one connected automated vehicle. This experimental setup allowed us to evaluate the effect of different types of feedback used by the connected automated vehicle on traffic patterns at a realistic range of speeds. The results showed that utilizing long-range feedback by the connected automated vehicle enables all vehicles to travel at high speeds for a given traffic density as well as prevent undesirable traffic oscillations. Furthermore, our proposed car-following model with delay replicated experimental results. We used simulations to investigate the effects of adding connected automated vehicles to human-driven traffic in a 100-vehicle connected vehicle network. We observed that although having some automated vehicles in the network brings benefits in terms of flux over human-driven vehicles, significant benefits of the connected automated vehicles are only realized when they are using long-range feedback from multiple vehicles ahead. Our results show that using long-range feedback is critical for realizing the benefits of connected automated vehicles on

traffic flow. Furthermore we show that even for small penetrations of connected automated vehicles (13 connected automated vehicles per 100 cars), flux can be improved by 5% for a wide range of traffic densities provided half of the vehicles on the road are connected vehicles. Full connectivity will yield even more significant benefits (over 10% across a wide range of densities), even if only a quarter of the vehicles are connected automated. Finally, we showed that with our strategy CAV's do not benefit by receiving information from connected vehicles over 300 [m] ahead even for small penetrations.

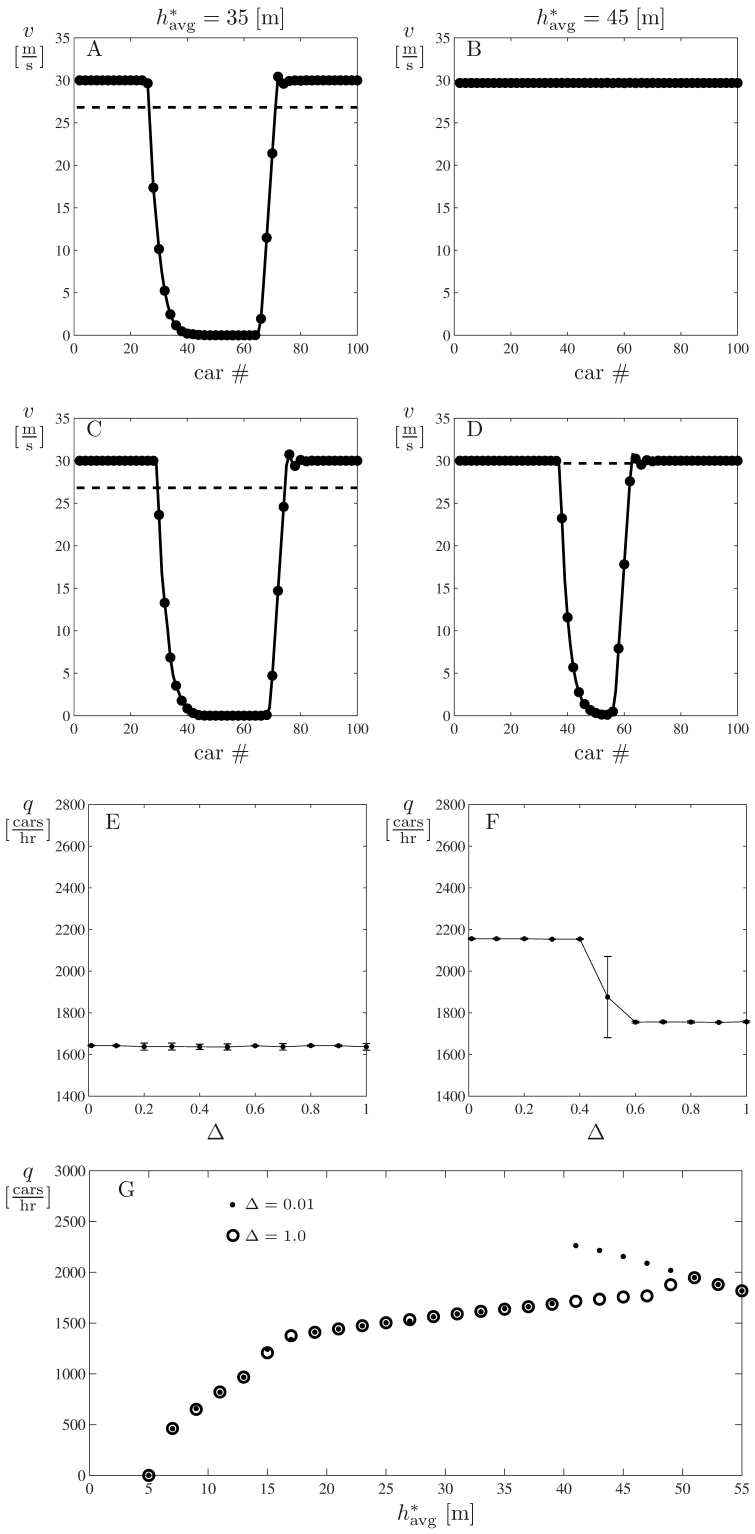

Figure 6.1: Behavior of a network consisting of 100 human-driven vehicles. A-D: Distributions of velocities in the network at the end of the simulation for different Δ and h^*_{avg}. The dashed line indicates the uniform flow. E, F: Flux-severity charts. G: Flux-spacing chart for different severities as indicated.

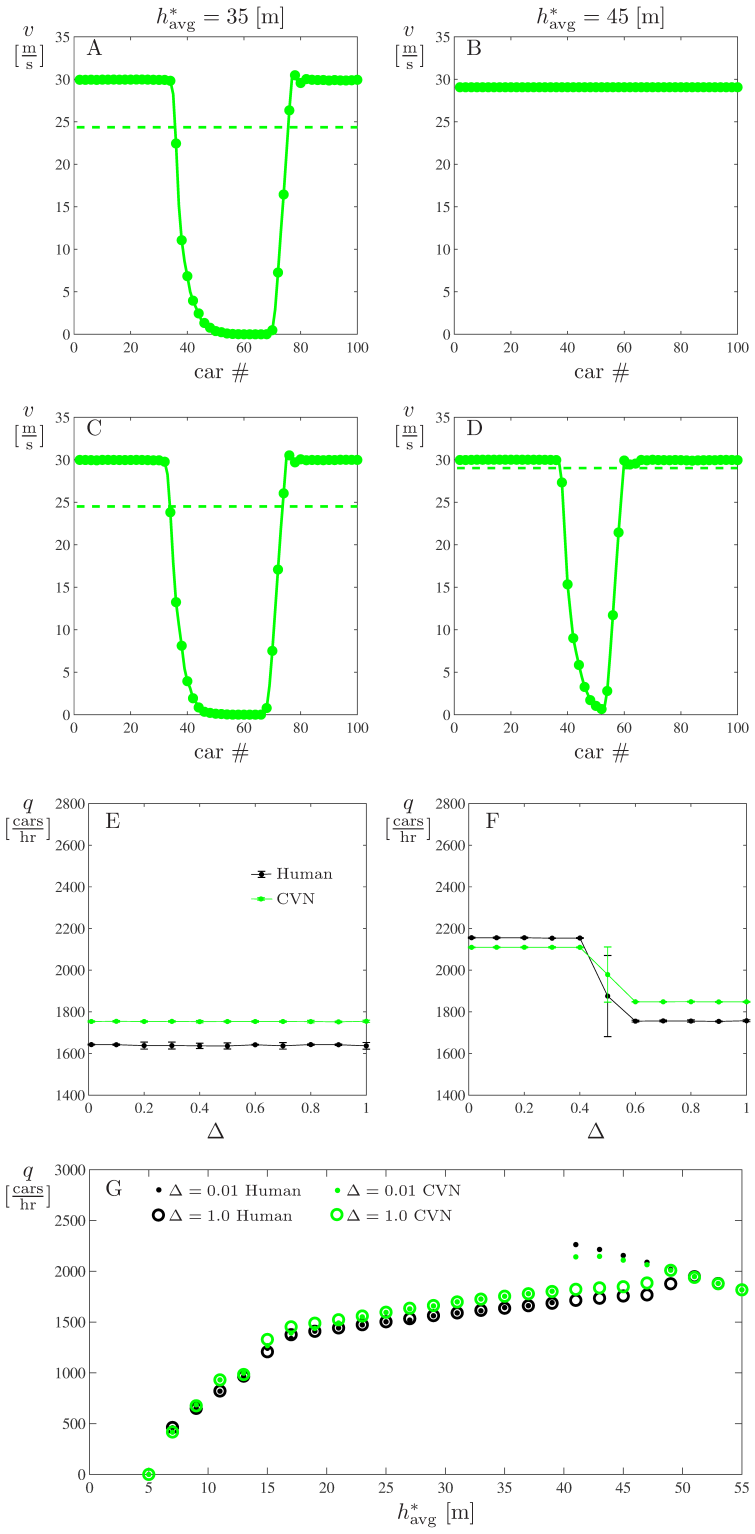

Figure 6.2: Behavior of a network with 100% CV penetration and 30% CAV of CV penetration (70% CHVs and 30% CAVs) with the CAVs using nearest neighbor feedback with $\kappa = 0.6$ [1/s] range policy. Same notation is used as in Figure 6.1.

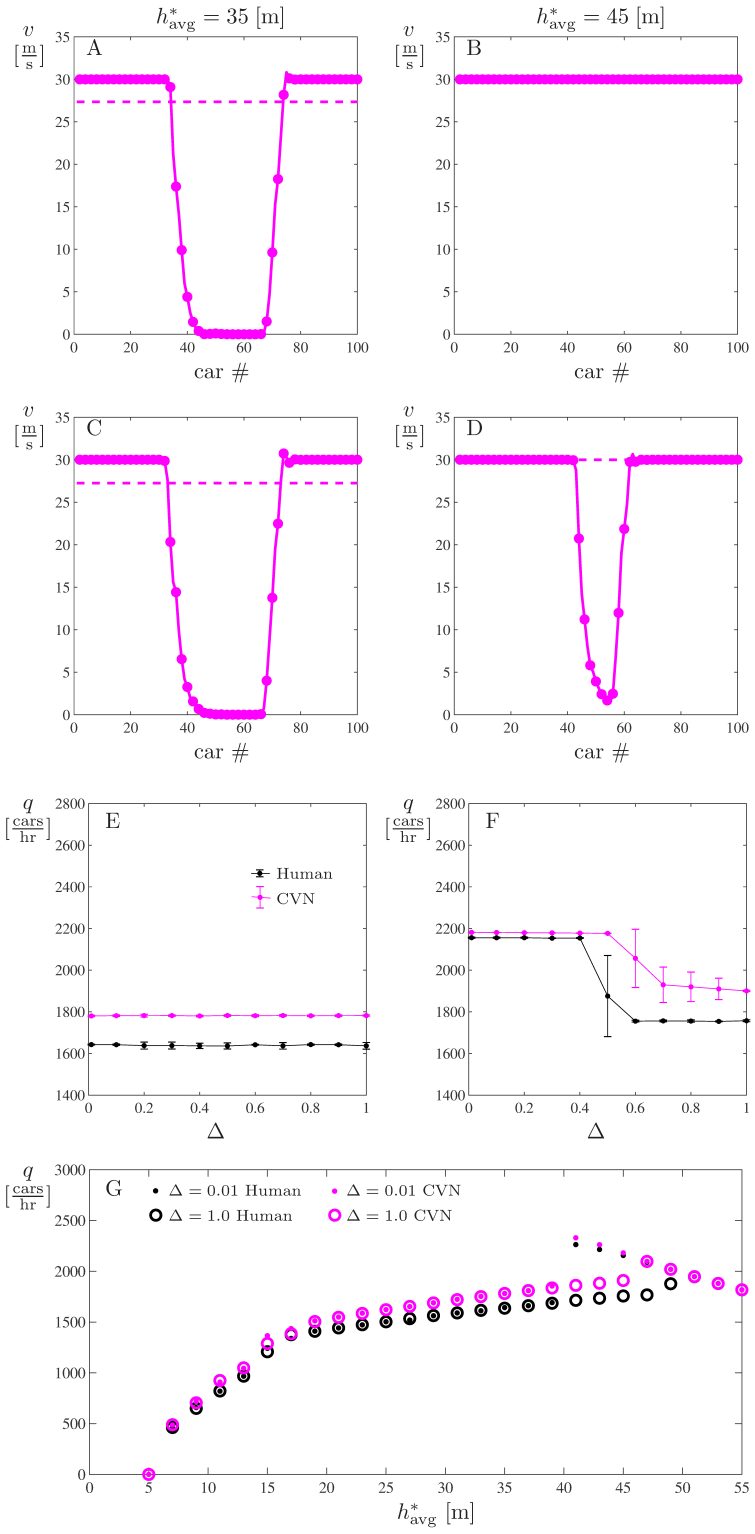

Figure 6.3: Behavior of a network with 100% CV penetration and 30% CAV of CV penetration (70% CHVs and 30% CAVs) with the CAVs using nearest neighbor feedback with $\kappa = 1.0$ [1/s] range policy (left). Same notation is used as in Figure 6.2.

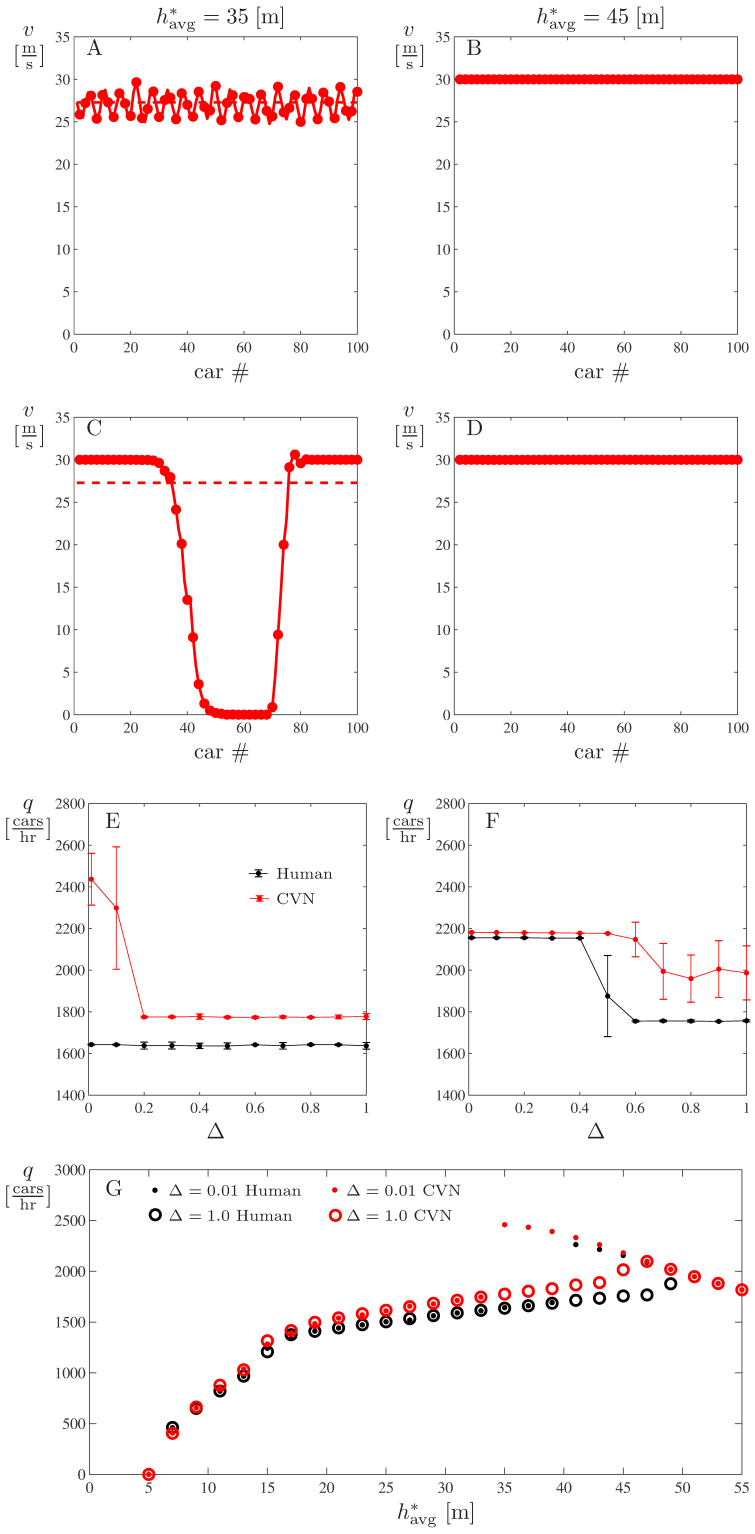

Figure 6.4: Behavior of a network with 100% CV penetration and 30% CAV of CV penetration (70% CHVs and 30% CAVs) with the CAVs using long-range feedback with $\kappa = 1.0$ [1/s] range policy. Same notation is used as in Figure 6.2.

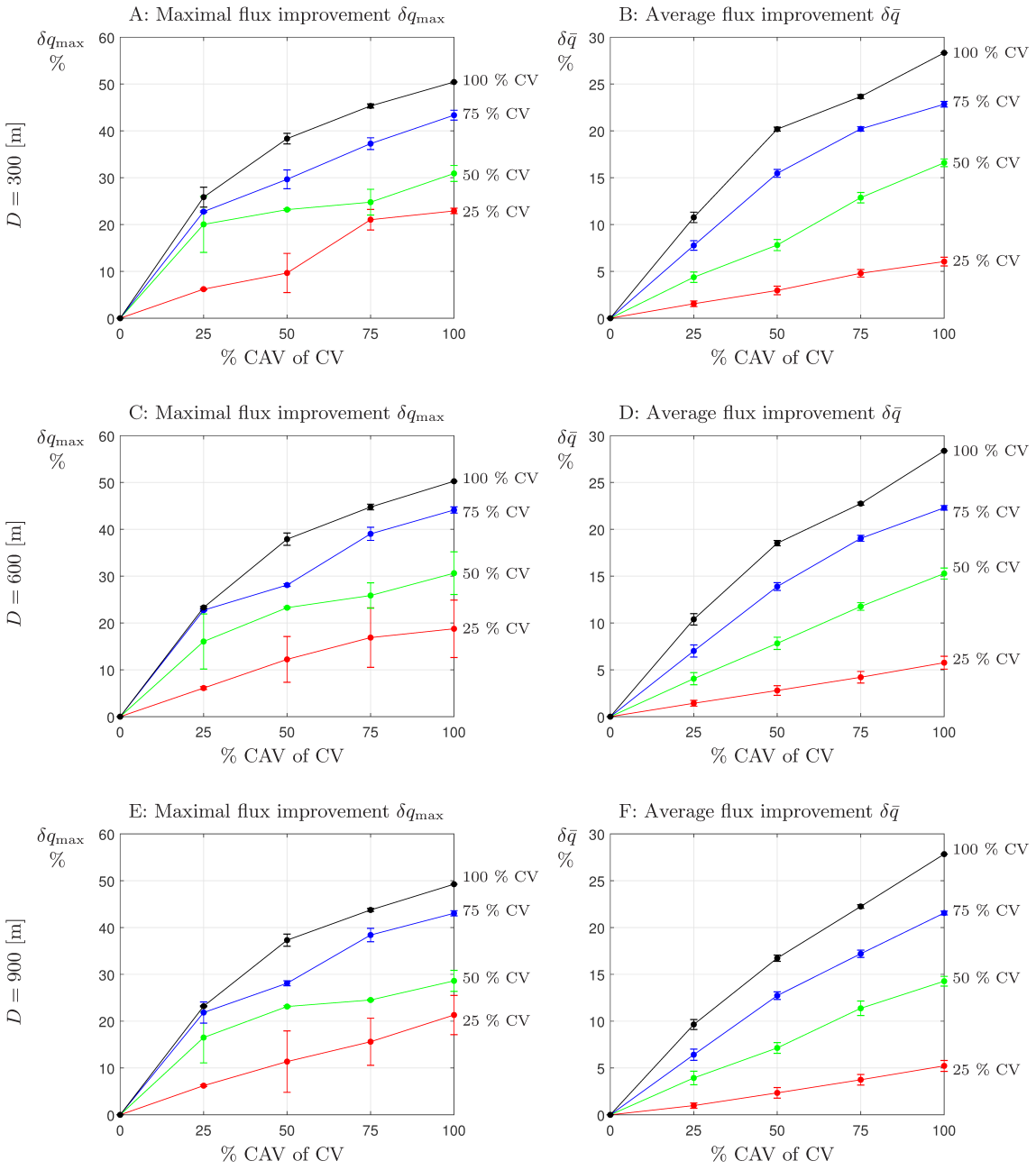

Figure 6.5: Penetration study of connected vehicle network with CAV's using long-range feedback A: $\delta q_{\max}$ B: $\delta \bar{q}$ calculated between $h_{\min} = 25$ [m] and $h_{\max} = 49$ [m] C, D: Penetration study for $D = 600$, with the same notation as A, B. D,E:Penetration study for $D = 900$, with the same notation as A, B.

CHAPTER 7

Conclusions

In this dissertation we examined the impact of vehicle-to-vehicle communication on traffic flow using rigorous analytical methods, large scale numerical simulations, and also small scale experiments with real connected and connected automated vehicles.

First we designed and tuned a car following controller of a connected automated vehicle that we developed to follow a connected human driven vehicle. Then we performed experiments with a small scale connected vehicle network consisting of the connected automated vehicle and two connected human-driven vehicles to observe the effect of n-earest neighbor feedback and long-range feedback on traffic patterns. These experiments showed us two important implications; first is that using long-range feedback to control the connected automated vehicle gives significant benefits in stability and throughput of the connected vehicle network, and second that the car following models do a good job in replicating the dynamics of the vehicles as well as the dynamics of the connected vehicle network.

This motivated us to develop rigorous analytical methods to investigate large scale traffic patterns in vehicle networks as well as how connected automated vehicles can influence these patterns. First, motivated by the nonlinearity of car following we developed a network-based methodology to decouple the nonlinear normal modes in a system possessing cyclic symmetry. This method allowed us to perform bifurcation analysis on a conventional vehicle network consisting of human driven vehicles, and observe the emerging traffic patterns. After baselining the performance of the conventional vehicle network, we sought to analytically evaluate the impact of adding connected and connected automated vehicles into the network.

These results inspired us to develop a network-based method of decoupling modes for dynamical systems with acyclic symmetry. Using this method we were able to get nontrivial

insight about the effects of adding different connected and connected automated vehicle configurations to the network. We showed that by appropriately gauging the gains, V2V link lengths, as well as the positioning of connected and automated vehicles, we could benefit the stability of uniform flow.

To confirm the benefits of the wireless connectivity we performed simulations of large connected vehicle networks, where we included realistic effects such as delays, discrete time dynamics of connected automated vehicles, vehicle acceleration limits, as well as an ad-hoc environment where individual vehicles were not aware of the connected vehicle network structure. We demonstrated that in order for the connected automated vehicles to significantly improve traffic flow in the connected vehicle network at low penetration, the connected automated vehicles must use information from beyond-line-of-sight vehicles for long-range feedback. In a network including with automated vehicles that use using nearest-neighbor feedback no significant benefits to flux were observed. If however the same number of connected automated vehicles are included that respond to connected vehicles via long-range feedback, significant improvements in flux over human driven traffic are realized.

Furthermore our study of the effects of different penetrations of connected vehicles and connected automated vehicles using long-range feedback demonstrates that significant benefits for all traffic densities can be observed when only a few vehicles are connected automated, and these vehicles benefit to the flux grows with the % of connected human driven vehicles in the network. That is increasing the penetration of connected human driven vehicles would enable a small percentage of connected automated vehicles (on the order of $10-20$ % out of all the cars) to significantly improve traffic flow. Given that full connectivity can be easily achieved by a government mandate, such as the one proposed in 2016 [20], and-off-the-shelf devices can readily be retrofitted to conventional human-driven vehicles to make them connected [28, 11] these significant improvements can be viable in the near future.

Furthermore, our penetration study has demonstrated to achieve the significant benefits outlined above, connected automated vehicles do not need to look beyond several hundreds of meters. In particular, having reliable communication beyond 300 [m] was shown not to give significant benefits to flux at the considered penetrations of connected and connected automated vehicles. One implication is that while the emerging cellular V2X (C-V2X) technology promises higher range than DSRC, DSRC is sufficient to improve the flux of

connected vehicle networks at partial connected vehicle and connected automated vehicle penetrations. Given the fact that DSRC has already been successfully tested and deployed in connected vehicle by several manufacturers [40], benefits to traffic flux can be readily realized provided the deployment of connected automated vehicles with longitudinally controlled motion.

In addition to looking at the effects of connected and automated vehicles on mobility, one can extend the framework developed in this dissertation to look at other key performance metrics such as fuel economy and driver comfort. When considering such performance metrics it would be important to distinguish and consider both the benefits reaped by the individual vehicles as well as the benefits for the entire connected vehicle network. This way we can assess the customers' incentive behind adopting connected automated vehicles as well as the global benefits once a critical penetration has been reached.

Lastly experimental and simulation frameworks developed in this work would allow us to evaluate any other potential control strategies for connected automated vehicles. For instance, with the emergence of reinforcement learning as a technique for control of connected automated vehicles with promising initial simulation results in [106, 44, 101], it would be interesting to evaluate these algorithms on real vehicles and using large scale simulations to see how they compare in reducing congestion and increasing traffic flow in mixed penetration environments.

APPENDIX A

Analytical plant and string stability conditions

The car following equations (3.1 3.2) can be discretized with a timestep Δt equal to the V2V message frequency, provided that the timestep Δt is a factor of the delay, i.e., $\tau_a = \gamma \Delta t$ where γ is a real number

$$\begin{aligned} h(t) &= h(t_k) + \int_{t_k}^{t} v_L(\tilde{t})\mathrm{d}\tilde{t} - v(t_k)(t-t_k) - \frac{1}{2} f_{sat}(u(t_{k-\gamma}))(t-t_k)^2, \\ v(t_{k+1}) &= v(t_k) + \Delta t \; f_{sat}\big(u(t_{k-\gamma})\big), \end{aligned} \tag{A.1}$$

If we define

$$\mathbf{x}(k) = \begin{bmatrix} h(k) \\ v(k) \end{bmatrix} = \begin{bmatrix} h(t_k) \\ v(t_k) \end{bmatrix}, \tag{A.2}$$

we can write

$$\begin{aligned} \begin{bmatrix} h(k+1) \\ v(k+1) \end{bmatrix} &= \begin{bmatrix} 1 & -\Delta t \\ 0 & 1 \end{bmatrix} \begin{bmatrix} h(k) \\ v(k) \end{bmatrix} + \begin{bmatrix} 0 & \frac{\Delta t^2}{2}(k_P + k_V) \\ 0 & -\Delta t(k_P + k_V) \end{bmatrix} \begin{bmatrix} h(k-\gamma) \\ v(k-\gamma) \end{bmatrix} \\ &+ \begin{bmatrix} -\frac{\Delta t^2}{2} k_P \\ \Delta t k_P \end{bmatrix} V(h(k-\gamma)) + \begin{bmatrix} -\frac{\Delta t^2}{2} k_V \\ \Delta t k_V \end{bmatrix} W(v_L(k-\gamma)) + \begin{bmatrix} \int_{t_k}^{t_{k+1}} v_L(\tilde{t})\mathrm{d}\tilde{t} \\ 0 \end{bmatrix}, \end{aligned} \tag{A.3}$$

The uniform flow condition (2.18,2.19) can be re-defined for the discrete equations above as

$$v_L(t) \equiv v^* \quad \Rightarrow \quad v_L(k) \equiv v^*, \tag{A.4}$$

$$h(t) \equiv h^* \quad \Rightarrow \quad h(k) \equiv h^*, \tag{A.5}$$

$$v(t) \equiv v^* \quad \Rightarrow \quad v(k) \equiv v^*, \tag{A.6}$$

where $v^* = V(h^*)$ and $h_{\mathrm{st}} < h^* < h_{\mathrm{go}}$, in the linear regime of the range policy (2.6). We can linearize (A.3) about this uniform flow by defining perturbations

$$\tilde{v}_{\mathrm{L}}(k) = v_{\mathrm{L}}(k) - v^*, \tag{A.7}$$

$$\tilde{\mathbf{x}}(k) = \mathbf{x}(k) - \mathbf{x}^*, \tag{A.8}$$

where $\mathbf{x}^* = [h^*, v^*]^{\mathrm{T}}$. We can also use the approximations

$$\int_{t_k}^{t_{k+1}} v_{\mathrm{L}}(\tilde{t})\mathrm{d}\tilde{t} \approx \frac{v_{\mathrm{L}}(t_{k+1}) + v_{\mathrm{L}}(t_k)}{2}\Delta t\,, \tag{A.9}$$

$$\int_{t_k}^{t_{k+1}} \tilde{v}_{\mathrm{L}}(\tilde{t})\mathrm{d}\tilde{t} \approx \frac{\tilde{v}_{\mathrm{L}}(t_{k+1}) + \tilde{v}_{\mathrm{L}}(t_k)}{2}\Delta t\,, \tag{A.10}$$

for the integrals which yields

$$\tilde{\mathbf{x}}(k+1) = \mathbf{A}_0\tilde{\mathbf{x}}(k) + \mathbf{A}_\gamma\tilde{\mathbf{x}}(k-\gamma) + \mathbf{b}_0\big(\tilde{v}_{\mathrm{L}}(k) + \tilde{v}_{\mathrm{L}}(k+1)\big) + \mathbf{b}_\gamma\tilde{v}_{\mathrm{L}} \tag{A.11}$$

Where

$$\mathbf{A}_0 = \begin{bmatrix} 1 & -\Delta t \\ 0 & 1 \end{bmatrix}, \quad \mathbf{A}_\gamma = \begin{bmatrix} -\frac{(\Delta t)^2}{2}a\kappa & \frac{(\Delta t)^2}{2}(a+b) \\ \Delta t a\kappa & -\Delta t(a+b) \end{bmatrix}, \quad \mathbf{b}_\gamma = b\begin{bmatrix} -\frac{(\Delta t)^2}{2} \\ \Delta t \end{bmatrix}, \quad \mathbf{b}_0 = \frac{\Delta}{2}\begin{bmatrix} 1 \\ 0 \end{bmatrix}, \tag{A.12}$$

If we define $\hat{\mathbf{x}}(k) = [\tilde{x}(k), \ldots, \tilde{x}(k-\gamma)]$, we can write the system in standard state space form

$$\hat{\mathbf{x}}(k+1) = \hat{\mathbf{A}}\hat{\mathbf{x}}(k) + \hat{\mathbf{B}}_\gamma v_{\mathrm{L}}(k-\gamma) + \hat{\mathbf{B}}_0\big(v_{\mathrm{L}}(k) + v_{\mathrm{L}}(k+1)\big) \tag{A.13}$$

where

$$\hat{\mathbf{A}} = \begin{bmatrix} \mathbf{A}_0 & \mathbf{0} & \cdots & \mathbf{0} & \mathbf{A}_\gamma \\ \mathbf{I} & \mathbf{0} & \cdots & \cdots & \mathbf{0} \\ \vdots & \ddots & & & \vdots \\ \vdots & & \ddots & & \vdots \\ \mathbf{0} & \cdots & \cdots & \mathbf{I} & \mathbf{0} \end{bmatrix}, \quad \hat{\mathbf{B}}_0 = \begin{bmatrix} \mathbf{b}_0 \\ \mathbf{0} \\ \vdots \\ \vdots \\ \mathbf{0} \end{bmatrix}, \quad \hat{\mathbf{B}}_\gamma = \begin{bmatrix} \mathbf{b}_\gamma \\ \mathbf{0} \\ \vdots \\ \vdots \\ \mathbf{0} \end{bmatrix} \tag{A.14}$$

The transfer function between v_{L} and v may then be obtained as

$$T(z) \;=\; \hat{\mathbf{C}}\left(z\hat{\mathbf{I}} - \hat{\mathbf{A}}\right)^{-1}\left(z^{-\gamma}\hat{\mathbf{B}}_\gamma + (1+z)\hat{\mathbf{B}}_0\right) \;=\; \frac{\hat{\mathbf{C}}\,\mathrm{adj}\left(z\hat{\mathbf{I}} - \hat{\mathbf{A}}\right)\left(z^{-\gamma}\hat{\mathbf{B}}_\gamma + (1+z)\hat{\mathbf{B}}_0\right)}{\det\left(z\hat{\mathbf{I}} - \hat{\mathbf{A}}\right)}, \tag{A.15}$$

To make sure that the CAV is able to attenuate velocity fluctuations coming from the leading vehicle it is important to ensure **string stability** of the connected automated vehicle [94, 26, 109]. This can be formulated as

$$|T(e^{i\omega\Delta t})| < 1\,, \quad \text{for} \quad 0 < \omega < \frac{2\pi}{\Delta t}\,, \tag{A.16}$$

It can be shown that this criterion is equivalent to the one obtained from a continuous time delay system

$$\begin{aligned} \dot{h}(t) &= v_{\mathrm{L}}(t) - v(t)\,, \\ \dot{v}(t) &= f_{\mathrm{sat}}\Big(a\big(V(h(t-\bar{\tau})) - v(t-\bar{\tau})\big) + b\big(W(v_{\mathrm{L}}(t-\bar{\tau})) - v(t-\bar{\tau})\big)\Big)\,, \end{aligned} \tag{A.17}$$

where $\bar{\tau} = \tau_{\mathrm{a}} + \frac{\Delta t}{2}$. In other words, to account for the delay due to zero-order hold between V2V packet deliveries, it is sufficient to add a factor of half the timestep. In [26] is is shown that with the automated car following dynamics (A.17) with the piecewise linear range policy (2.5,2.6) shown in Figure 2.2 C, the string stability boundaries are parameterized by ω_{cr}, the frequency at which string stability is lost:

$$\begin{aligned} \alpha &= K_1 \pm \sqrt{K_1^2 + K_2}\,, \\ \beta &= \frac{\omega_{\mathrm{cr}} + \alpha\kappa\bar{\tau}\sin(\omega_{\mathrm{cr}}\bar{\tau})}{\sin(\omega_{\mathrm{cr}}\bar{\tau}) + \omega_{\mathrm{cr}}\bar{\tau}\cos(\omega_{\mathrm{cr}}\bar{\tau})} - \alpha\,, \end{aligned} \tag{A.18}$$

and

$$\begin{aligned} K_1 &= \frac{\omega_{\mathrm{cr}}(\kappa\bar{\tau} - 1) + \kappa\sin(\omega_{\mathrm{cr}}\bar{\tau})\cos(\omega_{\mathrm{cr}}\bar{\tau})}{(2\kappa\bar{\tau} - 1)\sin(\omega_{\mathrm{cr}}\bar{\tau}) - \omega_{\mathrm{cr}}\bar{\tau}\sin(\omega_{\mathrm{cr}}\bar{\tau})}, \\ K_2 &= \frac{\omega_{\mathrm{cr}}^2\big(\sin(\omega_{\mathrm{cr}}\bar{\tau}) - \omega_{\mathrm{cr}}\bar{\tau}\cos(\omega_{\mathrm{cr}}\bar{\tau})\big)}{(2\kappa\bar{\tau} - 1)\sin(\omega_{\mathrm{cr}}\bar{\tau}) - \omega_{\mathrm{cr}}\bar{\tau}\sin(\omega_{\mathrm{cr}}\bar{\tau})}. \end{aligned} \tag{A.19}$$

These analytic boundaries allow us to account for the uncertainty in delay τ. We plot the plant and string stability boundaries for $\bar{\tau} = 0.55$, 0.6, 0.65, 0.7 s (which is the range of communication and actuation delays observed for the connected automated vehicle with packet loss) in Figure 3.4.

APPENDIX B

Model matching car-following models to human data

To show that the traffic patterns observed in the experiments can be reproduced by car following models, we select the parameters for the human car-following model (2.3,2.5,2.7) via a two-step model matching process.

First we fit the range policy (2.5,2.7) to the experimental data to find $h_{\mathrm{st},i}$, $h_{\mathrm{go},i}$, and $v_{\max,i}$. To do this we select segments where the system is close to a uniform flow with vehicles traveling at roughly constant speed while maintaining constant headways. For example, see the first column with $\kappa = 0.6$ [1/s] nearest-neighbor feedback and $\kappa = 1$ [1/s] long-range feedback scenarios in Figure 3.6. The headways and velocities corresponding to these steady states are plotted as grey dots in Figures 2.2 B, C for vehicles 1 and 2, respectively. The blue curves correspond to the fitted range policies, with the parameters given in the first two rows of Table 2.1.

Second we select the appropriate gains α_i, β_i and time delay τ_i for the human drivers in (2.3). For simplicity, we assume both human drives have similar gains and delays, i.e., $\alpha_i = \alpha_{\mathrm{h}}, \beta_i = \beta_{\mathrm{h}}, \tau_i = \tau_{\mathrm{h}}$, but our method can be generalized to the scenario when these parameters are different for each driver. We select the gains and delays by minimizing two cost functions over a range of α_{h}, β_{h} and τ_{h}.

The first cost function calculates the sum of squared differences between the measured and simulated headways and velocities for all cars:

$$J_{\mathrm{car}}(\alpha_{\mathrm{h}}, \beta_{\mathrm{h}}, \tau_{\mathrm{h}}) = \frac{1}{t_{\mathrm{end}} - t_{\mathrm{st}}} \sum_{i=1}^{3} \int_{t_{\mathrm{st}}}^{t_{\mathrm{end}}} \left(h_i^{\mathrm{m}}(t) - h_i(t) \right)^2 + C \left(v_i^{\mathrm{m}}(t) - v_i(t) \right)^2 \mathrm{d}t. \qquad \text{(B.1)}$$

This cost was averaged for all 18 runs (8 for $\kappa = 0.6$ [1/s] and 5 for $\kappa = 1.0$ [1/s]). The superscript "m" indicates measured quantities, whereas the unsubscripted headways and velocities denote data obtained by simulating the network Figure 3.5 B starting from the same initial condition. Here C is a constant, which we set to 1 [s^2].

The second cost function seeks to match the traffic patterns between the measurements and simulations:

$$J_{\text{trf}}(\alpha_{\text{h}}, \beta_{\text{h}}, \tau_{\text{h}}) = \left(\Delta v^{\text{m}} - \Delta v\right)^2, \tag{B.2}$$

where

$$\Delta v = \frac{1}{t_{\text{set}}} \int_{t_{\text{set}}}^{t_{\text{f}}} \max_{i,j=1,2,3} |v_i(t) - v_j(t)| \text{d}t, \tag{B.3}$$

gives the average speed difference between the fastest and the slowest moving vehicle in the connected vehicle network taken after time t_{set} when the network settled down to either uniform flow or steady oscillations. More precisely, for the experiments this period of time is taken as a time segment from t_{set} to t_{f} of at least 10 seconds where the trajectories either approach uniform flow, or exhibit constant amplitude oscillations. For the simulation results this segment is taken as the last 10 seconds of the simulation ($t_{\text{f}} = t_{\text{set}} + 10$). Intuitively small Δv correspond to the network being close to uniform flow, whereas large Δv correspond to traffic congestion [22, 66, 8]. Again, this cost was averaged for all 18 runs,and the superscripts are used to distinguish experimental and simulated quantities as in (B.1).

We select the gains α_{h}, β_{h} and the delay τ_{h} for which the values of both of the above cost functions are sufficiently small. For the 18 runs considered we obtained $\alpha_{\text{h}} = 0.14\ [1/\text{s}]$, $\beta_{\text{h}} = 0.54\ [1/\text{s}]$ and $\tau_{\text{h}} = 1.0\ [\text{s}]$. We show the simulation results with these parameters for $h^*_{\text{avg}} = 15\ [\text{m}]$ in the second column of Figure 3.6. Indeed, the simulations reproduce the experiments with high accuracy in the three scenarios.

APPENDIX C

Simplification of Cubic Terms

Before applying the cubic near-identity transformation (4.46) we need to express all the cubic terms of (4.44) using multiples of two circulant matrices. However, the cubic term $\hat{\mathfrak{L}}^{(\beta)}\left(\hat{\mathbf{S}}_b\big(\hat{\mathbf{\Psi}}(\hat{\mathbf{u}})\hat{\mathbf{u}}\big)\right)\hat{\mathbf{K}}_b^{(\beta)}\,\hat{\mathbf{u}}$ does not appear to have such structure. By spelling out the components corresponding to the dynamics of mode k (in other words the $k+1$-st row pair) we obtain

$$\Bigg[\sum_{b=0,1}\sum_{\beta=1,2}\hat{\mathfrak{L}}^{(\beta)}\big(\hat{\mathbf{S}}_b(\hat{\mathbf{\Psi}}(\hat{\mathbf{u}})\hat{\mathbf{u}})\big)\hat{\mathbf{K}}_b^{(\beta)}\hat{\mathbf{u}}\Bigg]_k = \sum_{j=0}^{N-1}\sum_{\ell=0}^{N-1}\sum_{b=0,1}\sum_{\beta=1,2}\sum_{\delta=1,2}\begin{bmatrix}\mathrm{e}^{\mathrm{i}\frac{2\pi b(k-\ell)}{N}}\Big[\partial_b^{(\beta)}\,\kappa_{\ell 0}^{(1\,\delta)}\Big]^*\Big(\overline{\psi}_{m(\ell)\,j}^{(\beta\,1)}\cdot\mathbf{u}_{f_{m(\ell)\,j}}u_j^{(1)}+\overline{\psi}_{m(\ell)\,j}^{(\beta\,2)}\cdot\mathbf{u}_{f_{m(\ell)\,j}}u_j^{(2)}\Big)u_\ell^{(\delta)}\\ \mathrm{e}^{\mathrm{i}\frac{2\pi b(k-\ell)}{N}}\Big[\partial_b^{(\beta)}\,\kappa_{\ell 0}^{(2\,\delta)}\Big]^*\Big(\overline{\psi}_{m(\ell)\,j}^{(\beta\,1)}\cdot\mathbf{u}_{f_{m(\ell)\,j}}u_j^{(1)}+\overline{\psi}_{m(\ell)\,j}^{(\beta\,2)}\cdot\mathbf{u}_{f_{m(\ell)\,j}}u_j^{(2)}\Big)u_\ell^{(\delta)}\end{bmatrix}, \tag{C.1}$$

where $m(\ell)$ is given as

$$m(\ell)=f_{k\ell}=\begin{cases}k-\ell & \text{if}\quad k\geq\ell,\\ N+k-\ell & \text{if}\quad k<\ell.\end{cases} \tag{C.2}$$

If we consider a change of indexes $\sigma=f_{k\ell}$ we get

$$\Bigg[\sum_{b=0,1}\hat{\mathfrak{L}}^{(\beta)}\big(\hat{\mathbf{S}}_b(\hat{\mathbf{\Psi}}(\hat{\mathbf{u}})\hat{\mathbf{u}})\big)\hat{\mathbf{K}}_b^{(\beta)}\hat{\mathbf{u}}\Bigg]_k = \sum_{j=0}^{N-1}\sum_{\sigma=0}^{N-1}\sum_{b=0,1}\sum_{\beta=1,2}\sum_{\delta=1,2}\begin{bmatrix}\mathrm{e}^{\mathrm{i}\frac{2\pi b\sigma}{N}}\Big[\partial_b^{(\beta)}\,\kappa_{f_{k\sigma}0}^{(1\,\delta)}\Big]^*\Big(\overline{\psi}_{\sigma\,j}^{(\beta\,1)}\cdot\mathbf{u}_{f_{\sigma\,j}}u_j^{(1)}+\overline{\psi}_{\sigma\,j}^{(\beta\,2)}\cdot\mathbf{u}_{f_{\sigma\,j}}u_j^{(2)}\Big)u_{f_{k\sigma}}^{(\delta)}\\ \mathrm{e}^{\mathrm{i}\frac{2\pi b\sigma}{N}}\Big[\partial_b^{(\beta)}\,\kappa_{f_{k\sigma}0}^{(2\,\delta)}\Big]^*\Big(\overline{\psi}_{\sigma\,j}^{(\beta\,1)}\cdot\mathbf{u}_{f_{\sigma\,j}}u_j^{(1)}+\overline{\psi}_{\sigma\,j}^{(\beta\,2)}\cdot\mathbf{u}_{f_{\sigma\,j}}u_j^{(2)}\Big)u_{f_{k\sigma}}^{(\delta)}\end{bmatrix}. \tag{C.3}$$

Similarly, the k-th modal component of $\hat{\mathfrak{L}}^{(\beta)}\big(\hat{\mathbf{S}}_b(\hat{\mathbf{u}})\big)\hat{\mathbf{K}}_b^{(\beta)}\hat{\mathbf{\Psi}}(\hat{\mathbf{u}})\hat{\mathbf{u}}$ can be expanded as

$$\Bigg[\sum_{b=0,1}\sum_{\beta=1,2}\hat{\mathfrak{L}}^{(\beta)}\big(\hat{\mathbf{S}}_b(\hat{\mathbf{u}})\big)\hat{\mathbf{K}}_b^{(\beta)}\hat{\mathbf{\Psi}}(\hat{\mathbf{u}})\hat{\mathbf{u}}\Bigg]_k = \sum_{j=0}^{N-1}\sum_{\ell=0}^{N-1}\sum_{b=0,1}\sum_{\delta=1,2}\sum_{\beta=1,2}\begin{bmatrix} \mathrm{e}^{\mathrm{i}\frac{2\pi b(k-\ell)}{N}}\Big[\partial_b^{(\beta)}\,\boldsymbol{\kappa}_{\ell 0}^{(1\,\delta)}\Big]^*\Big(\overline{\boldsymbol{\psi}}_{\ell j}^{(\delta\,1)}\cdot\mathbf{u}_{f_{\ell j}}u_j^{(1)}+\overline{\boldsymbol{\psi}}_{\ell j}^{(\delta\,2)}\cdot\mathbf{u}_{f_{\ell j}}u_j^{(2)}\Big)u_{f_{k\ell}}^{(\beta)} \\ \mathrm{e}^{\mathrm{i}\frac{2\pi b(k-\ell)}{N}}\Big[\partial_b^{(\beta)}\,\boldsymbol{\kappa}_{\ell 0}^{(2\,\delta)}\Big]^*\Big(\overline{\boldsymbol{\psi}}_{\ell j}^{(\delta\,1)}\cdot\mathbf{u}_{f_{\ell j}}u_j^{(1)}+\overline{\boldsymbol{\psi}}_{\ell j}^{(\delta\,2)}\cdot\mathbf{u}_{f_{\ell j}}u_j^{(2)}\Big)u_{f_{k\ell}}^{(\beta)} \end{bmatrix}. \tag{C.4}$$

If we re-label the δ and β we obtain

$$\Bigg[\sum_{b=0,1}\sum_{\beta=1,2}\hat{\mathfrak{L}}^{(\beta)}\big(\hat{\mathbf{S}}_b(\hat{\mathbf{u}})\big)\hat{\mathbf{K}}_b^{(\beta)}\hat{\mathbf{\Psi}}(\hat{\mathbf{u}})\hat{\mathbf{u}}\Bigg]_k = \sum_{j=0}^{N-1}\sum_{\ell=0}^{N-1}\sum_{b=0,1}\sum_{\beta=1,2}\sum_{\delta=1,2}\begin{bmatrix} \mathrm{e}^{\mathrm{i}\frac{2\pi b(k-\ell)}{N}}\Big[\partial_b^{(\delta)}\,\boldsymbol{\kappa}_{\ell 0}^{(1\,\beta)}\Big]^*\Big(\overline{\boldsymbol{\psi}}_{\ell j}^{(\beta\,1)}\cdot\mathbf{u}_{f_{\ell j}}u_j^{(1)}+\overline{\boldsymbol{\psi}}_{\ell j}^{(\beta\,2)}\cdot\mathbf{u}_{f_{\ell j}}u_j^{(2)}\Big)u_{f_{k\ell}}^{(\delta)} \\ \mathrm{e}^{\mathrm{i}\frac{2\pi b(k-\ell)}{N}}\Big[\partial_b^{(\delta)}\,\boldsymbol{\kappa}_{\ell 0}^{(2\,\beta)}\Big]^*\Big(\overline{\boldsymbol{\psi}}_{\ell j}^{(\beta\,1)}\cdot\mathbf{u}_{f_{\ell j}}u_j^{(1)}+\overline{\boldsymbol{\psi}}_{\ell j}^{(\beta\,2)}\cdot\mathbf{u}_{f_{\ell j}}u_j^{(2)}\Big)u_{f_{k\ell}}^{(\delta)} \end{bmatrix}. \tag{C.5}$$

Considering (C.3) and (C.5) for the same values of j, β, and δ, and for $\sigma=\ell$ we can show that

$$\sum_{b=0,1}\mathrm{e}^{\mathrm{i}\frac{2\pi b\sigma}{N}}\Big[\partial_b^{(\beta)}\,\boldsymbol{\kappa}_{f_{k\sigma}0}^{(1\,\delta)}\Big]^* = \sum_{b=0,1}\mathrm{e}^{\mathrm{i}\frac{2\pi b(k-\ell)}{N}}\Big[\partial_b^{(\delta)}\,\boldsymbol{\kappa}_{\ell 0}^{(1\,\beta)}\Big]^*, \tag{C.6}$$

and hence (C.3) and (C.5) are equal. This means that (4.44) and (4.45) are identical.

APPENDIX D

Cubic Near Identity Coefficients (Left Hand Side)

The coefficient vector $\tilde{\mathbf{b}}_{kj\ell}$ in (4.51) is given by

$$\tilde{\mathbf{b}}_{kj\ell} = \begin{bmatrix} \gamma_{kj}^{(111)}\,\phi_{j\ell}^{(111)} + \gamma_{kj}^{(121)}\,\phi_{j\ell}^{(211)} \\ \gamma_{kj}^{(111)}\,\phi_{j\ell}^{(112)} + \gamma_{kj}^{(121)}\,\phi_{j\ell}^{(212)} \\ \gamma_{kj}^{(112)}\,\phi_{j\ell}^{(111)} + \gamma_{kj}^{(122)}\,\phi_{j\ell}^{(211)} \\ \gamma_{kj}^{(112)}\,\phi_{j\ell}^{(112)} + \gamma_{kj}^{(122)}\,\phi_{j\ell}^{(212)} \\ \gamma_{kj}^{(111)}\,\phi_{j\ell}^{(121)} + \gamma_{kj}^{(121)}\,\phi_{j\ell}^{(221)} \\ \gamma_{kj}^{(111)}\,\phi_{j\ell}^{(122)} + \gamma_{kj}^{(121)}\,\phi_{j\ell}^{(222)} \\ \gamma_{kj}^{(112)}\,\phi_{j\ell}^{(121)} + \gamma_{kj}^{(122)}\,\phi_{j\ell}^{(221)} \\ \gamma_{kj}^{(112)}\,\phi_{j\ell}^{(122)} + \gamma_{kj}^{(122)}\,\phi_{j\ell}^{(222)} \\ \gamma_{kj}^{(211)}\,\phi_{j\ell}^{(111)} + \gamma_{kj}^{(221)}\,\phi_{j\ell}^{(211)} \\ \gamma_{kj}^{(211)}\,\phi_{j\ell}^{(112)} + \gamma_{kj}^{(221)}\,\phi_{j\ell}^{(212)} \\ \gamma_{kj}^{(212)}\,\phi_{j\ell}^{(111)} + \gamma_{kj}^{(222)}\,\phi_{j\ell}^{(211)} \\ \gamma_{kj}^{(212)}\,\phi_{j\ell}^{(112)} + \gamma_{kj}^{(222)}\,\phi_{j\ell}^{(212)} \\ \gamma_{kj}^{(211)}\,\phi_{j\ell}^{(121)} + \gamma_{kj}^{(221)}\,\phi_{j\ell}^{(221)} \\ \gamma_{kj}^{(211)}\,\phi_{j\ell}^{(122)} + \gamma_{kj}^{(221)}\,\phi_{j\ell}^{(222)} \\ \gamma_{kj}^{(212)}\,\phi_{j\ell}^{(121)} + \gamma_{kj}^{(222)}\,\phi_{j\ell}^{(221)} \\ \gamma_{kj}^{(212)}\,\phi_{j\ell}^{(122)} + \gamma_{kj}^{(222)}\,\phi_{j\ell}^{(222)} \end{bmatrix}, \tag{D.1}$$

where the constants $\gamma_{kj}^{(\cdots)}$ and $\phi_{j\ell}^{(\cdots)}$ are defined in (4.47).

APPENDIX E

General Cubic Coefficients (Right Hand Side)

The coefficient vector $\tilde{\mathbf{c}}_{k\,j\,\ell}$ in (4.51) is given by

$$\tilde{\mathbf{c}}_{k\,j\,\ell} = \begin{bmatrix} \left(\sum_{\beta=1,2} \psi_{j\ell}^{(\beta\,1\,1)} (\partial_0^{(\beta)} + \mathrm{e}^{\mathrm{i}\frac{2\pi j}{N}} \partial_1^{(\beta)})\right) \kappa_{kj}^{(1\,1)\,*} \\ \left(\sum_{\beta=1,2} \psi_{j\ell}^{(\beta\,1\,2)} (\partial_0^{(\beta)} + \mathrm{e}^{\mathrm{i}\frac{2\pi j}{N}} \partial_1^{(\beta)})\right) \kappa_{kj}^{(1\,1)\,*} \\ \left(\sum_{\beta=1,2} \psi_{j\ell}^{(\beta\,1\,1)} (\partial_0^{(\beta)} + \mathrm{e}^{\mathrm{i}\frac{2\pi j}{N}} \partial_1^{(\beta)})\right) \kappa_{kj}^{(1\,2)\,*} \\ \left(\sum_{\beta=1,2} \psi_{j\ell}^{(\beta\,1\,2)} (\partial_0^{(\beta)} + \mathrm{e}^{\mathrm{i}\frac{2\pi j}{N}} \partial_1^{(\beta)})\right) \kappa_{kj}^{(1\,2)\,*} \\ \left(\sum_{\beta=1,2} \psi_{j\ell}^{(\beta\,2\,1)} (\partial_0^{(\beta)} + \mathrm{e}^{\mathrm{i}\frac{2\pi j}{N}} \partial_1^{(\beta)})\right) \kappa_{kj}^{(1\,1)\,*} \\ \left(\sum_{\beta=1,2} \psi_{j\ell}^{(\beta\,2\,2)} (\partial_0^{(\beta)} + \mathrm{e}^{\mathrm{i}\frac{2\pi j}{N}} \partial_1^{(\beta)})\right) \kappa_{kj}^{(1\,1)\,*} \\ \left(\sum_{\beta=1,2} \psi_{j\ell}^{(\beta\,2\,1)} (\partial_0^{(\beta)} + \mathrm{e}^{\mathrm{i}\frac{2\pi j}{N}} \partial_1^{(\beta)})\right) \kappa_{kj}^{(1\,2)\,*} \\ \left(\sum_{\beta=1,2} \psi_{j\ell}^{(\beta\,2\,2)} (\partial_0^{(\beta)} + \mathrm{e}^{\mathrm{i}\frac{2\pi j}{N}} \partial_1^{(\beta)})\right) \kappa_{kj}^{(1\,2)\,*} \\ \left(\sum_{\beta=1,2} \psi_{j\ell}^{(\beta\,1\,1)} (\partial_0^{(\beta)} + \mathrm{e}^{\mathrm{i}\frac{2\pi j}{N}} \partial_1^{(\beta)})\right) \kappa_{kj}^{(2\,1)\,*} \\ \left(\sum_{\beta=1,2} \psi_{j\ell}^{(\beta\,1\,2)} (\partial_0^{(\beta)} + \mathrm{e}^{\mathrm{i}\frac{2\pi j}{N}} \partial_1^{(\beta)})\right) \kappa_{kj}^{(2\,1)\,*} \\ \left(\sum_{\beta=1,2} \psi_{j\ell}^{(\beta\,1\,1)} (\partial_0^{(\beta)} + \mathrm{e}^{\mathrm{i}\frac{2\pi j}{N}} \partial_1^{(\beta)})\right) \kappa_{kj}^{(2\,2)\,*} \\ \left(\sum_{\beta=1,2} \psi_{j\ell}^{(\beta\,1\,2)} (\partial_0^{(\beta)} + \mathrm{e}^{\mathrm{i}\frac{2\pi j}{N}} \partial_1^{(\beta)})\right) \kappa_{kj}^{(2\,2)\,*} \\ \left(\sum_{\beta=1,2} \psi_{j\ell}^{(\beta\,2\,1)} (\partial_0^{(\beta)} + \mathrm{e}^{\mathrm{i}\frac{2\pi j}{N}} \partial_1^{(\beta)})\right) \kappa_{kj}^{(2\,1)\,*} \\ \left(\sum_{\beta=1,2} \psi_{j\ell}^{(\beta\,2\,2)} (\partial_0^{(\beta)} + \mathrm{e}^{\mathrm{i}\frac{2\pi j}{N}} \partial_1^{(\beta)})\right) \kappa_{kj}^{(2\,1)\,*} \\ \left(\sum_{\beta=1,2} \psi_{j\ell}^{(\beta\,2\,1)} (\partial_0^{(\beta)} + \mathrm{e}^{\mathrm{i}\frac{2\pi j}{N}} \partial_1^{(\beta)})\right) \kappa_{kj}^{(2\,2)\,*} \\ \left(\sum_{\beta=1,2} \psi_{j\ell}^{(\beta\,2\,2)} (\partial_0^{(\beta)} + \mathrm{e}^{\mathrm{i}\frac{2\pi j}{N}} \partial_1^{(\beta)})\right) \kappa_{kj}^{(2\,2)\,*} \end{bmatrix} + \frac{1}{6} \begin{bmatrix} (\partial_0^{(1)} + \mathrm{e}^{\mathrm{i}\frac{2\pi(k-j)}{N}} \partial_1^{(1)})(\partial_0^{(1)} + \mathrm{e}^{\mathrm{i}\frac{2\pi(j-\ell)}{N}} \partial_1^{(1)}) \kappa_{\ell 0}^{(1\,1)\,*} \\ (\partial_0^{(1)} + \mathrm{e}^{\mathrm{i}\frac{2\pi(k-j)}{N}} \partial_1^{(1)})(\partial_0^{(2)} + \mathrm{e}^{\mathrm{i}\frac{2\pi(j-\ell)}{N}} \partial_1^{(2)}) \kappa_{\ell 0}^{(1\,1)\,*} \\ (\partial_0^{(2)} + \mathrm{e}^{\mathrm{i}\frac{2\pi(k-j)}{N}} \partial_1^{(2)})(\partial_0^{(1)} + \mathrm{e}^{\mathrm{i}\frac{2\pi(j-\ell)}{N}} \partial_1^{(1)}) \kappa_{\ell 0}^{(1\,1)\,*} \\ (\partial_0^{(2)} + \mathrm{e}^{\mathrm{i}\frac{2\pi(k-j)}{N}} \partial_1^{(2)})(\partial_0^{(2)} + \mathrm{e}^{\mathrm{i}\frac{2\pi(j-\ell)}{N}} \partial_1^{(2)}) \kappa_{\ell 0}^{(1\,1)\,*} \\ (\partial_0^{(1)} + \mathrm{e}^{\mathrm{i}\frac{2\pi(k-j)}{N}} \partial_1^{(1)})(\partial_0^{(1)} + \mathrm{e}^{\mathrm{i}\frac{2\pi(j-\ell)}{N}} \partial_1^{(1)}) \kappa_{\ell 0}^{(1\,2)\,*} \\ (\partial_0^{(1)} + \mathrm{e}^{\mathrm{i}\frac{2\pi(k-j)}{N}} \partial_1^{(1)})(\partial_0^{(2)} + \mathrm{e}^{\mathrm{i}\frac{2\pi(j-\ell)}{N}} \partial_1^{(2)}) \kappa_{\ell 0}^{(1\,2)\,*} \\ (\partial_0^{(2)} + \mathrm{e}^{\mathrm{i}\frac{2\pi(k-j)}{N}} \partial_1^{(2)})(\partial_0^{(1)} + \mathrm{e}^{\mathrm{i}\frac{2\pi(j-\ell)}{N}} \partial_1^{(1)}) \kappa_{\ell 0}^{(1\,2)\,*} \\ (\partial_0^{(2)} + \mathrm{e}^{\mathrm{i}\frac{2\pi(k-j)}{N}} \partial_1^{(2)})(\partial_0^{(2)} + \mathrm{e}^{\mathrm{i}\frac{2\pi(j-\ell)}{N}} \partial_1^{(2)}) \kappa_{\ell 0}^{(1\,2)\,*} \\ (\partial_0^{(1)} + \mathrm{e}^{\mathrm{i}\frac{2\pi(k-j)}{N}} \partial_1^{(1)})(\partial_0^{(1)} + \mathrm{e}^{\mathrm{i}\frac{2\pi(j-\ell)}{N}} \partial_1^{(1)}) \kappa_{\ell 0}^{(2\,1)\,*} \\ (\partial_0^{(1)} + \mathrm{e}^{\mathrm{i}\frac{2\pi(k-j)}{N}} \partial_1^{(1)})(\partial_0^{(2)} + \mathrm{e}^{\mathrm{i}\frac{2\pi(j-\ell)}{N}} \partial_1^{(2)}) \kappa_{\ell 0}^{(2\,1)\,*} \\ (\partial_0^{(2)} + \mathrm{e}^{\mathrm{i}\frac{2\pi(k-j)}{N}} \partial_1^{(2)})(\partial_0^{(1)} + \mathrm{e}^{\mathrm{i}\frac{2\pi(j-\ell)}{N}} \partial_1^{(1)}) \kappa_{\ell 0}^{(2\,1)\,*} \\ (\partial_0^{(2)} + \mathrm{e}^{\mathrm{i}\frac{2\pi(k-j)}{N}} \partial_1^{(2)})(\partial_0^{(2)} + \mathrm{e}^{\mathrm{i}\frac{2\pi(j-\ell)}{N}} \partial_1^{(2)}) \kappa_{\ell 0}^{(2\,1)\,*} \\ (\partial_0^{(1)} + \mathrm{e}^{\mathrm{i}\frac{2\pi(k-j)}{N}} \partial_1^{(1)})(\partial_0^{(1)} + \mathrm{e}^{\mathrm{i}\frac{2\pi(j-\ell)}{N}} \partial_1^{(1)}) \kappa_{\ell 0}^{(2\,2)\,*} \\ (\partial_0^{(1)} + \mathrm{e}^{\mathrm{i}\frac{2\pi(k-j)}{N}} \partial_1^{(1)})(\partial_0^{(2)} + \mathrm{e}^{\mathrm{i}\frac{2\pi(j-\ell)}{N}} \partial_1^{(2)}) \kappa_{\ell 0}^{(2\,2)\,*} \\ (\partial_0^{(2)} + \mathrm{e}^{\mathrm{i}\frac{2\pi(k-j)}{N}} \partial_1^{(2)})(\partial_0^{(1)} + \mathrm{e}^{\mathrm{i}\frac{2\pi(j-\ell)}{N}} \partial_1^{(1)}) \kappa_{\ell 0}^{(2\,2)\,*} \\ (\partial_0^{(2)} + \mathrm{e}^{\mathrm{i}\frac{2\pi(k-j)}{N}} \partial_1^{(2)})(\partial_0^{(2)} + \mathrm{e}^{\mathrm{i}\frac{2\pi(j-\ell)}{N}} \partial_1^{(2)}) \kappa_{\ell 0}^{(2\,2)\,*} \end{bmatrix}. \tag{E.1}$$

APPENDIX F

Remaining quadratic terms for mode 0

In equation (4.71) $\frac{1}{2}\hat{\mathbf{R}}(\hat{\mathbf{u}})\hat{\mathbf{u}}$ represents the quadratic terms that cannot be eliminated by the near-identity transformation (4.32) when modes 1 and $N-1$ undergo a Hopf bifurcation. The only two non-zero entries in matrix $\hat{\mathbf{R}}(\hat{\mathbf{u}})$ are given by

$$[\hat{\mathbf{R}}(\hat{\mathbf{u}})]_{(1,2)} = \begin{bmatrix} 0 & 0 \\ 4q_1 \sin^2\left(\frac{\pi}{N}\right) z_{N-1}^{(1)} & 0 \end{bmatrix}, \qquad [\hat{\mathbf{R}}(\hat{\mathbf{u}})]_{(1,N)} = \begin{bmatrix} 0 & 0 \\ 4q_1 \sin^2\left(\frac{\pi}{N}\right) z_1^{(1)} & 0 \end{bmatrix}, \tag{F.1}$$

where subscripts denote the location of the block in $\hat{\mathbf{R}}(\hat{\mathbf{u}})$, and q_1 gives the value of q at the bifurcation point; cf. (4.4). Indeed, these quadratic terms correspond to the modes 1 and $N-1$ and they only appear in the dynamics of the $k=0$ mode. In the special case when $\beta = 0$ and even N the term

$$[\hat{\mathbf{R}}(\hat{\mathbf{u}})]_{(1,\frac{N}{2}+1)} = \begin{bmatrix} 0 & 0 \\ 4q_1 z_{\frac{N}{2}}^{(1)} & 0 \end{bmatrix}, \tag{F.2}$$

also remains in the equation of the $k=0$ mode due to mode $N/2$.

APPENDIX G

Quadratic near-identity coefficients for the connected vehicle example

Equations (4.77) and (4.82) contain four non-zero quadratic near identity coefficients that can be obtained by solving (4.51) for the car following model:

$$
\begin{aligned}
\psi_{21}^{(111)} &= \frac{q_1\left(\mathrm{e}^{\mathrm{i}\frac{2\pi}{N}}-1\right)^2}{2\,\Delta}\Bigg(-\left(2\,\kappa_{10}^{(21)\,*}-\kappa_{20}^{(21)\,*}\right)\left(4\,\kappa_{10}^{(21)\,*}-\kappa_{20}^{(21)\,*}\right)\\
&\quad-2\,\kappa_{10}^{(21)\,*}\left(\kappa_{10}^{(22)\,*}-\kappa_{20}^{(22)\,*}\right)\kappa_{20}^{(22)\,*}+\kappa_{20}^{(21)\,*}\,\kappa_{10}^{(22)\,*}\left(5\,\kappa_{10}^{(22)\,*}-3\,\kappa_{20}^{(22)\,*}\right)\\
&\quad-2\left(\kappa_{10}^{(22)\,*}\right)^2\left(\kappa_{10}^{(22)\,*}-\kappa_{20}^{(22)\,*}\right)\left(2\,\kappa_{10}^{(22)\,*}-\kappa_{20}^{(22)\,*}\right)\Bigg),\\
\psi_{21}^{(112)}+\psi_{21}^{(121)} &= \frac{-q_1\left(\mathrm{e}^{\mathrm{i}\frac{2\pi}{N}}-1\right)^2}{\Delta}\Bigg(4\,\kappa_{10}^{(21)\,*}\,\kappa_{10}^{(22)\,*}+\kappa_{20}^{(21)\,*}\left(\kappa_{10}^{(22)\,*}-\kappa_{20}^{(22)\,*}\right)\\
&\quad-2\,\kappa_{10}^{(22)\,*}\left(\kappa_{10}^{(22)\,*}-\kappa_{20}^{(22)\,*}\right)\left(2\kappa_{10}^{(22)\,*}-\kappa_{20}^{(22)\,*}\right)\Bigg),\\
\psi_{21}^{(122)} &= \frac{q_1\left(\mathrm{e}^{\mathrm{i}\frac{2\pi}{N}}-1\right)^2}{\Delta}\left(\left(4\,\kappa_{10}^{(21)\,*}-\kappa_{20}^{(21)\,*}\right)-\left(\kappa_{10}^{(22)\,*}-\kappa_{20}^{(22)\,*}\right)\left(2\kappa_{10}^{(22)\,*}-\kappa_{20}^{(22)\,*}\right)\right),
\end{aligned}
\tag{G.1}
$$

where the factor Δ is

$$
\begin{aligned}
\Delta &= \kappa_{20}^{(21)\,*}\left(4\,\kappa_{10}^{(21)\,*}-\kappa_{20}^{(21)\,*}\right)^2-16\,\kappa_{10}^{(22)\,*}\left(\kappa_{10}^{(22)\,*}-\kappa_{20}^{(22)\,*}\right)\left(\kappa_{10}^{(21)\,*}\right)^2\\
&\quad+4\left(2\left(\kappa_{10}^{(22)\,*}\right)^2-\left(\kappa_{20}^{(22)\,*}\right)^2\right)\kappa_{10}^{(21)\,*}\,\kappa_{20}^{(21)\,*}-\kappa_{10}^{(22)\,*}\left(5\kappa_{10}^{(22)\,*}-3\kappa_{20}^{(22)\,*}\right)\left(\kappa_{20}^{(22)\,*}\right)^2\\
&\quad+2\,\kappa_{10}^{(22)\,*}\left(\kappa_{10}^{(22)\,*}-\kappa_{20}^{(22)\,*}\right)\left(2\,\kappa_{10}^{(22)\,*}-\kappa_{20}^{(22)\,*}\right)\left(-2\,\kappa_{10}^{(21)\,*}\,\kappa_{20}^{(22)\,*}+\kappa_{20}^{(21)\,*}\,\kappa_{10}^{(22)\,*}\right),
\end{aligned}
\tag{G.2}
$$

and q_1 gives the value of q at the bifurcation point; cf. (4.4). We remark that the coefficients $\psi_{21}^{(112)}$ and $\psi_{21}^{(121)}$ do not need to be evaluated individually since (4.77,4.82) only include their sum.

APPENDIX H

Third-order approximation of modal dynamics

To obtain the third-order perturbation of the dynamics of the k-th mode $[\hat{\mathbf{D}}^{(1,2,3)}]_k^k$ for an arbitrary $i_1,\sigma_1,i_2,\sigma_2,i_3,\sigma_3$ sextuple we take the derivative of (5.44) with respect to $\varepsilon_{i_3\sigma_3}$ (denoted by ε_3) which yields

$$\begin{aligned}
&\partial_{\varepsilon_1}\partial_{\varepsilon_2}\partial_{\varepsilon_3}\left(\hat{\mathbf{J}}-\mathbf{I}_N\otimes[\hat{\mathbf{D}}]_k^k\right)[\hat{\mathbf{T}}]_k+\partial_{\varepsilon_1}\partial_{\varepsilon_2}\left(\hat{\mathbf{J}}-\mathbf{I}_N\otimes[\hat{\mathbf{D}}]_k^k\right)\partial_{\varepsilon_3}[\hat{\mathbf{T}}]_k\\
&+\partial_{\varepsilon_1}\partial_{\varepsilon_3}\left(\hat{\mathbf{J}}-\mathbf{I}_N\otimes[\hat{\mathbf{D}}]_k^k\right)\partial_{\varepsilon_2}[\hat{\mathbf{T}}]_k+\partial_{\varepsilon_2}\partial_{\varepsilon_3}\left(\hat{\mathbf{J}}-\mathbf{I}_N\otimes[\hat{\mathbf{D}}]_k^k\right)\partial_{\varepsilon_1}[\hat{\mathbf{T}}]_k\\
&+\partial_{\varepsilon_1}\left(\hat{\mathbf{J}}-\mathbf{I}_N\otimes[\hat{\mathbf{D}}]_k^k\right)\partial_{\varepsilon_2}\partial_{\varepsilon_3}[\hat{\mathbf{T}}]_k+\partial_{\varepsilon_2}\left(\hat{\mathbf{J}}-\mathbf{I}_N\otimes[\hat{\mathbf{D}}]_k^k\right)\partial_{\varepsilon_1}\partial_{\varepsilon_3}[\hat{\mathbf{T}}]_k\\
&+\partial_{\varepsilon_3}\left(\hat{\mathbf{J}}-\mathbf{I}_N\otimes[\hat{\mathbf{D}}]_k^k\right)\partial_{\varepsilon_1}\partial_{\varepsilon_2}[\hat{\mathbf{T}}]_k+\left(\hat{\mathbf{J}}-\mathbf{I}_N\otimes[\hat{\mathbf{D}}]_k^k\right)\partial_{\varepsilon_1}\partial_{\varepsilon_2}\partial_{\varepsilon_3}[\hat{\mathbf{T}}]_k=0.
\end{aligned}\tag{H.1}$$

At $\varepsilon_{i_1\sigma_1}=\varepsilon_{i_2\sigma_2}=\varepsilon_{i_3\sigma_3}=0$ we obtain

$$\begin{aligned}
&\frac{1}{6}\mathbf{I}_N\otimes\left([\hat{\mathbf{D}}^{(1,2,3)}]_k^k+[\hat{\mathbf{D}}^{(1,3,2)}]_k^k+[\hat{\mathbf{D}}^{(2,1,3)}]_k^k+[\hat{\mathbf{D}}^{(2,3,1)}]_k^k+[\hat{\mathbf{D}}^{(3,1,2)}]_k^k+[\hat{\mathbf{D}}^{(3,2,1)}]_k^k\right)\\
&=-\frac{1}{2}\mathbf{I}_N\otimes\left([\hat{\mathbf{D}}^{(1,2)}]_k^k+[\hat{\mathbf{D}}^{(2,1)}]_k^k\right)[\hat{\mathbf{T}}^{(3)}]_k-\frac{1}{2}\mathbf{I}_N\otimes\left([\hat{\mathbf{D}}^{(1,3)}]_k^k+[\hat{\mathbf{D}}^{(3,1)}]_k^k\right)[\hat{\mathbf{T}}^{(2)}]_k\\
&-\frac{1}{2}\mathbf{I}_N\otimes\left([\hat{\mathbf{D}}^{(2,3)}]_k^k+[\hat{\mathbf{D}}^{(3,2)}]_k^k\right)[\hat{\mathbf{T}}^{(1)}]_k+\frac{1}{2}(\hat{\mathbf{P}}^{(1)}-\mathbf{I}_N\otimes[\hat{\mathbf{D}}^{(1)}]_k^k)([\hat{\mathbf{T}}^{(2,3)}]_k+[\hat{\mathbf{T}}^{(3,2)}]_k)\\
&+\frac{1}{2}(\hat{\mathbf{P}}^{(2)}-\mathbf{I}_N\otimes[\hat{\mathbf{D}}^{(2)}]_k^k)([\hat{\mathbf{T}}^{(1,3)}]_k+[\hat{\mathbf{T}}^{(3,1)}]_k)+\frac{1}{2}(\hat{\mathbf{P}}^{(3)}-\mathbf{I}_N\otimes[\hat{\mathbf{D}}^{(3)}]_k^k)([\hat{\mathbf{T}}^{(1,2)}]_k+[\hat{\mathbf{T}}^{(2,1)}]_k)\\
&+\frac{1}{6}(\hat{\mathbf{J}}_0-\mathbf{I}_N\otimes[\hat{\mathbf{D}}_0]_k^k)\left([\hat{\mathbf{T}}^{(1,2,3)}]_k+[\hat{\mathbf{T}}^{(1,3,2)}]_k+[\hat{\mathbf{T}}^{(2,1,3)}]_k+[\hat{\mathbf{T}}^{(2,3,1)}]_k+[\hat{\mathbf{T}}^{(3,1,2)}]_k+[\hat{\mathbf{T}}^{(3,2,1)}]_k\right).
\end{aligned}\tag{H.2}$$

We can eliminate the last term in the expression above by multiplying by $[\hat{\mathbf{T}}_0^{-1}]^k$ from the left and using (5.21). Also because the above expression has six unknowns $\Big($ the $[\hat{\mathbf{D}}^{(\cdot,\cdot,\cdot)}]_k^k$'s

$\Big)$ for each $i_1, \sigma_1, i_2, \sigma_2, i_3, \sigma_3$ sextuple we have the freedom to set

$$[\hat{\mathbf{D}}^{(1,2,3)}]_k^k = [\hat{\mathbf{D}}_3(i_1,\sigma_1,i_2,\sigma_2,i_3,\sigma_3)]_k^k = \\ -3[\hat{\mathbf{T}}_0^{-1}]^k(\mathbf{I}_N \otimes [\hat{\mathbf{D}}^{(1,2)}]_k^k)\hat{\mathbf{T}}_0[\hat{\mathbf{U}}^{(3)}]_k + 3[\hat{\mathbf{T}}_0^{-1}]^k(\hat{\mathbf{P}}^{(1)} - \mathbf{I}_N \otimes [\hat{\mathbf{D}}^{(1)}]_k^k)\hat{\mathbf{T}}_0[\hat{\mathbf{U}}^{(2,3)}]_k, \tag{H.3}$$

while the equations for the other third-order terms can be obtained by permuting on the indices corresponding to $i_1, \sigma_1, i_2, \sigma_2, i_3, \sigma_3$ on the left and right hand side of (H.3). By algebraic manipulation one can show $[\hat{\mathbf{T}}_0^{-1}]^k(\mathbf{I}_N \otimes [\hat{\mathbf{D}}^{(1,2)}]_k^k)\hat{\mathbf{T}}_0[\hat{\mathbf{U}}^{(3)}]_k = [\hat{\mathbf{T}}_0^{-1}]^k(\mathbf{I}_N \otimes [\hat{\mathbf{D}}^{(1)}]_k^k)\hat{\mathbf{T}}_0[\hat{\mathbf{U}}^{(2,3)}]_k = 0$. This means we can simplify (H.3) to

$$[\hat{\mathbf{D}}^{(1,2,3)}]_k^k = 3[\hat{\mathbf{T}}_0^{-1}]^k\hat{\mathbf{P}}^{(1)}\hat{\mathbf{T}}_0[\hat{\mathbf{U}}^{(2,3)}]_k, \tag{H.4}$$

and by using (5.12) we can obtain (5.57).

APPENDIX I

Second-order approximation of the modal block-eigenvector

Solving (5.54) for the connected vehicle network , we obtain the (k,ℓ)-th block of $\hat{\mathbf{U}}^{(1,2)}$ whose elements are contained in

$$\mathbf{b}_{k\ell}^{(1,2)} = \begin{bmatrix} u_{k\ell,11}^{(1,2)} \\ u_{k\ell,21}^{(1,2)} \\ u_{k\ell,12}^{(1,2)} \\ u_{k\ell,22}^{(1,2)} \end{bmatrix}. \tag{I.1}$$

For $k \neq \ell$ using (5.75,5.76) we obtain

$$\begin{aligned} \mathbf{b}_{k\ell}^{(1,2)} &= \frac{1}{p(p-\alpha\beta_1)\eta_{k\ell}} \\ &\times \begin{bmatrix} (p+\beta_1(\beta_1\eta_{\ell 1}-\alpha))R(i_1,\sigma_1,i_2,\sigma_2)_{k\ell} + p\eta_{\ell 1}(p+\beta_1(\beta_1\eta_{k1}-\alpha))Q(i_1,\sigma_1,i_2,\sigma_2)_{k\ell} - p\beta_1\eta_{\ell 1}S(i_1,\sigma_1,i_2,\sigma_2)_{k\ell} \\ p\eta_{\ell 1}(-\beta_1 R(i_1,\sigma_1,\xi_2,\psi_2)_{k\ell} - p\beta_1\eta_{k1}Q(i_1,\sigma_1,\xi_2,\psi_2)_{k\ell} + pS(i_1,\sigma_1,\xi_2,\psi_2)_{k\ell}) \\ (-p\beta_1\eta_{k1}Q(i_1,\sigma_1,i_2,\sigma_2)_{k\ell} - \beta_1 R(i_1,\sigma_1,i_2,\sigma_2)_{k\ell} + pS(i_1,\sigma_1,i_2,\sigma_2)_{k\ell}) \\ p(R(i_1,\sigma_1,\xi_2,\psi_2)_{k\ell} + p\eta_{k1}Q(i_1,\sigma_1,\xi_2,\psi_2)_{k\ell} - \alpha\, S(i_1,\sigma_1,\xi_2,\psi_2)_{k\,\ell}) \end{bmatrix} \end{aligned} \tag{I.2}$$

where

$$\begin{aligned} Q(i_1,\sigma_1,i_2,\sigma_2)_{k\,\ell} &= \frac{2}{N}u_{k\ell,12}^{(1)}\Big(\mathrm{e}^{\mathrm{i}\frac{2\pi}{N}\sigma_2(\ell-1)} - 1\Big), \\ R(i_1,\sigma_1,i_2,\sigma_2)_{k\,\ell} &= \frac{2}{N}\Bigg(-\sum_{j=1}^{N}\mathrm{e}^{\mathrm{i}\frac{2\pi}{N}(i_1-1)(j-k)}\Big(\mathrm{e}^{\mathrm{i}\frac{2\pi}{N}\sigma_1(j-1)} - 1\Big)u_{j\ell,21}^{(2)}\Bigg), \\ S(i_1,\sigma_1,i_2,\sigma_2)_{k\,\ell} &= \frac{2}{N}\Bigg(u_{k\ell,22}^{(1)}\Big(\mathrm{e}^{\mathrm{i}\frac{2\pi}{N}\sigma_2(\ell-1)} - 1\Big) - \sum_{j=1}^{N}\mathrm{e}^{\mathrm{i}\frac{2\pi}{N}(i_1-1)(j-k)}\Big(\mathrm{e}^{\mathrm{i}\frac{2\pi}{N}\sigma_1(j-1)} - 1\Big)u_{j\ell,22}^{(2)}\Bigg). \end{aligned} \tag{I.3}$$

and $u^{(1)}_{k\ell,12}, u^{(2)}_{j\ell,21}, u^{(1)}_{k\ell,22}, u^{(2)}_{j\ell,22}$ are given in (5.72). For the case $k = \ell$ (5.54) has multiple possible solutions due to a non-zero nullity. In this case, we set

$$\mathbf{b}^{(1,2)}_{k\ell} = \begin{bmatrix} 0 \\ 0 \\ 0 \\ 0 \end{bmatrix}. \tag{I.4}$$

APPENDIX J

Cubic terms of the modal approximation

The coefficients in (5.77) and (5.78) are given by

$$L_0(i_1,\sigma_1,i_2,\sigma_2,i_3,\sigma_3) = \frac{1}{N^3}\frac{p\eta_{k1}}{(p-\alpha\beta_1)^2}\sum_{u=1,u\neq k}^{N}\frac{(\mathrm{e}^{\mathrm{i}\frac{2\pi}{N}\sigma_1(u-1)}-1)\mathrm{e}^{\mathrm{i}\frac{2\pi}{N}(i_1-1)(u-k)}}{\eta_{uk}}$$
$$\times\Bigg(-\frac{(\mathrm{e}^{\mathrm{i}\frac{2\pi}{N}\sigma_2(k-1)}-1)(\mathrm{e}^{\mathrm{i}\frac{2\pi}{N}\sigma_3(k-1)}-1)\mathrm{e}^{\mathrm{i}\frac{2\pi}{N}(i_2-1)(k-u)}}{\eta_{uk}}(\beta_1\eta_{u1}+\alpha)$$
$$+\sum_{j=1,j\neq k}^{N}\frac{(\mathrm{e}^{\mathrm{i}\frac{2\pi}{N}\sigma_2(j-1)}-1)(\mathrm{e}^{\mathrm{i}\frac{2\pi}{N}\sigma_3(k-1)}-1)\mathrm{e}^{\mathrm{i}\frac{2\pi}{N}(i_2-1)(j-u)}\mathrm{e}^{\mathrm{i}\frac{2\pi}{N}(i_3-1)(k-j)}}{\eta_{jk}}(\beta_1\eta_{k1}+\alpha)\Bigg),$$

and

$$L_1(i_1,\sigma_1,i_2,\sigma_2,i_3,\sigma_3) = \frac{1}{N^3}\frac{1}{(p-\alpha\beta_1)^2}\sum_{u=1,u\neq k}^{N}\frac{(\mathrm{e}^{\mathrm{i}\frac{2\pi}{N}\sigma_1(u-1)}-1)\mathrm{e}^{\mathrm{i}\frac{2\pi}{N}(i_1-1)(u-k)}}{\eta_{uk}}$$
$$\times\Bigg(\frac{(\mathrm{e}^{\mathrm{i}\frac{2\pi}{N}\sigma_2(k-1)}-1)(\mathrm{e}^{\mathrm{i}\frac{2\pi}{N}\sigma_3(k-1)}-1)\mathrm{e}^{\mathrm{i}\frac{2\pi}{N}(i_2-1)(k-u)}}{\eta_{uk}}(p\eta_{u1}+\alpha^2)$$
$$-\sum_{j=1,j\neq k}^{N}\frac{(\mathrm{e}^{\mathrm{i}\frac{2\pi}{N}\sigma_2(j-1)}-1)(\mathrm{e}^{\mathrm{i}\frac{2\pi}{N}\sigma_3(k-1)}-1)\mathrm{e}^{\mathrm{i}\frac{2\pi}{N}(i_2-1)(j-u)}\mathrm{e}^{\mathrm{i}\frac{2\pi}{N}(i_3-1)(k-j)}}{\eta_{jk}}(p\eta_{k1}+\alpha^2)\Bigg). \tag{J.1}$$

APPENDIX K

Coefficients for modal stability boundaries and modal frequencies

The coefficients for p_k and ω_k in (5.80) and (5.81) are obtained by plugging in (5.80) and (5.81) into (5.79) with $p = p_k$ and $\lambda = \mathrm{i}\omega_k$. The zeroth-order terms in (5.80) and (5.81) are then determined by setting all $\beta_{i\sigma} = 0$, taking the real and imaginary parts of (5.79), and solving the resulting two equations for p_{k0} and ω_{k0} we obtain

$$\begin{aligned} p_{k0} &= \tfrac{1}{2}(2\beta_1 + \alpha)\Big((2\beta_1 + \alpha)\tan^2\left(\tfrac{\theta_k}{2}\right) + \alpha\Big), \\ \omega_{k0} &= (2\beta_1 + \alpha)\tan\left(\tfrac{\theta_k}{2}\right), \end{aligned} \tag{K.1}$$

where $\theta_k = \frac{2\pi}{N}(k-1)$. These expressions indeed correspond to (5.67) and (5.68).

To obtain the first-order terms for indices i_1, σ_1, we take the partial derivative of (5.79) with respect to $\beta_{i_1\sigma_1}$ and evaluate the expression at $\beta_{i_1\sigma_1} = 0$. Then taking the real and imaginary parts, and performing some algebraic manipulation we get

$$\begin{aligned} p_{k1}(i_1,\sigma_1) = \frac{1}{2N}\Bigg(& \omega_{k0}\Bigg(\sin(\sigma_1\theta_k) + \frac{2\big(1+\sin(\frac{\theta_k}{2})\big)}{\sin(\theta_k)}\big(1-\cos(\sigma_1\theta_k)\big)\Bigg) \\ & + \alpha\Bigg(\frac{\sin(\sigma_1\theta_k)}{\tan(\frac{\theta_k}{2})} + \big(1-\cos(\sigma_1\theta_k)\big)\Bigg)\Bigg) \\ \omega_{k1}(i_1,\sigma_1) = \frac{1}{N}\Bigg(& \sin(\sigma_1\theta_k) + \tan(\tfrac{\theta_k}{2})\big(1-\cos(\sigma_1\theta_k)\big)\Bigg). \end{aligned} \tag{K.2}$$

Similarly, the second-order terms for the indices $i_1, \sigma_1, i_2, \sigma_2$ can be obtained by taking the second partial derivative of (5.79) with respect to $\beta_{i_1\sigma_1}$ and $\beta_{i_2\sigma_2}$ and evaluating the

results at $\beta_{i_1\sigma_1} = \beta_{i_2\sigma_2} = 0$. Splitting the real and imaginary parts we obtain

$$
\begin{aligned}
p_{k2}(i_1,\sigma_1,i_2,\sigma_2) &= \frac{2}{N}\omega_{k1}(i_1,\sigma_1)_k \frac{1-\cos(\sigma_2\theta_k)}{\sin(\theta_k)} \\
&\quad + \left(2\omega_{k0}\frac{1+\sin^2(\frac{\theta_k}{2})}{\sin(\theta_k)} + \alpha\right)\left(\mathrm{Re}\,K_1(i_1,\sigma_1,i_2,\sigma_2)|_{\mathrm{c}} + \frac{1}{\omega_{k0}}\mathrm{Im}\,K_0(i_1,\sigma_1,i_2,\sigma_2)|_{\mathrm{c}}\right) \\
&\quad + \left(\omega_{k0} + \alpha\frac{2\cos^2(\frac{\theta_k}{2})}{\sin(\theta_k)}\right)\left(-\mathrm{Im}K_1\,(i_1,\sigma_1,i_2,\sigma_2)|_{\mathrm{c}} + \frac{1}{\omega_{k0}}\mathrm{Re}\,K_0(i_1,\sigma_1,i_2,\sigma_2)|_{\mathrm{c}}\right) \\
\omega_{k2}(i_1,\sigma_1,i_2,\sigma_2) &= 2\left(\mathrm{Re}\,K_1(i_1,\sigma_1,i_2,\sigma_2)|_{\mathrm{c}}\tan(\tfrac{\theta_k}{2}) - \mathrm{Im}\,K_1(i_1,\sigma_1,i_2,\sigma_2)|_{\mathrm{c}}\right) \\
&\quad + \frac{2}{\omega_{k0}}\left(\mathrm{Re}\,K_1(i_1,\sigma_1,i_2,\sigma_2)|_{\mathrm{c}} + \mathrm{Im}\,K_0(i_1,\sigma_1,i_2,\sigma_2)|_{\mathrm{c}}\tan(\tfrac{\theta_k}{2})\right),
\end{aligned}
\tag{K.3}
$$

where "$|_{\mathrm{c}}$" indicates that the quantity is evaluated with all $\beta_{i\sigma} = 0$.

Finally, to obtain the third-order terms for the indices $i_1,\sigma_1,i_2,\sigma_2,i_3,\sigma_3$ we take the third partial derivative of (5.79) with respect to $\beta_{i_1\sigma_1}$, $\beta_{i_2\sigma_2}$, and $\beta_{i_3\sigma_3}$ and evaluate the result at

$\beta_{i_1\sigma_1} = \beta_{i_2\sigma_2} = \beta_{i_3\sigma_3} = 0$. Taking the real and imaginary parts yields

$$
\begin{aligned}
&p_{k3}(i_1,\sigma_1,i_2,\sigma_2,i_3,\sigma_3) = 3\omega_{k1}(i_1,\sigma_1)\omega_{k2}(i_1,\sigma_1,i_2,\sigma_2) + \frac{3}{N}\frac{1-\cos(\sigma_1\theta)}{\sin(\theta_k)}\omega_{k2}(i_2,\sigma_2,i_3,\sigma_3)\\
&+\left(\frac{3}{2}\omega_{k0} + \frac{\alpha}{2}\frac{1}{\tan(\frac{\theta_k}{2})}\right)\omega_{k3}(i_1,\sigma_1,i_2,\sigma_2,i_3,\sigma_3)\\
&+6\omega_{k1}(i_1,\sigma_1)\left(\mathrm{Re}\,K_1(i_2,\sigma_2,i_3,\sigma_3)|_{\mathrm{c}}\frac{1}{\tan(\theta_k)} + \mathrm{Im}\,K_1(i_2,\sigma_2,i_3,\sigma_3)|_{\mathrm{c}}\right)\\
&+6\omega_{k0}\left(\partial_{\varepsilon_1}\mathrm{Re}\,K_1(i_2,\sigma_2,i_3,\sigma_3)|_{\mathrm{c}}\frac{1}{\tan(\theta_k)} + \partial_{\varepsilon_1}\mathrm{Im}\,K_1(i_2,\sigma_2,i_3,\sigma_3)|_{\mathrm{c}}\right)\\
&+6\omega_{k0}\left(\mathrm{Re}\,L_1(i_1,\sigma_1,i_2,\sigma_2,i_3,\sigma_3)|_{\mathrm{c}}\frac{1}{\tan(\theta_k)} + \mathrm{Im}\,L_1(i_1,\sigma_1,i_2,\sigma_2,i_3,\sigma_3)|_{\mathrm{c}}\right)\\
&+6\left(\partial_{\varepsilon_1}\mathrm{Im}\,K_0(i_2,\sigma_2,i_3,\sigma_3)|_{\mathrm{c}}\frac{1}{\tan(\theta_k)} - \partial_{\varepsilon_1}\mathrm{Re}\,K_0(i_2,\sigma_2,i_3,\sigma_3)|_{\mathrm{c}}\right)\\
&+6\left(\mathrm{Im}\,L_0(i_1,\sigma_1,i_2,\sigma_2,i_3,\sigma_3)|_{\mathrm{c}}\frac{1}{\tan(\theta_k)} - \mathrm{Re}\,L_0(i_1,\sigma_1,i_2,\sigma_2,i_3,\sigma_3)|_{\mathrm{c}}\right),
\end{aligned}
$$

$$
\begin{aligned}
&\omega_{k3}(i_1,\sigma_1,i_2,\sigma_2,i_3,\sigma_3) = -3\frac{\omega_{k1}(i_1,\sigma_1)\omega_{k2}(i_2,\sigma_2,i_3,\sigma_3)}{\omega_{k0}}\\
&+6\frac{\omega_{k1}(i_1,\sigma_1)}{\omega_{k0}}\left(\mathrm{Re}\,K_1(i_2,\sigma_2,i_3,\sigma_3)|_{\mathrm{c}}\tan(\tfrac{\theta_k}{2}) - \mathrm{Im}\,K_1(i_2,\sigma_2,i_3,\sigma_3)|_{\mathrm{c}}\right)\\
&+6\left(\partial_{\varepsilon_1}\mathrm{Re}\,K_1(i_2,\sigma_2,i_3,\sigma_3)|_{\mathrm{c}}\tan(\tfrac{\theta_k}{2}) - \partial_{\varepsilon_1}\mathrm{Im}\,K_1(i_2,\sigma_2,i_3,\sigma_3)|_{\mathrm{c}}\right)\\
&+6\left(\mathrm{Re}\,L_1(i_1,\sigma_1,i_2,\sigma_2,i_3,\sigma_3)|_{\mathrm{c}}\tan(\tfrac{\theta_k}{2}) - \mathrm{Im}\,L_1(i_1,\sigma_1,i_2,\sigma_2,i_3,\sigma_3)|_{\mathrm{c}}\right)\\
&+\frac{6}{\omega_{k0}}\left(\partial_{\varepsilon_1}\mathrm{Re}\,K_0(i_2,\sigma_2,i_3,\sigma_3)|_{\mathrm{c}} + \partial_{\varepsilon_1}\mathrm{Im}\,K_0(i_2,\sigma_2,i_3,\sigma_3)|_{\mathrm{c}}\tan(\tfrac{\theta_k}{2})\right)\\
&+\frac{6}{\omega_{k0}}\left(\mathrm{Re}\,L_0(i_1,\sigma_1,i_2,\sigma_2,i_3,\sigma_3)|_{\mathrm{c}} + \mathrm{Im}\,L_0(i_1,\sigma_1,i_2,\sigma_2,i_3,\sigma_3)|_{\mathrm{c}}\tan(\tfrac{\theta_k}{2})\right).
\end{aligned}
\tag{K.4}
$$

BIBLIOGRAPHY

[1] V2X functional and performance test report; test procedures and results. 5GAA P-190033, 5G Automotive Association, (2018)

[2] Timeline for deployment of C-V2X - Update 5G Automotive Association, (2019)

[3] Aeberhard, M., Rauch, S., Bahram, M., Tanzmeister, G., Thomas, J., Pilat, Y., Homm, F., Huber, W., Kaempchen, N.: Experience, results and lessons learned from automotive driving on Germany's highways IEEE Intelligent Transportation Systems Magazine, **7**(1), 42–57, (2015).

[4] Alam, A., Mårtensson, J., Johansson, K.H.: Experimental evaluation of decentralized cooperative cruise control for heavy-duty vehicle platooning. Control Engineering Practice **38**, 11–25 (2015)

[5] Alam, A., Besselink, B., Turri, V., Martensson, J., Johansson, K.H.: Heavy-duty vehicle platooning for sustainable freight transportation: a cooperative method to enhance safety and efficiency. IEEE Control Systems **35**(6), 34–56 (2015)

[6] Arena, F., Pau, G.: An overview of vehicular communications Furure internet **11**(27), fil11020027, (2019)

[7] ARIB STD-T88: Dedicated short range communication system, Association of Radio Industries and Buisinesses (ARIB), ARIB standard, (2012).

[8] Avedisov, S.S., Orosz, G.: Nonlinear network modes in cyclic systems with applications to connected vehicles. Journal of Nonlinear Science **25**(4), 1015–1049 (2015)

[9] Avedisov, S. S., Orosz, G.: Analysis of connected vehicle systems using network-based perturbation techniques. Nonlinear Dynamics **89**(3), 1651–1672 (2017)

[10] Avedisov, S. S., Bansal, G.: Vehicle mitigation system. Patent US 15 403 064, July, 2018

[11] Avedisov, S. S., Bansal, G., Orosz, G.: Experimental verification platform for connected vehicle networks. Proceedings of the 21st IEEE International Conference on Intelligent Transportation Systems, IEEE, 818–823, (2018)

[12] Bando, M., Hasebe, K., Nakanishi, K., Nakayama, A.: Analysis of optimal velocity model with explicit delay. Physical Review E. **58**(5), 5429–5435 (1998)

[13] Belvy, D., Cao X., Gordon, M., Ozbilgin, G., Kari, D., Nelson, B., Woodruff, J., Barth, B., Murray, C., Kurt, A., Redmill, K., Ozguner, U.: Lane change and merge maneuvers for connected automated vehicles: a survey IEEE Transactions on Intelligent Transportation Systems, **1**(1), 105–120 (2016)

[14] Caveney, D.: Cooperative vehiclular safety applications IEEE Control Systems Magazine, **30**(4), 38–53, (2010)

[15] Chou, F., Shladover, S. E., Bansal, G.: Coordinates merge control based on v2v communication Proceedings of the 2016 IEEE Vehicular Networking Conference, IEEE, 2016, pp. 1Ű8.

[16] Cochelin, B., Damil, N., Potier-Ferry, M.: Asymptotic-numerical methods and Pade approximations for non-linear elastic structures. International Journal on Numerical Methods in Engineering **37**(7), 1187–1213 (1994)

[17] di Bernardo, M., Salvi, A., Santini, S.: Distributed consensus strategy for platooning of vehicles in the presence of time-varying heterogeneous communication delays. IEEE Transactions on Intelligent Transportation Systems **16**(1), 102–112 (2015)

[18] Dollar, R. A., and Vahidi, A.: Efficient and collision-free anticipative cruise control in randomly mixed strings IEEE Transactions on Intelligent Transportation Systems **3**(4), 439–452 (2018)

[19] Vehicle Safety Communications- Applications VSC-A. Final report. U.S. Department of Transportation, National Highway Traffic Safety Administration, DOT HS 811 492 A, Available online, (2011)

[20] Bayless, S., Guan, A., Paruch, J., Carter, J., Schaffnit, T., Shaw, A., America, ITS.: The impact of a vehicle-to-vehicle communications rulemaking on growth in the DSRC automotive aftermarket: a market adoption model and forecast for dedicated short range communications (DSRC) for light and heavy vehicle categories. U.S. Department of Transportation, Intelligent Transportation Systems, FHWA-JPO-17-487, Available online, (2016)

[21] EN 12253: Road transport and traffic telematics - dedicated short range communication (DSRC) - physical layer using microwave at 5.8 GHz, European Committee for Standardization, (2004)

[22] Gasser, I., Sirito, G., Werner, B.: Bifurcation analysis of a class of 'car following' traffic models. Physica D **197**(3-4), 222–241 (2004)

[23] Gallagher, B., Akatsuka, H., Suzuki, H.: Wireless communications for vehicle safety: radio link performance and wireless connectivity methods. IEEE Vehicular Technology Magazine **1**(4), 4–24 (2006)

[24] Ge, J.I., Avedisov, S.S., Orosz, G.: Stability of connected vehicle platoons with delayed acceleration feedback. In: Proceedings of the ASME Dynamical Systems and Control Conference. ASME (2013). Paper no. DSCC2013-4040

[25] Ge, J.I., Orosz, G.: Dynamics of connected vehicle systems with delayed acceleration feedback. Transportation Research, Part C **46**, 46–64 (2014)

[26] Ge, J.I., Orosz, G., Hajdu, D., Insperger, T., Moehlis, J.: To delay or not to delay – stability of connected cruise control time delay systems. Theory, Numerics, Applications, and Experiments. In: T. Insperger, T. Ersal, G. Orosz (eds.) Advances in Delays and Dynamics, vol. 7. Springer (2017)

[27] Ge, J.I., Orosz, G.: Optimal control of connected vehicle systems with communication delay and driver reaction time. IEEE Transactions on Intelligent Transportation Systems **18**(8), 2056–2070 (2017)

[28] Ge, J. I., Avedisov, S. S., He, C. R., Qin, W. B., Sadeghpour, and Orosz, G.: Experimental validation of connected automated vehicle design among human-driven vehicles. Transportation Research Part C **91**, 335–352 (2018)

[29] Geiger, A., Lauer, M., Moosmann, F., Ranft, B., Rapp, H., Stiller, C., Ziegler, J.: Team Annieway's entry to the 2011 grand cooperative driving challenge. IEEE Transactions on Intelligent Transportation Systems **13**(3), 1008–1017 (2012)

[30] Gendelman, O.V.: Bifurcations of nonlinear normal modes of linear oscillator with strongly nonlinear damped attachment. Nonlinear Dynamics **37**(2), 115–128 (2004)

[31] Georgiades, F., Peeters, M., Kerschen, G., Golinval, J.C., Ruzzene, M.: Modal analysis of a nonlinear periodic structure with cyclic symmetry. AIAA Journal **47**(4), 1014–1025 (2009)

[32] Grolet, A., Thouverez, F.: Vibration analysis of a nonlinear system with cyclic symmetry. Journal of Engineering, Gas Turbines, and Power **133**(2), 022502 (2011)

[33] Happawana, G.S., Nwokah, O.D.I., Bajaj, A.K., Azene, M.: Free and forced response of mistuned linear cyclic systems: a singular perturbation approach. Journal of Sound and Vibration **211**(5), 761–789 (1998)

[34] Harding, J., Powell, G. R., Yoon, R., Fikentsher, J., Doyle, C., Sade, D., Lucuc, M., Simons, J., Wang, J.: Vehicle-to-vehicle communications: Readiness of V2V technology for application National Highway Traffic Safety Administration, Technical Report, DOT HS 812014, (2014)

[35] Haterbouch, M., Benamar, R.: Geometrically nonlinear free vibrations of simply supported isotropic thin circular plates. Journal of Sound and Vibration **280**(3-5), 903–924 (2005)

[36] Traffic and related self-driven many-particle systems Review of Modern Physics **73**(4), 1067–1141 (2001)

[37] Helbing, D., Moussaid, M.: Analytical calculation of critical pertubation amplitudes and critical densities by non-linear stability analysis of a simple traffic flow model. European Physics Journal B **69**(4), 571-581 (2009)

[38] Jézéquel, L., Lamarque, C.H.: Analysis of non-linear dynamic systems by the normal form theory. Journal of Sound and Vibration **149**(3), 429-459 (1991)

[39] Kenney, J. B.: Dedicated short-range communications (DSRC) standards in the United States. Proceedings of the IEEE, **99**(7), 1162–1182, (2011)

[40] Kenney, J. B.: An Automaker Perspective on Next Gen V2X. IEEE 802.11-18/0917r0, Toyota InfoTechnology Center, (2018)

[41] Kerschen, G., Peeters, M., Golinval, J.C., Vakakis, A.F.: Nonlinear normal modes, Part I: A useful framework for the structural dynamicist. Mechanical Systems and Signal Processing **23**(1), 170–194 (2009)

[42] Kim, C., Park, J., Huh, K.: Target classification layer design via vehicle-to-vehicle communcation. Journal of Automobile Engineering, **230**(13), pp. 1849–1861 (2016)

[43] Kiss, A. K., Avedisov, S. S., Bachrathy, D., Orosz, G.: On the global dynamics of connected vehicle systems. Nonlinear Dynamics, **96**(3), 1865–1877 (2019)

[44] Kreideh, A. R., Wu, C., Bayen, A. M.: Dissipating stop-and-go waves in closed and open networks via deep reinforcement learning Proceedings of the 21st IEEE International Conference on Intelligent Transportation Systems, 1475–1480, (2018)

[45] Kiss, A. K., Avedisov, S. S., Bachrathy, D., Orosz, G.: On the global dynamics of connected vehicle systems. Nonlinear Dynamics, **96**(3), pp. 1865–1877 (2019)

[46] Kuznetsov, Y.: Elements of Applied Bifurcation Theory. Springer, Berlin (2004)

[47] Liu, Z.H., Liu, W., Gao, W.C., Cheng, X.: Advances of research on mode localization in mistuned cyclically periodic structures. Applied Mechanics and Materials, **405-408**, pp. 3198–3203 (2013)

[48] Lu, X.Y., Hedrick, J.K., Drew, M.: ACC/CACC-control design, stability and robust performance. In: Proceedings of the American Control Conference, vol. 6, pp. 4327–4332. IEEE (2002)

[49] Manevich, L.I., Mikhlin, Y.V.: On periodic solutions close to rectilinear normal vibration modes. Journal of Applied Mathamatics and Mechanics (PMM) **36**(6), 1051–1058 (1972)

[50] Mangel, T., Michl, M., Klemp, O., Hartenstein, H.: Real-world measurements of non-line-of-sight reception quality for 5.9 GHz IEEE 802.11p at intersections. In: T. Strang, A. Festag, A. Vinel, R. Mehmood,C. Rico Garcia, M. Röckl (eds.) Communication Technologies for Vehicles, pp. 189–202. Springer (2011)

[51] Masini, B. M., Bazzi, A., Zanella, A.: A survey on the roadmap to mandate on board connectivity and enable V2V-based vehicular sensor networks. Sensors, **18**(7), pp. 2207, Multidisciplinary Digital Publishing Institute, (2018)

[52] Medina, A. I. M., van de Wouw, N., Nijmeijer, H.: Cooperative intersection control based on virtual platooning IEEE Transactions on Intelligent Transportation Systems **19**(6), 1459–1471 (2018)

[53] Wang, M., Daamen, W., Hoogendoorn, S.P., van Arem, B.,: Cooperative car-following control: distributed algorithm and impact on moving jam features IEEE Transactions on Intelligent Transportation Systems **17**(5), 1459–1471 (2016)

[54] Milanés, V., Shladover, S.E.: Modeling cooperative and autonomous adaptive cruise control dynamic responses using experimental data. Transportation Research Part C: Emerging Technologies **48**, 285–300 (2014)

[55] Milanés, V., Shladover, S.E., Spring, J., Nowakowski, C., Kawazoe, H., Nakamura, M.: Cooperative adaptive cruise control in real traffic situations. IEEE Transactions on Intelligent Transportation Systems **15**(1), 296–305 (2014)

[56] Milanés, V., Shladover, S. E., Handling cut-in vehicles in strings of cooperative adaptive cruise control vehicles Journal of Intelligent Transportation Systems **20**(2), 178–191 (2016)

[57] Nayfeh, A.H.: On direct methods for constructing nonlinear normal modes of continuous systems. Journal of Vibration and Control **1**(4), 389–430 (1995)

[58] Nayfeh, A.H., Nayfeh, S.A.: On nonlinear modes of continuous systems. Journal of Vibrations and Acoustics **116**(1), 129–136 (1994)

[59] Olson, B.J., Shaw, S.W., Shi, C., Pierre, C., Parker, R.G.: Circulant matrices and their application to vibration analysis. Applied Mechanics Review **66**(4), 040803 (2014)

[60] Öncü, S., Ploeg, J., van de Wouw, N., Nijmeijer, H.: Cooperative adaptive cruise control: Network-aware analysis of string stability. IEEE Transactions on Intelligent Transportation Systems **15**(4), 1527–1537 (2014)

[61] Orosz, G., Stépán, G.: Subcritical Hopf bifurcations in a car-following model with reaction-time delay. Proceedings of the Royal Society **462**(2073), 2643–2670 (2006)

[62] Orosz, G.: Connected cruise control: modelling, delay effects, and nonlinear behaviour. Vehicle System Dynamics **54**(8), 1147–1176 (2016)

[63] Orosz, G.: Connected cruise control: modeling, delays, and nonlinear behavior. Vehicle System Dynamics, (submitted) (2014).

[64] Orosz, G., Moehlis, J., Bullo, F.: Delayed car-following dynamics for human and robotic drivers. Proceedings of the ASME IDETC/CIE Conference, pp. 529–538. ASME (2011). Paper no. DETC2011-48829

[65] Orosz, G., Stépán, G.: Subcritical Hopf bifurcations in a car-following model with reaction-time delay. Proceedings of the Royal Society **462**(2073), 2643–2670 (2006)

[66] Orosz, G., Wilson, R.E., Stépán, G.: Traffic jams: dynamics and control. Philosophical Transactions of The Royal Society A **368**(1928), 4455–4479 (2010)

[67] Orosz, G., Wilson, R.E., Szalai, R., Stépán, G.: Exciting traffic jams: Nonlinear phenomena behind traffic jam formation on highways. Physical Review E **80**(4),046205 (2009)

[68] Orosz, G., Ge J. I., He, C. R., Avedisov S. S., Qin W. B., Zhang, L.: Seeing beyond the line of sight Ű- controlling connected automated vehicles. ASME Dynamic Systems and Control Magazine, **5**(4), 8–12, (2017)

[69] Peeters, M., Viguié, R., Sérandour, G., Kerschen, G., Golinval, J.C.: Nonlinear normal modes, Part II: Toward a practical computation using numerical continuation techniques. Mechanical Systems and Signal Processing **23**(1), 195–216 (2009)

[70] Pierre, C., Dowell, E.H.: Localization of vibrations by structural irregularity. Journal of Sound and Vibration **114**(3), 549–564 (1987)

[71] Ploeg, J., van de Wouw, N., Nikmeijer, H.:Fault tolerance of cooperative vehicle platoons subject to communication delay Proceedings of the 12th IFAC Workshop on Time-Delay Systems, pp. 352–357. IFAC (2015)

[72] Ploeg, J., van de Wouw, N., Nijmeijer, H.: Lp string stability of cascaded systems: application to vehicle platooning. IEEE Transactions on Control Systems Technology **22**(2), 1527–1537 (2014)

[73] Qin, W.B., Orosz, G.: Digital effects and delays in connected vehicles: linear stability and simulations. Proceedings of the ASME Dynamical Systems and Control Conference, ASME (2013), Paper no. DSCC2013-3830

[74] Qin, W.B., Gomez, M.M., Orosz, G.: Stability analysis of connected cruise control with stochastic delays. Proceedings of the American Control Conference, pp. 4624–4629. IEEE (2014)

[75] Qin, W.B., Gomez, M.M., Orosz, G.: Stability and frequency response under stochastic communication delays with applications to connected cruise design. IEEE Transactions on Intelligent Transportation Systems **18**, 388–403 (2017)

[76] Qin, W. B., Orosz, G.: Experimental validation of string stability for connected vehicles subject to information delay IEEE Transactions on Control Systems Technology, published online, (2019)

[77] Rajamani, R.: Vehicle dynamics and control. Springer (2011)

[78] Roose, D., Szalai, R.: Continuation and bifurcation analysis of delay differential equations. In: B. Krauskopf, H. M. Osinga, J. Galan-Vioque (eds.) Numerical Continuation Methods for Dynamical Systems, Understanding Complex Systems. pp. 359-399. Springer (2007)

[79] Rosenberg, R.M.: On nonlinear vibrations of systems with many degrees of freedom. Advances in Applied Mechanics **9**, 155–242 (1966)

[80] SAE: Dedicated Short Range Communications (DSRC) Message Set Dictionary Set. SAE J2735SET_201603, SAE International, (2016)

[81] SAE: Taxonomy and definitions for terms related to driving automation systems for on-road motor vehicles. SAE International, (2016)

[82] Bezzina, D., Sayer, J.: Safety pilot model deployment: Test conductor team report. Report No. DOT HS 812 171, Washington, DC: National Highway Traffic Safety Administration, (2015)

[83] Sepulcre, M., Gozalvez, J., Coll-Perales, B., Lucas-Estañ, M. C., Gisbert, J. R.: Empirical Performance Models for V2V Communications 2015 IEEE International Conference on Computer and Information Technology; Ubiquitous Computing and Communications; Dependable, Autonomic and Secure Computing; Pervasive Intelligence and Computing, 737–742 (2015).

[84] Shaw, S.W., Pierre, C.: Normal modes for non-linear vibratory systems. Journal of Sound and Vibration **164**(1), 85–124 (1993)

[85] Shladover, S.E.: Longitudinal control of automotive vehicles in close-formation platoons. Journal of Dynamic Systems, Measurement, and Control **113**(2), 231–241 (1991)

[86] Shladover, S.E.: PATH at 20-history and major milestones IEEE Transactions on Intelligent Transportation Systems, **8**(4), 584–592 (2007)

[87] Shladover, S.E., Nowakowski, C., Lu, X.Y., Ferlis, R.: Cooperative adaptive cruise control (CACC) definitions and operating concepts. In: Proceedings of the 94th Annual TRB Meeting, 15-3265 (2015)

[88] Shladover, S.E., Su, D., Lu, X.Y.: Impacts of cooperative adaptive cruise control on freeway traffic flow. Transportation Research Record: Journal of the Transportation Research Board (2324), 63–70 (2012)

[89] Slater, J.C.: A numerical method for determining nonlinear normal modes. Nonlinear Dynamics **10**(1), 19–30 (1996)

[90] Use of Hardware in the Loop (HIL) Simulation for Developing Connected Autonomous Vehicle (CAV) Applications. Technical Paper2019-01-1063, SAE International, (2019)

[91] Stern, R. E., Cui, S., Monache, M. L. D., Bhadani, R., Bunting, M., Churchill, M., Hamilton, N., Haulcy, R., Pohlmann, H., Wu, F., Piccoli, B., Seibold, B., Sprinkle, J., Work, D. B.: Dissipation of stop-and-go waves via control of autonomous vehicles: Field experiments Transportation Research Part C, **10**, 205–221 (208)

[92] Sun, X., Yin, Y.: Behaviorally stable vehicle platooning for ener- gy savings New Journal of Physics **10**, 33001 (2008)

[93] Sugiyama, Y., Fukui, M., Kikuchi, M., Hasebe, K., Nakayama, A., Nishinari K., Tadaki, S., Yukawa, S.: Traffic jams without bottlenecks - experimental evidence for the physical mechanism of the formation of a jam Transportation Research Part C: Emerging Technologies **99**, 37–52 (2019)

[94] Swaroop, D., Hedrick, J. K., String stability of interconnected systems. IEEE Transactions on Automatic Control **41**(3), 349–357 (1996)

[95] Szalai, R., Orosz, G.: Decomposing the dynamics of heterogeneous delayed networks with applications to connected vehicle systems. Physical Review E **88**(4), 040902 (2013)

[96] Szemplinska-Stupnicka, W.: "Non-linear normal modes" and the generalized Ritz method in the problems of vibrations of non-linear elastic continuous systems. International Journal of Non-linear Mechanics **18**(2), 149–165 (1983)

[97] Talebpour, A., Mahmassani, H. S.: Influence of connected and autonomous vehicles on traffic flow stability and throughput. Transportation Research Part C: emerging technologies, **71**, 143–163 (2016)

[98] Steadman, M., Huntsman, B.: Connected Vehicle Infrastructure: Deployment and Funding Overview. PRC 17-77 F, Texas A&M Transportation Institute, (2018)

[99] Tsugawa, S., Jeschle, S., Shladover S. E.: A review of truck platooning projects for energy savings IEEE Transactions on Intelligent Transportation Systems,**1**(1), 68–77, (2016)

[100] van de Hoef, S., Johansson, K. H., Dimarogonas D. V.: Fuel-efficient en route formation of truck platoons IEEE Transactions on Intelligent Transportation Systems **19**(1), 102–112, IEEE (2018)

[101] Vinitsky, E., Parvate, K., Kreideh, A. R., Wu, C., Bayen, A. M.: Lagrangian control through deep-rl: applications to bottleneck decongestion Proceedings of the 21st IEEE International Conference on Intelligent Transportation Systems, 759–765, (2018)

[102] Wang, F., Bajaj, A.K.: Nonlinear normal modes in multi-mode models of an inertially coupled elastic structure. Nonlinear Dynamics **47**(1-3), 25–47 (2007)

[103] Wang, M., Daamen, W., Hoogendoorn, S. P., van Arem, B.: Cooperative car-following control: distributed algorithm and impact on moving jam features. IEEE Transactions on Intelligent Transportation Systems **17**(5), 1459–1471, IEEE (2016)

[104] Wang, M., Daamen, W., Hoogendoorn, S. P., van Arem, B.: Rolling horison control framework for driver assistance systems. part ii: Cooperative sensing and cooperative control. Transportation Research Part C: Emerging Technologies **40**, 290–311, (2016)

[105] Wei, S.T., Pierre, C.: Localization phenomena in mistuned assemblies with cyclic symmetry part i: free vibrations. Journal of Vibration, Acoustics, Stress, and Reliability in Design **110**(4), 429–438 (1988)

[106] Wu, C., Parvate, K., Kheterpal, N., Dickstein, L., Mehta, A., Vinitsky, E., Bayen, A. M.: Framework for control and deep reinforcement learning in traffic Proceedings of the 20th IEEE International Conference on Intelligent Transportation Systems, (2017)

[107] Xiao, L., Wang, M., Schakel, W., van Arem, B.: Unravelling effects of cooperative adaptive cruise control deactivation on traffic flow characteristics at merging bottlenecks Transportation research part C: emerging technologies, **96**, 380–397 (2018)

[108] Zhang, L., Orosz, G.: Designing network motifs in connected vehicle systems: Delay effects and stability. Proceedings of the ASME Dynamic Systems and Control Conference, pp. V003T42A006. ASME (2013). Paper no. DSCC2013-4081

[109] Zhang, L., Orosz, G.: Motif-based design for connected vehicle systems in presence of heterogeneous connectivity structures and time delays. IEEE Transactions on Intelligent Transportation Systems **17**(6), 1638–1651 (2016)

[110] Liao, Y., Li, S.E., Wang, W., Wang, Y., Li, G., Cheng, B.,: Detection of driver cognitive distraction: a comparison study of stop-controlled intersection and speed-limited highway. IEEE Transactions on Intelligent Transportation Systems **17**(6), 1628–1637 (2016)

[111] Zheng, Y., Li, S. E., Li, K., Wang, L. Y.: Stability margin improvement of vehicular platoon considering undirected topology and asymmetric control. IEEE Transactions on Control Systems Technology **24**(4), 1253–1265 (2016)

[112] Zheng, Y., Li, S. E., Li, K., Borelli, F., Hedrick, J. K.: Distributed model predictive control for heterogeneous vehicle platoons under unidirectional topologies IEEE Transactions on Intelligent Transportation Systems **25**(3), 899–910 (2017)